ISSN 1343-2230

CNS-REP-98
March, 2020

Annual Report 2018

Center for Nuclear Study,
Graduate School of Science, the University of Tokyo

Editor
Hiroki Nagahama

Center for Nuclear Study

CNS Reports are available from:
Wako-Branch at RIKEN
Center for Nuclear Study,
Graduate School of Science, the University of Tokyo
2-1 Hirosawa, Wako
351-0198, Japan
Tel: +81-48-464-4191
Fax: +81-48-464-4554

Annual Report 2018

Center for Nuclear Study,
Graduate School of Science, the University of Tokyo

Preface

This is the annual report of the Center for Nuclear Study (CNS), Graduate School of Science, the University of Tokyo, for the fiscal year 2018 (April 2018 through March 2019). During this period, a lot of research activities in various fields of nuclear physics have been carried out and a wide variety of fruitful results have been obtained at CNS. This report summarizes such research activities. I hereby mention some highlights of the report.

The Center for Nuclear Study (CNS) aims to elucidate the nature of nuclear system by producing the characteristic states where the Isospin, Spin and Quark degrees of freedom play central roles. These researches in CNS lead to the understanding of the matter based on common natures of many-body systems in various phases. We also aim at elucidating the explosion phenomena and the evolution of the universe by the direct measurements simulating nuclear reactions in the universe. In order to advance the nuclear science with heavy-ion reactions, we develop AVF upgrade, CRIB and OEDO-SHARAQ facilities in the large-scale accelerator laboratories RIBF. The OEDO started in operation to provide a good quality of low-energy RI beam for physics experiments. We added a new group for fundamental symmetry by using heavy RIs. We promote collaboration programs at RIBF as well as RHIC-PHENIX and ALICE-LHC with scientists in the world, and host international meetings and conferences. We also provide educational opportunities to young scientists in the heavy-ion science through the graduate course as a member of the department of physics in the University of Tokyo and through hosting the international summer school.

The NUSPEQ (NUclear SPectroscopy for Extreme Quantum system) group studies exotic structures in high-isospin and/or high-spin states in nuclei. The CNS GRAPE (Gamma-Ray detector Array with Position and Energy sensitivity) is a major apparatus for high-resolution in-beam gamma-ray spectroscopy. Missing mass spectroscopy using the SHARAQ is used for another approach on exotic nuclei. The group plays a major role in the OEDO/SHARAQ project described below. In 2018, the following progress has been made. Experimental data taken under the EURICA collaboration for studying octupole deformation in neutron-rich Ba isotopes was published. Analysis of new measurements of the ^{4}He(^{8}He, ^{8}Be)4n reaction for better statistics and better accuracy has been proceeding.

The main mission of the nuclear astrophysics group is to study astrophysical reactions and special nuclear structures using low-energy RI beams. In 2018, a new direct measurement of ^{8}Li(α,n)^{11}B reaction using a ^{8}Li beam at CRIB was carried out to solve the discrepancy of previous inclusive and exclusive measurements. We simultaneously employed γ-ray detection with a $LaBr_3$ system and neutron detection with scintillators for the first time. A ^{7}Be-implanted gold target was produced at CRIB, for a direct measurement of the ^{7}Be(d, p) reaction, which is also a possible destruction reaction of ^{7}Be in the Big-bang nucleosynthesis. The implanted target was transferred to JAEA, where a measurement of the ^{7}Be(d, p) reaction was made. We also performed an elastic scattering measurement of the ^{25}Al+p system, in order to evaluate the reaction rate of ^{22}Mg(α, p) which models indicate may strongly influence the light curve of X-ray bursts.

Main goal of the quark physics group is to understand the properties of hot and dense nuclear matter created by colliding heavy nuclei at relativistic energies. The group has been involved in the PHENIX experiment at Relativistic Heavy Ion Collider (RHIC) at Brookhaven National Laboratory, and the ALICE experiment at Large Hadron Collider (LHC) at CERN. As for ALICE, the group has involved in the data analyses, which include the measurement of low-mass lepton pairs in Pb-Pb collisions and studies of J/ψ production, long range two particle correlations, and low pT photon productions in small systems such as pp and p-Pb collisions. The group has been responsible to run the experiment in 2018 and for the future TPC upgrade using a Gas Electron Multiplier (GEM). Development of the online data processing by utilizing FPGA and GPU, has been ongoing in 2018.

The Exotic Nuclear Reaction group studies various exotic reactions induced by beams of unstable nuclei. One subject is inverse-kinematics (p,n) reaction. In 2018 a set of neutron counters PANDORA was introduced for the first time in RIBF experiment for the study of the ^{11}Li(p,n) and ^{14}Be(p,n) reactions. A candidate nucleus for further (p,n) study is the high spin isomer of ^{52}Fe(12+). Development of the isomer beam was continued at HIMAC.

The OEDO/SHARAQ group pursues experimental studies of RI beams by using the OEDO beamline and the SHARAQ spectrometer. A mass measurement by TOF-$B\rho$ technique for very neutron-rich successfully reaches calcium isotopes beyond N=34, $^{55-57}$Ca, and a physics paper is published. The experimental study of 0^- strength in nuclei using the parity-transfer charge exchange (^{16}O, ^{16}F) is on progress and the data analysis is on the final stage. Three experiments were carried out in 2017 using the OEDO beamline, which can decelerate and focus RI beams. We made progress of analysis on the data this year. Preliminary results were already given in some conferences. Optical studies for OEDO-SHARAQ system is ongoing to improve the transmission and to advance high-resolution studies of RI beams.

Two types of gaseous active target TPCs called CAT's and GEM-MSTPC are developed and used for the missing mass spectroscopy. The CAT's are employed for the study of equation of state of nuclear matter. The measurement of giant monopole resonance in ^{132}Sn at RIBF with CAT-S and the data analysis is ongoing. A larger active target called CAT-M, which has 10-times larger active volume than that of CAT-S, has been developed from 2016. The CAT-M was commissioned at HIMAC and the excitation energy spectrum of ^{136}Xe for proton scattering was measured in FY2017. A measurement of deuteron inelastic scattering on ^{132}Xe was performed in FY2018. The GEM-MSTPC is employed for the nuclear astrophysics study. The data analysis of (α,p) reaction on ^{18}Ne and ^{22}Mg and the β decay of ^{16}Ne followed by γ emission are ongoing.

A recoil particle detector for missing mass spectroscopy, named TiNA, had been updating under the collaboration with RIKEN and RCNP. TiNA originally consisted of 6 sector telescopes. Each of which had a single-sided stripped-type SSD and 2 CsI(Tl) crystals. TiNA was employed for measuring (d,p) reaction at OEDO. For the approved experiment of ^{50}Ca(d,p), 4 double-sided stripped detectors will be added as a barrel detector. Development of tritium targets is still on-going. Several deuterium doped Ti targets were fabricated at the Toyama Univ. The amount the deuterium was measured to be around D/T$\sim$0.7 from the elastic recoil detection analysis at Tsukuba University. Further improvement of the deuterium ratio have been tried. The production cross section ^{178m2}Hf was evaluated for the mass production in the future. The digital signal processing devices for the GRAPE have been developed to measure the cascade transitions from the isomeric state. After chemical separation of Hf at the hot laboratory at RIBF. The weak cascade decay was successfully measured.

AVF upgrade project that includes the development of ion sources, RIKEN AVF cyclotron and beam transport system is in progress. In 2018, the operating time of the HyperECR was 2158 hours, which is 43 % of the total operating time of AVF. The beam extraction system of the HyperECR is under development to realize a high intensity and low emittance beam. To increase stabler ^{6}Li^{3+} ion beam, a crucible position was optimized by measuring a plasma light intensity and its temperature. For the beam transport system, the measurement accuracy of pepper-pot emittance monitor was improved to calculate more accurate injection beam trajectory. Moreover, the ion optics studies of the beam line to the experiment device of EDM search were started by supposing beam line which have additional beam focusing magnets.

The permanent electric dipole moment (EDM) of an atomic system such as Fr is a combination of those of each constituent particle and also CP-violating interactions, which is important observable to understand the antimatter disappearance mechanism. The development of the new surface ionizer was in progress and will be installed at E7 in RIKEN. In the EDM experiment, we measure two atomic resonance frequencies that are in the electric field parallel to the magnetic field, and anti-parallel to the magnetic field in the OL. The frequency differences due to the magnetic field shift and electric field change have to be minimized to reduce the systematic errors. The unique solution to eliminate these errors are to monitor the spin frequencies of two atomic species, which have no EDM contribution compared with Fr, and measure the magnetic field and vector light shift explicitly. Based on this idea, the dual species co-magnetometer was successfully developed.

The nuclear theory group participates in a project, ”Priority Issue 9 to be tackled by using the Post-K Computer” and promotes computational nuclear physics utilizing supercomputers. In FY2018, we performed the large-scale shell-model calculations and Monte Carlo shell-model calculations to study various neutron-rich nuclei under collaborations with experimental groups. In particular, we revealed the occurrence of the shape coexistence of ^{154}Sm, although it had been considered as a possible example of γ vibration. In parallel, we developed the shell-model code equipped with a novel eigensolver for massively parallel computation.

The 17th CNS International Summer School (CNSSS18) has been organized in August 2018 with many invited lecturers including four foreign distinguished physicists.

Finally, I thank Mr. Osugi and other administrative staff members for their heartful contributions throughout the year.

Susumu Shimoura
Director of CNS
S. Shimoura

Table of Contents

1a. Experimental Nuclear Physics: Low and Intermediate Energies

1b. Experimental Nuclear Physics: PHENIX Experiment at BNL-RHIC and ALICE Experiment at CERN-LHC

2. Accelerator and Instrumentation

3. Theoretical Nuclear Physics

4. Other Activities

Appendices

Experimental Nuclear Physics: Low and Intermediate Energies

Neutron capture cross section on ^{79}Se via the surrogate reaction

N. Imai, M. Dozono, S. Michimasa, S. Ota, T. Sumikama[a], D. Suzuki[a], O. Beliuskina, S. Hayakawa, C. Iwamoto, K. Kawata, N. Kitamura, S. Masuoka, P. Schrock, H. Shimizu, S. Shimoura, K. Wimmer[1b], K. Yako, H. Yamaguchi, L. Yang, N. Chiga[a], D. Nagae[a], S. Omika[a], H. Otsu[a], H. Sakurai[a], K. Yamada[a], S. Takeuchi[c], H. Miki[c], H. Yamada[c], S. Kawase[d], K. Nakano[d], Y. Watanabe[d], K. Iribe[e], T. Teranishi[e], N. Aoi[f], E. Ideguchi[f], H.J. Ong[f], R. Yanagihara[f]

Center for Nuclear Study, Graduate School of Science, University of Tokyo
[a]RIKEN Nishina Center
[b]Department of Physics, Univ. of Tokyo
[c]Tokyo Insititute of Technology
[d]Department of Advanced Energy Science and Engineering, Kyushu Univ.
[e]Department of Physics, Kyushu Univ.
[f]RCNP, Osaka Univ.

^{79}Se, which has a half-life as long as 3.3×10^5 years, is one of the long-lived fission products (LLFPs) of the nuclear wastes. It is supposed to be stored for millions of years in the deep geological repository, which has not been determined yet in Japan [1]. The ImPACT program aims to propose an alternative way to reduce the LLFPs by accelerator-driven transmutation. Among the nuclear reactions, generally, neutron-induced reaction is one of the effective ways to transmute nuclei in terms of the cross section as well as the mean-free path of neutron due to its chargeless property. To design the facility for the transmutation, cross sections of any neutron induced reactions are highly demanded to be measured. However, because of the radioactivity and the chemical property of the selenium isotopes, the neutron-induced reactions such as (n,γ) and $(n,2n)$ on ^{79}Se have never been measured.

In the present study, the cross section of ^{79}Se(n,γ) was studied with a surrogate ratio technique [3]. In general the neutron capture reaction can be expressed with two factors; the formation cross section of the compound states and the γ decay probability from the unbound states. The first term can be calculated precisely by using the global optical potential. On the other hand, the γ emission probability strongly depends on the nuclear structure of the nucleus. Once the γ emission probability can be obtained experimentally, we can determine the neutron capture cross sections. In the surrogate method, the γ emission probability is evaluated through the direct reaction such as (*d, p*) reaction. However, because the reaction mechanism is different between (n,γ) and (*d, p*) reaction, the experimental γ emission probabilities would not be identical with each other. The discrepancy may be caused by the different spin parity distributions populated by the respective reactions. In the surrogate ratio method, the mismatch is considered to be compensated with the experimental data of neighboring nuclei. In the present study, we used the ^{77}Se(*d, p*)^{78}Se reaction. Because ^{77}Se(n,γ) reaction was directly measured at 550 keV [5] and the theoretical curves are identical within 20% difference, the discrepancy between (n,γ) and (*d, p*) reaction can be reduced to be within 20%.

In a conventional way, the γ decay probability is determined by measuring γ rays. However, the probability largely depends on γ decay schemes. There may be also a chance in which the γ ray is emitted after the particle emission from the unbound state. In the Ref. [4] the number of transitions of low lying state after neutron transfer reaction was used to determine the γ emission probability with the help of the theoretical γ decay scheme using the statistical model. On the other hand, the γ emission probability was determined by identifying the reaction residue in coincidence with the recoiled particles without γ rays. Comparing the yields of ^{80}Se and ^{79}Se measured at the same excitation energy determined by the momentum of recoiled protons can give the γ decay probability from the unbound state in ^{80}Se. The measurement became feasible due to the inverse kinematics.

The secondary ^{77,79}Se beams were produced at RIBF by the in-flight fission of ^{238}U beams with a rotating Be target of 3 mm thickness. By tuning the thicknesses of the degraders at F1 and F2 the beam energy was adjusted to 120 MeV/nucleon at F5. The beam energy was further degraded with a thick Al degrader at F5 at 23 MeV/nucleon to achieve 20 MeV/nucleon at the secondary target after passing through the beam line detectors. Diamond detectors of 3×3 cm^2 and 300 μm thickness were placed at F3 and F5 to measure the timing when the beam passed through. The small active area of the diamond limited the momentum slit at F1 $\pm 1\%$. The parallel beam was made by the super conducting triplet quadrupole magnet at FE10, where the RF deflector is installed.

Two PPACs were installed upstream of the secondary target, FE12, to register the timing and the trajectory of the beams on the target. Time of flight (TOF) between F5 and FE12 was measured. Thanks to the high time resolution of diamond and PPACs, the TOF was enough to identify the beams. The RF deflector squeezed the beam spot in a diameter of 2 cm (σ) at a deuterated polyethylene CD_2 target of 4 mg/cm^2. The recoiled particles of (d,p) reactions were detected by six telescopes, each of which consisted of SSD and two CsI(Tl)s detectors. The telescope covered the scattering angles from 100 to 150 degrees. The SSD was

[1]Present Address:CISC, Madrid, Spain

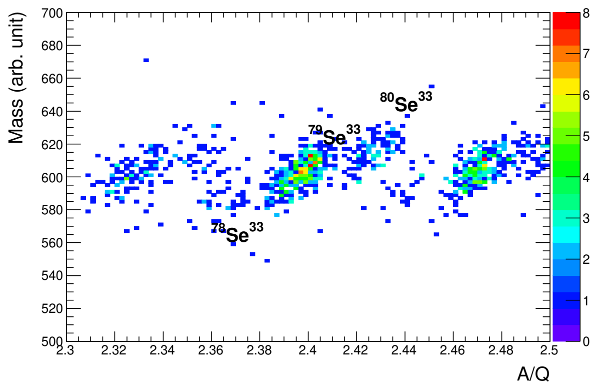

Figure 1. The mass of the residual outgoing nuclei as a function as a function of the A/Q ratio for ^{79}Se(d, p) reaction. The mass was determined by the Bragg curve analysis while the A/Q was obtained from the spectrometer of SHARAQ. ^{78,79,80}Se with three different charge states were observed.

divided to 16 channels in angle. The momentum of the outgoing particles ^{80}Se was analyzed by the first part of the SHARAQ spectrometer. At the exit of the D1 magnet, two PPACs and an ionization chamber were installed as the focal plane detectors. PPACs gave the TOF of ions. The ionization chamber yielded the energy loss (dE) and the range in the gas. The TOF-dE-range and $B\rho$ information enables us to identify the ions.

Figure 1 shows the mass of residual nuclei determined by the Bragg curve as a function of the charge-to-mass ratio (A/Q) determined by the SHARAQ spectrometer for ^{79}Se$(d,p)^{80}$Se reaction. Three charge states of the outgoing nuclei were observed. The figure displays that ^{80}Se^{33+} ions can be separated from ^{78}Se^{32+} although they cannot be distinguished clearly only in A/Q axis. Further analysis is on-going.

Acknowledgment

The work was funded by ImPACT Program of Council for Science, Technology and Innovation (Cabinet Office, Government of Japan).

References

[1] https://www.numo.or.jp/en/ .

[2] F. Kappler, H. Beer, and K. Wisshak, Rep. of Prog. in Phys. 52, 945 (1989).

[3] J. E. Escher et al., Rev. of Mod. Phys. 84, 353 (2012).

[4] R. Hatrarik et al., Phys. Rev. C **81**, 011602 (R) (2010).

[5] S. Kawada, M. Igashira, T. Katabuchi, and M. Mizumoto, J. Nucl. Sci. Tech. 47, 643 (2010).

Proton- and deuteron-induced reactions on ^{107}Pd at $20-30$ MeV/u

M. Dozono, N. Imai, S. Michimasa, T. Sumikama[a], N. Chiga[a], S. Ota, O. Beliuskina, S. Hayakawa, K. Iribe[b], C. Iwamoto, S. Kawase[c], K. Kawata, N. Kitamura, S. Masuoka, K. Nakano[c], P. Schrock, D. Suzuki[a], R. Tsunoda, K. Wimmer[d], D. S. Ahn[a], N. Fukuda[a], E. Ideguchi[e], K. Kusaka[a], H. Miki[f], H. Miyatake[g], D. Nagae[a], M. Nakano[h], S. Ohmika[a], M. Ohtake[a], H. Otsu[a], H. J. Ong[e], S. Sato[h], H. Shimizu, Y. Shimizu[a], H. Sakurai[a], X. Sun[a], H. Suzuki[a], M. Takaki, H. Takeda[a], S. Takeuchi[f], T. Teranishi[b], H. Wang[a], Y. Watanabe[c], Y. X. Watanabe[g], H. Yamada[f], H. Yamaguchi, R. Yanagihara[e], L. Yang, Y. Yanagisawa[a], K. Yoshida[a], and S. Shimoura

Center for Nuclear Study, the University of Tokyo
[a]RIKEN Nishina Center
[b]Department of Physics, Kyushu University
[c]Department of Advanced Energy Engineering Science, Kyushu University
[d]Department of Physics, the University of Tokyo
[e]Research Center for Nuclear Physics, Osaka University
[f]Department of Physics, Tokyo Institute of Technology
[g]WNSC, IPNS, KEK
[h]Department of Physics, Rikkyo University

The nuclear transmutation of long-lived fission products (LLFPs), which are produced in nuclear reactors, is one of the candidate techniques for the reduction and/or reuse of LLFPs. To design optimum pathways for the transmutation process, several nuclear reactions have been studied by using LLFPs as secondary beams. The studies indicate that proton- and/or deuteron-induced spallation reactions at intermediate energies ($100-200$ MeV/nucleon) are sufficiently effective for the LLFP transmutation [1–3]. We note that protons/deuterons lose their energies in materials; therefore, measurements at lower reaction energies are definitely desired for the application of transmutation. In this study, the isotopic production cross sections of proton- and deuteron-induced reactions on ^{107}Pd and ^{93}Zr at $20-30$ MeV/nucleon were measured under an inverse kinematics condition. The experiment was conducted at the OEDO [4] beamline, which is used to deccelerate the unstable nuclei beam at RIBF. This was the first physics experiment using OEDO. This report describes the current status of the analysis on ^{107}Pd data. The status of the ^{93}Zr data analysis is reported by J. W. Hwang *et al.* [5].

Detailed descriptions of the setup and procedure can be found in Ref. [6]. A secondary beam was produced by the in-flight fission of a ^{238}U primary beam at 345 MeV/u on a Be target with a thickness of 5 mm. The beam was degraded and purified by using an Al degrader at the focus F1 and further degraded by using another Al degrader at F5. The purity of ^{107}Pd was 37%, and its energy was 32 MeV/u in front of the secondary target. Another setting was used to study the reaction at a lower beam energy of 26 MeV/u. The OEDO device, which consists of a radio-frequency deflector and two superconducting triplet quadrupole magnets, was employed to reduce the beam spot size, and the resulting size was 45 mm in FWHM on the secondary target. The typical beam intensity was 10^4 pps.

The secondary targets, H_2 and D_2, were prepared as high-pressure cooled gas targets. The temperature was 40 K, and the pressure was adjusted to $7.5(15)$ mg/cm^2 for H_2 (D_2). In order to obtain the background contribution, empty-target measurements were also carried out.

Reaction residues were analyzed by the SHARAQ spectrometer and detected by two PPACs [7] and an ionization chamber [8] located at the focal plane. Position and timing information of PPACs were used to deduce the velocity (β) and magnetic rigidity ($B\rho$). The ionization chamber measured the energy loss (ΔE) and range (R). The mass-to-charge ratio A/Q, atomic number Z, and mass number A, were obtained from $B\rho-\beta$, $\Delta E-\beta$, and $R-\beta$ correlations, respectively. In order to cover a broad range of reaction products, several different $B\rho$ settings ($\Delta(B\rho)/B\rho = -7\%$, -3%, $+1\%$, $+5\%$ and $+9\%$ relative to the $B\rho$ value of the secondary beam) were applied in the SHARAQ spectrometer.

A example of the particle identification plot for reaction residues produced from the ^{107}Pd beam is shown in Fig. 1. The example was taken by using the 32 MeV/u beam and the H_2 target with the -3% SHARAQ setting. Figure 1(a) displays a correlation plot of Z versus A/Q, and (b) and (c) show correlation plots of A versus A/Q for Ag and Pd isotopes, respectively. The resolutions in A, Z and A/Q were 1.6 (FWHM), 0.40 (FWHM) and 1.3×10^{-2} (FWHM), respectively. Thanks to the good resolutions, particles were unambiguously distinguished from each other.

The isotopic production cross sections of the proton-induced reactions on ^{107}Pd are shown in Fig. 2. The symbols show the present measurement at 32 MeV/u. Considering the energy loss of the beam in the target, the measured cross sections are the ones averaged over $25-30$ MeV/u, which is shown by the hatched region. The error bars represent statistical uncertainties only. The sensitivity threshold of the measurement was 5 mb because of its statistics. We determined cross sections for five isotopes ($^{107-105}$Ag and

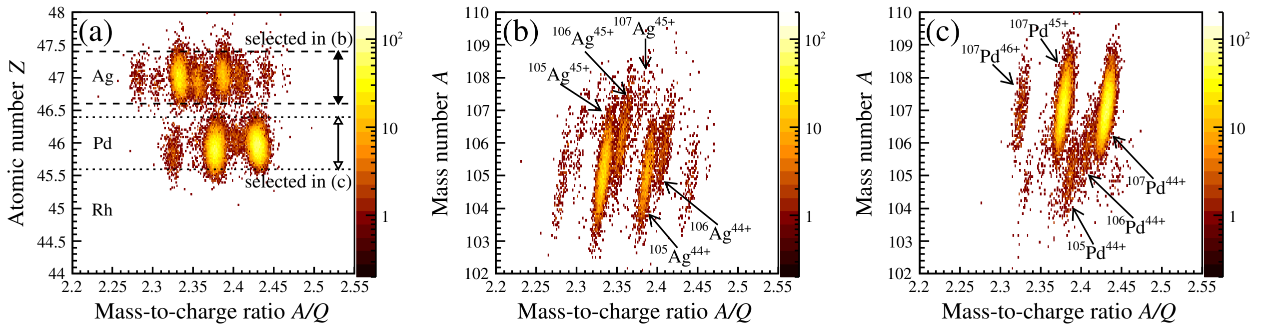

Figure 1. Particle identification plots for reaction residues using the SHARAQ spectrometer: (a) Correlation plot of Z versus A/Q. (b), (c) Correlation plots of A versus A/Q for Ag and Pd isotopes.

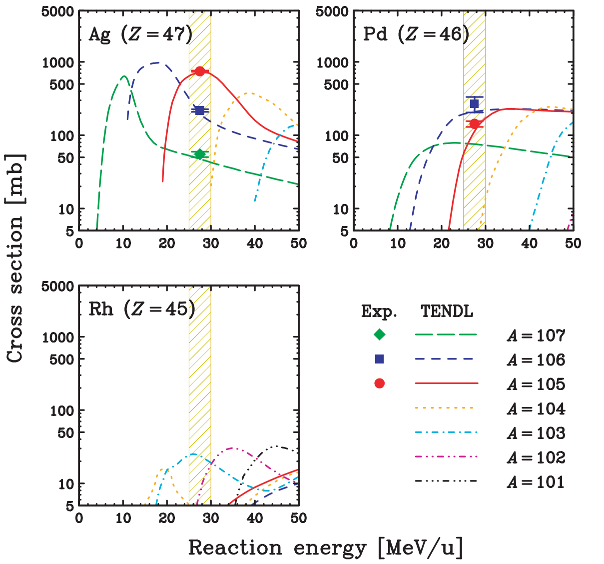

Figure 2. Cross sections for Ag, Pd, and Rh isotopes produced by proton-induced reactions on ^{107}Pd as a function of reaction energy. The symbols show the present measurement at 32 MeV/u and the curves TENDL-2017 [9] evaluation. Considering the energy loss of the beam in the target, the measured cross sections are the ones averaged over 25 – 30 MeV/u (hatched region).

$^{106-105}$Pd).

The results show a major production of Ag isotopes; about 70% of the total cross section is exhausted by Ag isotopes. This can be understood by the compound-nuclear process: $^{107}\mathrm{Pd} + p \rightarrow {}^{108}\mathrm{Ag}^*$. The Ag isotopes are probably produced by an evaporation of neutrons from the highly excited compound nucleus $^{108}\mathrm{Ag}^*$. Actually, the trend is completely different from the high-energy spallation reaction case [2], in which the contribution of Ag isotopes is less than 10%.

The curves in Fig. 2 show the excitation functions evaluated by TENDL-2017 [9]. The general behavior of the cross sections is well reproduced by the evaluation.

The present data, as well as higher-energy data, would provide an effective guideline for a possible solution of the LLFP transmutation. The results will be finalized soon. For the 26 MeV/u beam data, the analysis for particle identification is ongoing.

This work was funded by the ImPACT Program of the Council for Science, Technology and Innovation (Cabinet Office, Government of Japan).

References

[1] H. Wang *et al.*, Phys. Lett. **B754** (2016) 104.
[2] H. Wang *et al.*, Prog. Theor. Exp. Phys. **2017** (2017) 021D01.
[3] S. Kawase *et al.*, Prog. Theor. Exp. Phys. **2017** (2017) 093D03.
[4] S. Michimasa and S. Shimoura, Nucl. Phys. News **28(4)** (2018) 21.
[5] J. W. Hwang *et al.*, in this report.
[6] K. Iribe *et al.*, CNS Annual Report 2017, CNS-REP-**97** (2019) 5.
[7] H. Kumagai *et al.*, Nucl. Instrum. Methods Phys. Res. B **317** (2013) 717.
[8] N. Chiga *et al.*, RIKEN Accel. Prog. Rep. **50** (2017) 164.
[9] A. J. Koning *et al.*, TENDL-2017: TALYS-based evaluated nuclear data library, https://tendl.web.psi.ch/tendl_2017/tendl2017.html (2017).

R-matrix analysis of the ^{7}Be + n reactions and its astrophysical implications

S. Hayakawa[a], M. La Cognata[b], L. Lamia[b,c], H. Shimizu[a], L. Yang[a], H. Yamaguchi[a], K. Abe[a], O. Beliuskina[a], S. M. Cha[d], K. Y. Chae[d], S. Cherubini[b,c], P. Figuera[b,c], Z. Ge[e], M. Gulino[b,f], J. Hu[g], A. Inoue[h], N. Iwasa[i], D. Kahl[j], A. Kim[k], D. H. Kim[k], G. Kiss[e], S. Kubono[a,e,g], M. La Commara[l,m], M. Lattuada[b,c], E. J. Lee[d], J. Y. Moon[n], S. Palmerini[o,p], C. Parascandolo[m], S. Y. Park[k], D. Pierroutsakou[m], R. G. Pizzone[b,c], G. G. Rapisarda[b], S. Romano[b,c], C. Spitaleri[b,c], X. D. Tang[g], O. Trippella[o,p], A. Tumino[b,f], P. Vi[e], and N. T. Zhang[g]

[a] *Center for Nuclear Study, Graduate School of Science, University of Tokyo*
[b] *Istituto Nazionale di Fisica Nucleare - Laboratori Nazionali del Sud*
[c] *Department of Physics and Astronomy, University of Catania*
[d] *Department of Physics, Sungkyunkwan University*
[e] *RIKEN Nishina Center*
[f] *Faculty of Engineering and Architecture, Kore University of Enna*
[g] *Institute of Modern Physics, Chinese Academy of Sciences*
[h] *Research Center for Nuclear Physics, Osaka University*
[i] *Department of Physics, Tohoku University*
[j] *School of Physics and Astronomy, University of Edinburgh*
[k] *Department of Physics, Ewha Womans University*
[l] *Depart. of Phys. 'E. Pancini', University of Naples Federico II*
[m] *Istituto Nazionale di Fisica Nucleare - Section of Naples*
[n] *Institute for Basic Science (IBS)*
[o] *Istituto Nazionale di Fisica Nucleare - Section of Perugia*
[p] *Department of Physics and Geology, University of Perugia*

We have performed indirect measurements of the ^{7}Be$(n,\alpha)^4$He and the ^{7}Be$(n,p)^7$Li reactions via the ^{2}H$(^7$Be$,2\alpha)^1$H and the ^{2}H$(^7$Be$,^7$Li$p)^1$H reactions, respectively, by means of the Trojan Horse Method (THM) [1] at Center for Nuclear Study Radioactive Isotope Beam separator [2]. Those two reactions are responsible for reduction of the primordial ^{7}Li abundance produced in the Big-bang nucleosynthesis (BBN), which act to reduce the discrepancy between its observation and prediction known as the cosmological ^{7}Li problem [3]. Here we report the progress of the *R*-matrix analysis applying to the results previously reported in Ref [4].

With a simple assumption of the plane wave approximation, the THM provides the triple differential cross section of the ^{2}H$(^7$Be$,2\alpha)^1$H (or ^{2}H$(^7$Be$,^7$Li$p)^1$H) reaction proportional to the product of the kinematic factor, the Fourier transform of the radial wave function of the deuteron nucleus, and the cross sections of the half-off energy-shell (HOES) ^{7}Be$(n,\alpha)^4$He (or ^{7}Be$(n,p)^7$Li) reaction of interest. The HOES cross section should be corrected to the on-energy-shell (OES) one by multiplying it by the Coulomb- and centrifugal-barrier penetrability, and the externally normalized to the existing cross section data. Obviously the Coulomb barrier is absent in the neutron-induced reaction that we performed. In our case, the ^{7}Be$(n,\alpha)^4$He excitation function is expected to be characterized mostly by the *p*-wave resonant states due to the parity conservation, and the *p*-wave-corrected excitation function appears also consistent with the known data [5, 6]. For the ^{7}Be$(n,p_0)^7$Li reaction (where p_i represents the *i*th excited-state transition in ^{7}Li), the *s*-wave penetrability (thus no centrifugal barrier) seems consistent with the data deduced from the time-reversal reactions [7, 8], and also with the existence of the *s*-wave 2^- state near the neutron threshold as mentioned later. We derived the p_0/p_1 ratio of the HOES cross sections from the Gaussian fitting to the *Q*-value spectra [4]. The ^{7}Be$(n,p_1)^7$Li* channel is observed for the first time around the BBN energies, and assumed to be corrected and normalized in the same manner as the (n,p_0) channel. The normalized ^{7}Be$(n,p_1)^7$Li* cross section may be smoothly connected from mega electron volts to the thermal neutron data [9, 10] by the $1/v$ law.

A multi-channel *R*-matrix analysis was desired to confirm the penetrability correction and the normalization of the present THM data more strictly from the point of view of the resonance structure in the compound nucleus ^{8}B. It may also help with interpolation and extrapolation of the data for the reaction rate calculation. We expect that a comprehensive explanation of the these three channels may confirm the reliability of both the present and the previous data.

In the previous *R*-matrix analysis work [13], four dominant partial waves were selected, which characterize the basic resonant features of the ^{7}Be$(n,p)^7$Li reaction; 1) the 2^- resonance at $E_x = 18.91$ MeV ($E_{\mathrm{c.m.}} = 2.7$ keV) dominantly enhances the cross section in a wide energy range from the neutron threshold up to mega electron volts, 2) the resonance at $E_{\mathrm{c.m.}} \sim 330$ keV corresponds to the doublet 3^+ states at 19.07 and 19.24 MeV which are supposed to have

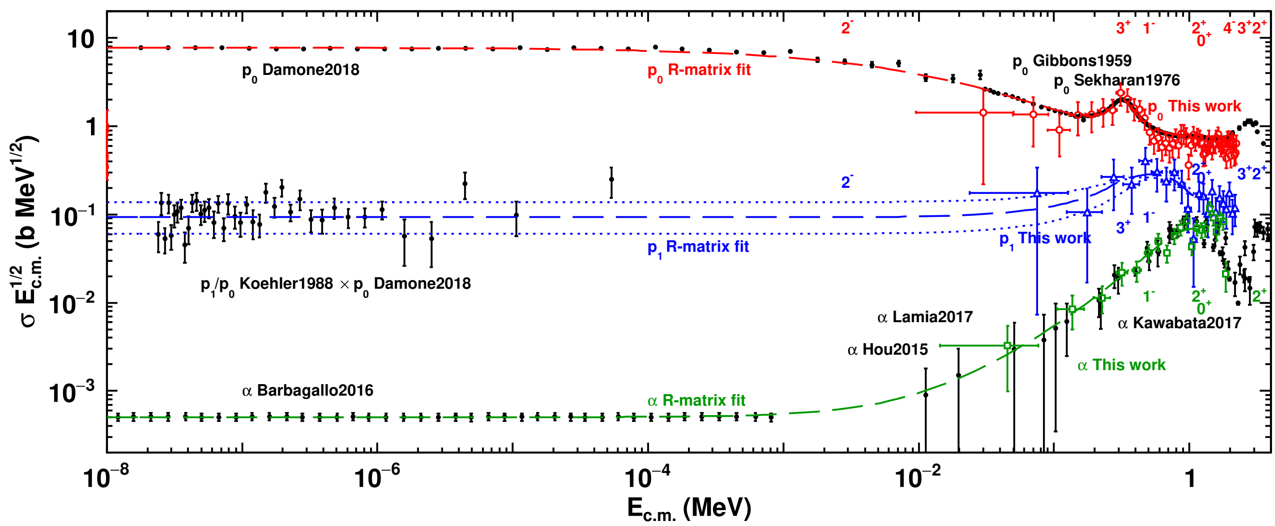

Figure 1. The cross section data of the $^{7}\mathrm{Be}(n,p_0)^{7}\mathrm{Li}$, the $^{7}\mathrm{Be}(n,p_1)^{7}\mathrm{Li}^{*}$and the $^{7}\mathrm{Be}(n,\alpha)^{4}\mathrm{He}$ reactions used for the multi-channel R-matrix analysis. The labels refers to the origins the present and the previous data [5–12]. The dashed lines represent the preliminary R-matrix fitting to the data of each reaction channel. The dotted lines above and the below the $^{7}\mathrm{Be}(n,p_1)^{7}\mathrm{Li}^{*}$ channel R-matrix fitting. The spins and parties indicate the resonant states adopted for the present R-matrix analysis.

different isospin structures: the former essentially decays through proton emission whereas the latter presents a substantial ratio in the neutron channel, thus only the latter was adopted, 3) the 3^+ state at 21.5 MeV well reproduce the resonance at $E_{\mathrm{c.m.}} \sim 2.66$ MeV, 4) a 2^+ non-resonant state was needed to express the high-energy enhancement of the cross section as the "background contribution".

Based on the above studies, we expanded the R-matrix analysis to the p_1 and α channels as well on simple conditions as follows; 1) fixing the known J^π and the resonance energies, 2) adopting partial waves with only $l \leq 3$ angular momenta, 3) excluding the excited states with no neutron emission reported, 4) fitting only at $E_{\mathrm{c.m.}} < 1.2$ MeV. The R-matrix fitting was performed using AZURE2 code [14]. The procedure of fitting is then; 1) starting from the n and p_0 channels with parameters taken from Ref. [13], 2) fixing the p_0 parameters, and fitting only the n, p_1 and the α channels, 3) fixing the p_1 and α channels, and fitting the n and p channels again, 4) fixing converged parameters and iterating the above. Then the χ^2 apparently converged close to unity. We could reproduce the basic features of these excitation functions [5–12] including the present p_1 data simultaneously as shown in Fig. 1, with most partial widths not to violate the known total widths nor the Wigner limits. The spin-parity notations in Fig. 1 indicate the locations of the resonant states adopted for the R-matrix analysis. The peak in the (n,p_1) channel around $E_{\mathrm{c.m.}} \sim 0.5$ MeV is very likely to arise from the s-wave 1^- resonance at $E_x = 19.5$ MeV, which supports the penetrability correction described above. The dotted lines in Fig. 1 reflect the possible (n,p_1) range obtained by varying the p_1 partial width and the resonance energy of the 1^- state to reproduce the 1σ deviation from the best-fit one. This state was supposed to have a total width of 500 keV [15], while we found that it may have a total width of about $1^{+0.2}_{-0.15}$ MeV, and a relatively small p_0 width and a large p_1 width. Accordingly, the (n,p_1) reaction cross section would amount up to about 1/10 of that of (n,p_0) at the relevant energies below 100 keV. By combining the above result and the latest (n,p_0) reaction cross section [10], the total $^{7}\mathrm{Be}(n,p)^{7}\mathrm{Li}$ reaction rate may be about 15% higher than that of Ref. [3] in the BBN temperature range, which may result in about a 10% reduction of the primordial $^{7}\mathrm{Li}$ abundance according to the known sensitivity to this reaction [3]. Definitive numbers of the resonance parameters will come out with further data analysis and confirmation.

This experiment was performed at RI Beam Factory operated by RIKEN Nishina Center and CNS, University of Tokyo, and supported by JSPS KAKENHI (Grant No. 15K17631).

References

[1] C. Spitaleri *et al.*, Phys. Atom. Nucl. **74**, 1725 (2011).
[2] Y. Yanagisawa *et al.*, NIM A **539**, 74 (2005).
[3] R. H. Cyburt *et al.*, Rev. Mod. Phys. **88**, 015004 (2016).
[4] S. Hayakawa *et al.*, **CNS-REP-97**, 13 (2019).
[5] S. Q. Hou *et al.*, Phys. Rev. C **91**, 055802 (2015).
[6] T. Kawabata *et al.*, Phys. Rev. Lett. **118**, 052701 (2017).
[7] R. Macklin and J. Gibbons, Phys. Rev. **109**, 105 (1958).
[8] K. Sekharan *et al.*, NIM **133**, 253 (1976).
[9] P. Koehler *et al.*, Phys. Rev. C **37**, 917 (1988).
[10] L. A. Damone *et al.*, Phys. Rev. Lett. **121**, 042701 (2018).
[11] M. Barbagallo *et al.*, Phys. Rev. Lett. **117**, 152701 (2016).
[12] L. Lamia *et al.*, Astrophys. J. **850**, 175, (2017).
[13] A.Adahchour and P.Descouvemont, JPG **29**, 395 (2003).
[14] R. E. Azuma *et al.*, Phys. Rev. C **81**, 045805, (2010).
[15] F. Ajzenberg-Selove, Nucl. Phys. A **523**, 1, (1991).

Breakup reaction mechanism study of ^{17}F at energies near the Coulomb Barrier

N. R. Ma[a,b], L. Yang[a,b], C. J. Lin[b,j], H. Yamaguchi[a], D. X. Wang[b], L. J. Sun[b], M. Mazzocco[c,d], H. M. Jia[b], S. Hayakawa[a], D. Kahl[a], S. M. Cha[e], G. X. Zhang[f], F. Yang[b], Y. Y. Yang[g], C. Signorini[c,d], Y. Sakaguchi[a], K. Abe[a], M. La Commara[h], D. Pierroutsakou[i], C. Parascandolo[i], E. Strano[c,d], A. Kim[e], K. Y. Chae[e], M. S. Kwag[e], G. L. Zhang[f], M. Pan[f], X. X. Xu[b], P. W. Wen[b], F. P. Zhong[b,j], and H. H. Sun[b]

[a] *Center for Nuclear Study, Graduate School of Science, University of Tokyo*
[b] *Department of Nuclear Physics, China Institute of Atomic Energy*
[c] *Department of Pharmacy, University Federico*
[d] *Department of Physics, Sungkyunkwan University*
[e] *Dipartimento di Fisica, Universita di Padova*
[f] *Istituto Nazionale di Fisica Nucleare-Sezione di Padova*
[g] *Istituto Nazionale di Fisica Nucleare-Sezione di Napoli*
[h] *Institute of Modern Physics, Chinese Academy of Sciences*
[i] *School of Physics and Nuclear Energy Engineering, Beihang University*
[j] *Department of Physics, Guangxi Normal University*

Weakly-bound nuclei, which have been extensively investigated in the past few decades [1], have typical feature that they can easily break into smaller fragments and populate the continuum states when approaching the strong Coulomb or nuclear fields of a target nucleus. These continuum states may strongly couple to the low-lying discrete states and change the reaction process greatly, which is the so-called breakup effect.

In recent years a number of radioactive ion beam lines such as IMP-RIBLL1. [2] and CNS-CRIB. [3] have been built, which has greatly broadened our ability to study the reaction dynamic induced by weekly bound stable and unstable nuclei. But due to the variety and complexity of reaction products, especially for the breakup reactions of heavy exotic nuclei at energies near the Coulomb barrier, a detector array with powerful particle identification capability in a large range of Z values and energies with energy threshold as low as possible is needed. With ionization chamber as the first layer to derive the required low energy thresholds, a lightweight Multilayer Ionization-chamber (IC) Telescope Array (MITA) for detecting the reaction products induced by heavy weakly bound nuclei at energies near the Coulomb barrier was developed [4]. MITA consists ten independent and identical telescopes, where each individual unit consists of four stages of detectors: one IC and three following silicon detectors, as is shown in Figure. 1.

MITA has been successfully used in the reaction mechanism study of proton-dripline ^{17}F+^{58}Ni system [5] at the low-energy radioactive isotope beam separator CRIB. Primary analysis showed that the energy distribution of oxygen measured by the telescope coincident well with the Moute Carlo simulation results, and the angular distribution of ^{16}O from direct reactions of ^{17}F+^{58}Ni proved that non-elastic breakup is the major contribution for the direct reactions.

With the fusion-evaporation protons and/or alphas measured by MITA, the fusion reaction cross section of ^{17}F+^{58}Ni can be deduced [6]. Figure. 2 showed the typical energy spectra of protons and alphas at E_{lab} = 63.1 MeV and also the calculation results with the code PACE2 [7]. In the PACE2 calculations, the level density parameter a is fixed to be a=A/7.6 [8], while for all the other various input parameters, default values were adopted. In addition, the experimental fusion cross sections σ_{exp} were used as an input in an iterative way, and then the code internally shifts the respective optical-model transmission coefficients to reproduce these values [6, 8].

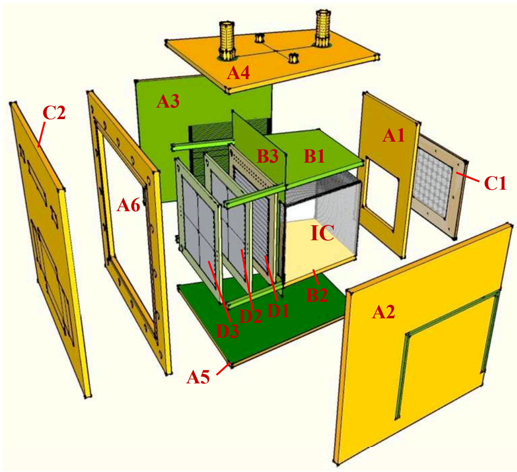

Figure 1. (Color online) General assembly diagram of the IC-based detector telescope.
(A1-Front plate A2-Left plate A3-Right plate A4-Roof plate A5-Floor plate A6-Screw-hole plate B1-Anode plate B2-Cathode plate B3-Back window plate C1-Front window plate C2-Back plate D1-64 μm DSSD D2-300 μm QSD D3-1000 μm QSD.)

As shown in Figure. 2 (a), for alpha events with energy higher than 11.5 MeV the distribution is consistent with

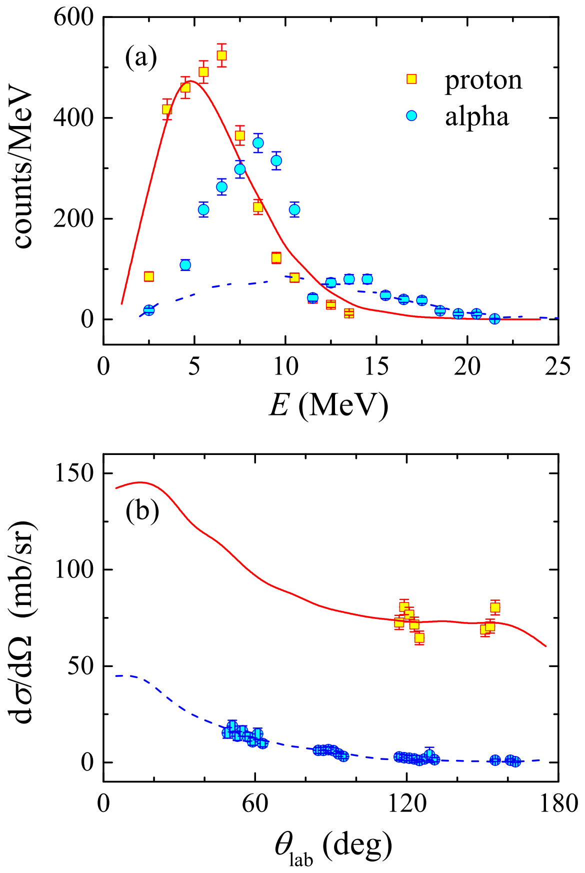

Figure 2. (Color online) Typical energy spectra (a) and angular distributions (b) of proton (squares) and alpha (circles) at E_{lab} = 63.1 MeV. The solid and dashed curves denote the PACE2 calculation results for the cases of proton and alpha, respectively.

the prediction of PACE2, which indicates that only the alphas within this energy region are mainly from the fusion-evaporation process. While for alpha events with energy of about 9 MeV a large difference appeared between the experimental result and the theoretical prediction, a further investigation is required for the large yield of the such alpha particles.

For the case of protons, in order to exclude the contribution from breakup events, only the events at backward angles ($\theta_{lab} > 115°$) were considered. As shown in Figure. 2 (a), the energy distribution of the protons can be reproduced accurately by the PACE2 calculations, indicating that the contributions from breakup can be safely neglected in the backward angular region. A further CDCC calculation is required to more rigorously investigate the influence arising from breakup reactions. The angular distributions of selected fusion-evaporation alphas and protons are shown in Figure. 2 (b), where the solid and dashed curves represent the PACE2 calculation results for protons and alphas, respectively.

Further data analysis of this experiment is still in progress, and the results will be published later.

References

[1] L. F. Canto, P. R. S. Gomes, R. Donangelo *et al.*, Phys. Rep. **596** (2015) 1.

[2] J. J. He, S. W. Xu, P. Ma *et al.*, Nucl. Instrum. Meth. A 680 (2012) 43-47.

[3] Y. Yanagisawa, S. Kubono, T. Teranishi., Nucl. Instrum. Meth. A 539 (2005) 74-83.

[4] N. R. Ma, L. Yang, C. J. Lin *et al.*, Eur. Phys. J. A **55** (2005) 87.

[5] L. Yang, C. J. Lin, N. R. Ma *et al.*, CNS Annual Report 2017 CNS-REP-**97** (2019) 15 - 16.

[6] E. F. Aguilera *et al.*, Phys. Rev. Lett. **107** (2011) 092701.

[7] A. Gavron, Phys. Rev. C **21** (1980) 230.

[8] P. Amador-Valenzuela *et al.*, J. Phys. Conf. Ser. **492** (2014) 012003.

New measurement of ^{8}Li(α,n)^{11}B reaction

Y. Mizoi[a,b,c], H. Baba[c], A. Bracco[d,e], F. Camera[d,e], S. M. Cha[f], K. Y. Chae[f], S. Cherubini[c,g,h], H. S. Choi[i], N. N. Duy[f], T. Fukuda[a,c,j], S. Hayakawa[b], Y. Hirayama[k], N. Imai[b], H. Ishiyama[c], A. Kim[l], D. H. Kim[f], N. Kitamura[b], S. Kubono[b,c], M. S. Kwag[f], S. Michimasa[b], M. Mihara[c,m], H. Miyatake[k], S. Ota[b], R. G. Pizzone[g], H. Shimizu[b,c], N. K. Uyen[f], R. Wakabayashi[c,m], Y. X. Watanabe[k], O. Wieland[d], H. Yamaguchi[b], L. Yang[b], N. Zhang[b,n] and Z. C. Zhang[n]

[a] *Center for Physics and Mathematics, Institute for Liberal Arts and Sciences, Osaka Electro-Communication University*
[b] *Center for Nuclear Study, the University of Tokyo*
[c] *RIKEN Nishina Center*
[d] *Istituto Nazionale di Fisica Nucleare (INFN) - Sezione di Milano*
[e] *Dipartimento di Fisica dell'Università degli Studi di Milano*
[f] *Department of Physics, Sungkyunkwan University*
[g] *Istituto Nazionale di Fisica Nucleare (INFN) - Laboratori Nazionali del Sud (LNS)*
[h] *Dipartimento di Fisica ed Astronomia, Università di Catania*
[i] *Department of Physics and Astronomy, Seoul National University*
[j] *Research Center for Nuclear Physics (RCNP), Osaka University*
[k] *Wako Nuclear Science Center (WNSC), Institute of Particle and Nuclear Studies (IPNS), High Energy Accelerator Research Organization (KEK)*
[l] *Department of Physics, Ewha Womans University*
[m] *Department of Physics, Osaka University*
[n] *Institute of Modern Physics (IMP), Chinese Academy of Science (CAS)*

1. Introduction

The ^{8}Li(α,n)^{11}B reaction is considered to be the key reaction in the inhomogeneous Big Bang [1–3] and type-II supernova nucleosyntheses [4, 5], and has been studied in experiments [6–13] for thirty years. Especially, we have been providing cross-section data [7–13] on this reaction for more than twenty years with using ^{8}Li RI beams.

The previous results [7–13] are summarized in Fig. 1. The Gamow-peak widths, whose energy regions of $T_9 = 1$ and 2 are important for the Big Bang and supernova nucleosyntheses, respectively, are also indicated in Fig. 1.

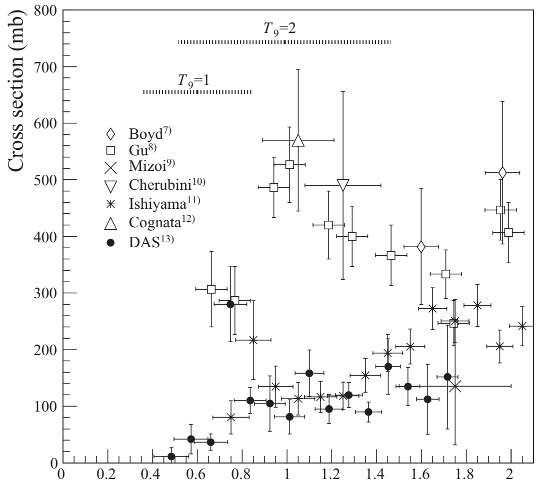

Figure 1. Excitation functions of ^{8}Li(α,n)^{11}B reaction.

We can see in Fig. 1 that the cross-sections obtained by the previous experiments have large differences around $E_{\rm cm} = 1.0$ MeV. The previous experiments were performed by two different methods: inclusive and exclusive. The former detected either ^{11}B [7, 8] or neutron [10, 12] and the latter [9, 11, 13] detected both ^{11}B and neutron by measuring their kinetic energies and angles. The cross-sections of the former results are larger than the latter ones systematically. The largest discrepancy appears at the center energy of $T_9 = 2$ region and its value is a factor of five. We could presume the discrepancies might originate from the experimental methods, but we have no experimental fact to investigate them.

2. Experiment

In order to solve this problem, we proposed a new *inclusive* measurement. Figure 2 shows the level schemes relevant to the ^{8}Li(α,n)^{11}B reaction. As shown in Fig. 2, we expect that the highly-excited states of ^{11}B might be produced by this reaction, however the previous experiments did not measure the γ-rays. Thus we performed a new experiment to measure the γ-rays emitted from ^{11}B*. Considering that the expected γ-ray energies are between 2 and 8 MeV, we employed a large volume 3.5”×8” LaBr$_3$:Ce detector [14] provided by INFN Milano. We also installed 850 mm×150 mm×50 mm plastic and 50 mm$^{\phi}$ × 10 mm ^{6}Li-glass scintillators to detect neutrons by covering wide energy ranges between a few ten keV to 10 MeV for reference to the previous experiments. The plastic scintillator has an energy threshold of a few hundred keV for detecting neutrons. The ^{6}Li-glass scintillator has good detection efficiencies for neutrons whose energies are below a few hundred keV.

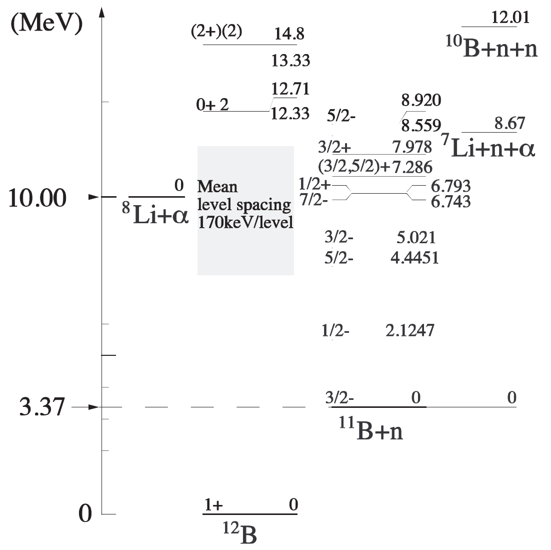

Figure 2. Level schemes relevant to ^{8}Li(α,n)^{11}B reaction. Vertical energy scale is adjusted to excitation energy of intermediate state of ^{12}B. Reaction energy of $E_{\rm cm} = 0.0$ MeV equals to 10 MeV of excitation energy of ^{12}B.

This experiment was performed at CRIB in September 2018. We placed a gas-target cell at F3, in which ^{4}He gas was filled at a pressure of 1.0 atm. Two LaBr$_3$:Ce detectors were placed closed to the ^{4}He-gas-target cell. Ten ^{6}Li-glass and six plastic scintillators were placed downstream of the gas-target cell with mean distances of 50 cm and 150 cm, respectively. The ^{8}Li beam, whose intensity was typically 300 kHz, was produced by the ^{7}Li(d,p)^{8}Li reaction. The primary ^{7}Li beam had an energy of 6.0 MeV/nucleon and an intensity of 250 particle nA. The D$_2$-gas production target had a thickness of 1.9 mg/cm^2. The energies of ^{8}Li particles measured inside the ^{4}He-gas target were between $E_{\rm cm} = 0.9$ and 1.9 MeV.

3. Preliminary result

We successfully obtained data with sufficient statistics. Although we faced difficulties in data analysis owing to the large background originating from thermal neutrons, we could identify the γ-rays emitted from ^{11}B*. Figure 3 shows the preliminary result of the γ-ray spectrum. By subtracting the huge background with considering timing information, we obtained this spectrum. We can observe some peak-like structures corresponding to the γ-ray energies from ^{11}B*.

4. Future outlook

For obtaining the γ-ray spectrum with rational quality, we should perform much more careful analysis. Due to the vast thermal-neutron background, we have difficulties in data of neutron detectors. We should do further research and development to resolve this problem. We are also doing computer simulations for determining efficiencies of detectors to derive absolute values of reaction cross section and branching ratios of the final states of ^{11}B. We expect that this experiment will provide new data to understand mechanism of the

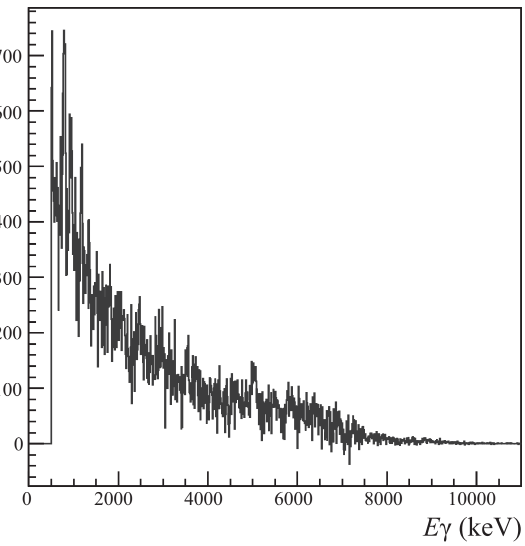

Figure 3. Energy spectrum obtained by one of LaBr$_3$:Ce detectors.

^{8}Li(α,n)^{11}B reaction and dynamics of the excited states of ^{11}B produced by this reaction.

Acknowledgments

This work is supported by JSPS KAKENHI, Grant Numbers JP17K05472. Fundamental Electronics Research Institute (FERI) of Osaka Electro-Communication University (OECU) and Center for Nuclear Science (CNS) of University of Tokyo partially support this work.

References

[1] J.H. Applegate *et al.*, Astrophys. J. **329**, 572 (1988).
[2] R.A. Malaney and W.A. Fowler, Astropys. J. **333**, 14 (1989).
[3] T. Kajino and R.N. Boyd, Astrophys. J. **359**, 359 (1990).
[4] M. Terasawa it et al., Astrophys. J. **562**, 470 (2001).
[5] T. Sasaqui *et al.*, Astrophys. J. **645**, 1345 (2006).
[6] T. Paradellis *et al.*, Z. Phys. A **337**, 211(1990).
[7] R.N. Boyd *et al.*, Phys. Rev. Lett. **68**, 1283 (1992).
[8] X. Gu *et al.*, Phys. Lett. B **343**, 31 (1995).
[9] Y. Mizoi *et al.*, Phys. Rev. C **62**, 065801 (2000).
[10]S. Cherubini *et al.*, Eur. Phys. J. **20**, 355 (2004).
[11]H. Ishiyama *et al.*, Phys. Lett. B **640**, 82 (2006).
[12]M.La Cognata, *et al.*, Phys. Lett. B **664**, 157 (2008).
[13]S.K. Das *et al.*, Phys. Rev. C **95**, 055805 (2017).
[14]A. Gaiz *et al.*, Nucl. Instrum. Methods Phys. Res. A **729**, 910 (2013).

Measurement of ^{25}Al+p elastic scattering relevant to the astrophysical reaction ^{22}Mg(α,p)^{25}Al

J. Hu[a], H. Yamaguchi, S. W. Xu[a], N. T. Zhang[a], S. B. Ma[a], L. H. Ru[a], E. Q. Liu[a], T. Liu[a], S. Hayakawa, L. Yang, H. Shimizu, D. Kahl[b], C. B. Hamill[b], A. Murphy[b], X. Fang[c], J. Su[d], K. Chae[e], M. Kwag[e], S. Cha[e], N. N. Duy[e], N. K. Uyen[e], D. Kim[e], G. Pizzone[f], M. L. Cognata[f], S. Cherubini[f], S. Romano[f], A. Tumino[f], J. Liang[g], A. Psaltis[g], M. Sferrazza[g], D. H. Kim[h] and S. Kubono[i]

Center for Nuclear Study, Graduate School of Science, University of Tokyo
[a]Institute of Modern Physics, Chinese Academy of Sciences, China
[b]School of Physics & Astronomy, University of Edinburgh, United Kingdom
[c]School of Physics, Sun Yet-sen University, China
[d]College of Nuclear Science and Technology, Beijing Normal University, China
[e]Department of Physics, Sungkyunkwan University, Korea
[f]INFN-LNS, Laboratori Nazionali del Sud, Italy
[g]Department of Physics & Astronomy, McMaster University, Canada
[h]Department of Physics, Ewha Womans University, Korea
[i]RIKEN (The Institute of Physical and Chemical Research)

Type I X-ray bursts are the most frequently observed thermonuclear explosions in nature [1, 2]. They take place on the surface of accreting neutron star in low-mass X-ray binary systems [3]. The investigation of X-ray bursts can help us to understand the neutron star's properties and the underlying physics [4].

The bursts are driven by the tripe-α reaction, the αp-process [5] and the rp-process [6]. After breakout from the hot CNO cycle, the nucleosynthesis path is characterized by the αp-process. The αp-process is a sequence of α- and proton-induced reactions that transport nuclear material from the CNO cylce toward heavier proton-rich nuclei region.

The X-ray light curve is the main direct observable of X-ray bursts, which may be affected significantly by the αp-process [7]. According to a recent sensitivity study by Cyburt [7], the ^{22}Mg(α, p)^{25}Al reaction is thought to be the most sensitive one during the αp-process and may have a prominent impact on the burst light curve. However, with a few experimental information on this reaction, the reaction rates were calculated using the statistical models.

An elastic scatering measurement of ^{25}Al+p has been performed to experimentally examine the ^{22}Mg(α, p)^{25}Al reaction rates. The experiment was carried out using the CNS radioactive ion beam separator (CRIB) [8], installed by the Center for Nuclear Study (CNS), University of Tokyo, in the RIKEN Accelerator Research Facility. A primary beam of ^{24}Mg^{8+} was accelerated up to 8.0 MeV/u by the AVF cyclotron (K = 70) with an average intensity of 1 eμA. The primary beam bombarded a liquid-nitrogen-cooled D_2 gas target where a secondary beam of ^{25}Al was produced via the ^{24}Mg(d, n)^{25}Al reaction in inverse kinematics. The D_2 gas at 200 Torr and 90 K was confined in a small cell with a length of 80 mm. The enterance and exit windows were made of 2.5 μm thick Havar foils. The ^{25}Al beam was separated by the CRIB separator using the in-flight method. The ^{25}Al beam, with an average energy of 142 MeV and an average intensity of 2.0×10^5 pps, was then delivered to F3 experimental chamber and bombarded a thick $(CH_2)_n$ target in which the beam was stopped.

The setup at F3 experimental chamber is shown in Figs. 1. A PPAC (Parallel Plate Avalanche Counter) and a

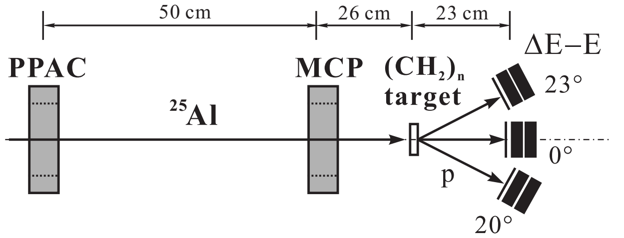

Figure 1. Schematic diagram (top view) of the experimental setup at F3 chamber.

MCP (Micron Channel Plate) were used for measuring time and position information of the beam particles. The beam particles were identified in an event-by-event mode using the abscissa of MCP, and the ToF between MCP and the RF signal provided by the cyclotron. After passing through a Wien-Filter, the ^{25}Al beam purity can be up to 80%. Figs. 2 shows the particle identification before the secondary target.

The recoiling light particles were measured using three sets of Si telescopes at average angles of $\theta_{lab} \approx 0°$, 20° and 23°, respectively. Each telescope consisted of a 65-μm-thick double-side-strip (16×16 strips) silicon detector and two 1500-μm-thick pad detectors. The recoiling particles were clearly identified by using the ΔE-E method. An array of ten NaI detectors was mounted directly above the target and used to detect the γ rays from the decay of the excited states in ^{25}Al. In addition, a carbon target was used in a separate run for evaluating the background contribution.

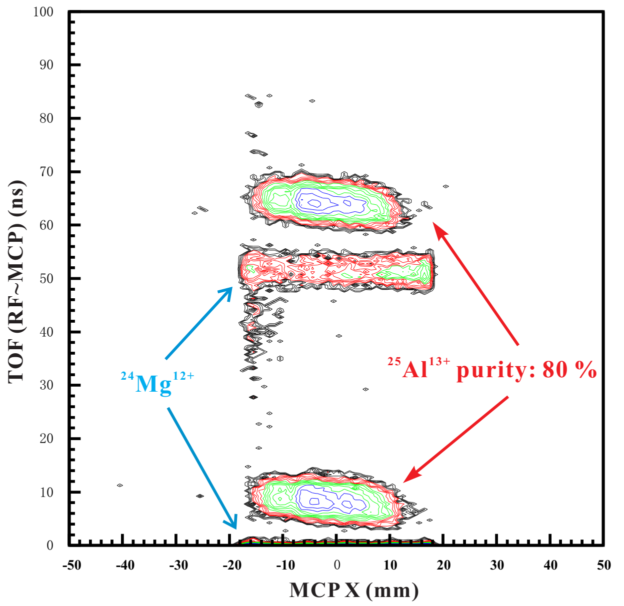

Figure 2. Identification plot for the beam particles before the secondary target.

Figs. 3 shows the proton spectrum at $\theta_{lab} \approx 0°$ for ^{25}Al+p elastic scattering in the center-of-mass frame. Resonances

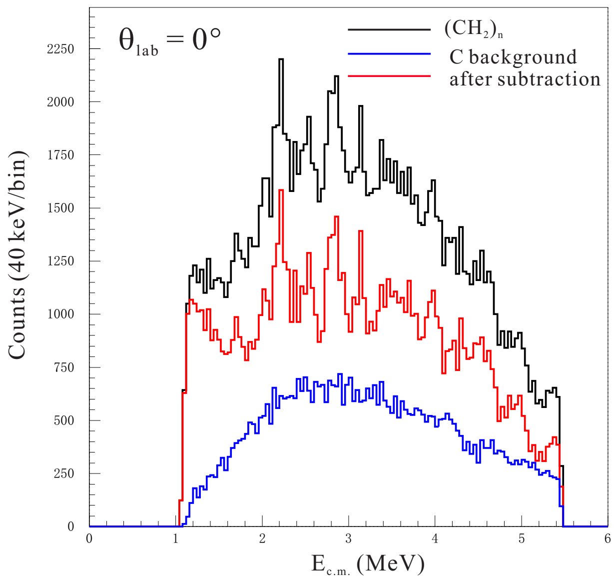

Figure 3. Energy spectrum of proton for ^{25}Al+p elastic scattering after conversion to the center-of-mass frame at $\theta_{lab} \approx 0°$.

with several structures were clearly observed, see Figs. 4. 13 resonance structures are indicated with arrows. The positions of the peaks are essentially in good agreement with previous measurements [9]. In order to determine the resonant parameters of observed resonances, a comprehensive multichannel R-matrix [10] analysis is on going.

References

[1] W.H.G. Lewin, J.V. Paradijs and R.E. Taam, Space Science Reviews **62** (1993) 223.
[2] H. Schatz, and K.E. Rehm, Nucl. Phys. A **777** (2006) 601.

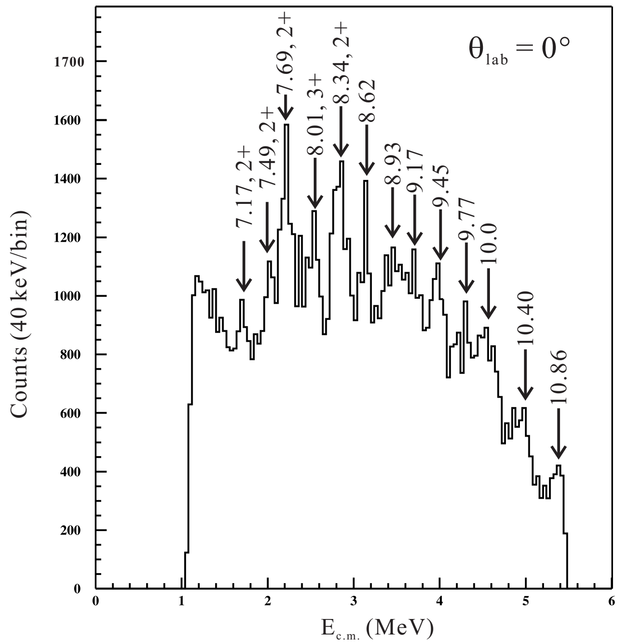

Figure 4. Proton spectrum in center-of-mass frame after C background subtraction. Arrows indicate the prominent resonances.

[3] P.C. Joss, Nature **270** (1977) 310.
[4] A.W. Steiner, J.M. Lattimer and E.F. Brown, Astrophys. J. **722** (2010) 33.
[5] R.K. Wallace and S.E. Woosley, Astrophys. J. Suppl. **45** (1981) 389.
[6] M. Wiescher *et al.*, Astrophys. J. **316** (1987) 162.
[7] R.H. Cyburt *et al.*, Astrophys. J. **830** (2016) 55.
[8] Y.Yanagisawa *et al.*, Nucl. Instr. Meth. **539** (2005) 74.
[9] ENSDF [http://www.nndc.bnl.gov/ensdf/].
[10] A.M. Lane and R.G. Thomas, Rev. Mod. Phys. **30** (1958) 257.

^{7}Be target production to measure ^{7}Be(d, p) reaction for the primordial ^{7}Li problem in Big-Bang Nucleosynthesis

A. Inoue, A. Tamii, S. Cha[a], K. Y. Chae[a], S. Hayakawa[b], N. Kobayashi, S. Nakamura, T. Shima, H. Shimizu[b], H. Yamaguchi[b] and Z. Yang[b]

Research Center for Nuclear Physics, Osaka University
[a]*Department of Physics, Sungkyunkwan University, Suwon, Republic of Korea*
[b]*Center for Nuclear Study, Graduate School of Science, University of Tokyo*

The overestimation of primordial ^{7}Li abundance in the standard Big-Bang nucleosynthesis (BBN) model is one of the known and unresolved problems. A recent theoretical BBN model predicted a primordial ^{7}Li abundance that was approximately three times larger than the recent precise observation [1]. Light nuclei were produced up to ^{7}Be by nuclear reactions in several hundred seconds following the Big Bang.

^{7}Li nuclei were predominantly produced by the electron capture decay of ^{7}Be in the standard BBN model. The decay half life of ^{7}Be, 53.22 days, is much longer than the timescale of the production of light nuclei after the Big Bang. Thus, one possible scenario to solve the ^{7}Li problem is that ^{7}Be was destroyed in the timescale of the nuclear reactions. There are several possibilities to destroy ^{7}Be, for example, the ^{7}Be$(d,p)^8$Be, ^{7}Be(n, α), or ^{7}Be(n, p) reactions [2]. We focus on the ^{7}Be$(d, p)^8$Be reaction because its contribution is suggested to be larger than that of ^{7}Be$(n, \alpha)^4$He [3] [4]. The goal of the experiment is to measure the cross-section of the ^{7}Be$(d, p)^8$Be reaction in the BBN energy region of 100 - 400 keV. We plan to measure the ^{7}Be$(d, p)^8$Be reaction with a ^{7}Be target because the available data are insufficient for the accuracy and energy range [5] [6]. We are also motivated to measure the reaction in direct kinematics because it results in a good energy resolution. The method allows us to reconstruct the kinematics of the reaction by measuring the outgoing proton without measuring the two alpha particles. We apply the *implantation target method* to produce the ^{7}Be target. ^{7}Be particles were implanted by irradiating a gold target with a ^{7}Be beam.

We performed an experiment to produce a ^{7}Be implanted target at CRIB, Center for Nuclear Study (CNS) in April, 2018 [7]. The experimental setup is shown in Fig. 1. The primary beam was ^{7}Li^{2+} at 5.6 MeV/nucleon. The secondary beam was produced by the ^{1}H(^{7}Li, ^{7}Be) reaction. The secondary beam energy was 4.0 MeV/nucleon. The ^{7}Be beam was directed onto a 10 μm thick gold target as the host material after an energy degrader made of gold with a thickness of 15 μm and 2 mmϕ collimator determined the implanted beam position.

We determined the amount of implanted ^{7}Be by detecting 477 keV γ-rays with a LaBr$_3$ detector after the implantation. The γ-ray is emitted in the electron capture process of ^{7}Be with a branching ratio of 10.5%. We achieved an implantation of 1.9×10^{12} ^{7}Be particles as expected after one day of irradiation. Figure 2 shows the measured γ-ray spectrum. We improved the beam optics for the high intensity ^{7}Be beam since 2017, which enabled the production of the ^{7}Be target with a high intensity beam.

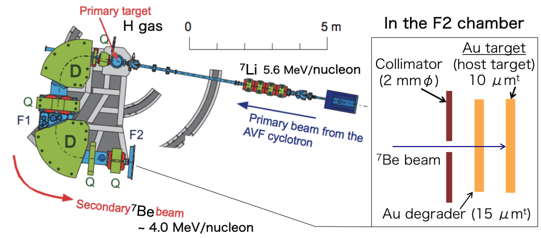

Figure 1. Experimental setup at CRIB. The enlarged schematic picture shows the inside of the F2 chamber.

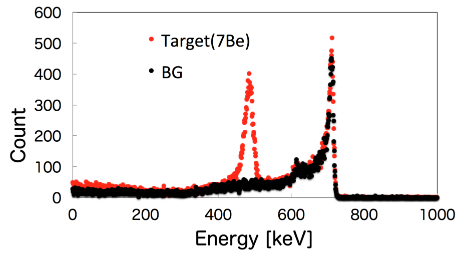

Figure 2. γ-ray energy spectrum of the implanted ^{7}Be (red plots) and background spectrum (black plots).

The ^{7}Be target was carried to the Japan Atomic Energy Agency (JAEA) to measure the (d, p) reaction in June, 2018. The outgoing protons were successfully measured by three layered silicon detectors with the thickness of 500 μm each at two different angles, 30° and 45°. Currently, analyses are being conducted to obtain the cross-section of the ^{7}Be(d, p) reaction.

References

[1] R. H. Cyburt *et al.*, J. Cosmol. Astropart. Phys. **11**, 012 (2008).
[2] M. Barbagallo *et al.*, Phys. Rev. Lett. **117**, 152701 (2016)
[3] S. Q. Hou *et al.*, Phys. Rev. C **91**, 055802 (2015)
[4] T. Kawabata *et al.*, Phys. Rev. Lett. **118**, 052701 (2017)
[5] R. W. Kavanagh *et al.*, Nucl. Phys. **18**, 493 (1960)
[6] C. Angulo *et al.*, Astrophys. J. **630**, L 105 (2005)
[7] H. Yamaguchi *et al.*, Nucl. Instr. Meth. A **589**, 150 (2008)

Study of spin-isospin response of ^{11}Li and ^{14}Be drip line nuclei with PANDORA

L. Stuhl, K. Yako, M. Sasano[a], J. Gao[a,b], Y. Hirai[c], for the SAMURAI30 collaboration

Center for Nuclear Study, Graduate School of Science, University of Tokyo
[a] RIKEN (The Institute of Physical and Chemical Research), Japan
[b] School of Physics, Peking University, Beijing 100871, China
[c] Department of Physics, Kyushu University, Japan

The spin-isospin responses of ^{11}Li and ^{14}Be neutron drip line nuclei were measured in charge-exchange (p,n) reactions. Until recently, only the spin-isospin collectivity in stable isotopes was investigated [1]. There is no available data for nuclei with large isospin asymmetry factors, where $(N-Z)/A > 0.25$. The (p,n) reactions at intermediate beam energies ($E/A > 100$ MeV) and small scattering angles can excite Gamow-Teller (GT) states up to high excitation energies in the final nucleus, without Q-value limitation [2–4]. The combined setup of PANDORA neutron detector [5] and SAMURAI spectrometer [6] with a thick liquid hydrogen target (LHT) allowed us to perform the experiment with high luminosity. In this setup [7], PANDORA was used for the detection of the low-energy recoil neutrons while SAMURAI was used to tag the decay channel of the reaction residues.

A secondary cocktail beam of unstable ^{11}Li and ^{14}Be was produced via the fragmentation reaction of a 230 MeV/u ^{18}O primary beam on a 14-mm-thick ^{9}Be target. Figure 1 shows the overview of the experimental setup. In the experimental setup around SAMRAI spectrometer, two 1-mm-thick plastic scintillators (SBT1,2) were installed for the detection of beam particles.

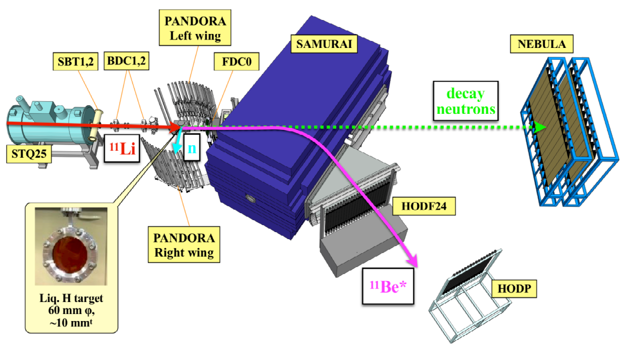

Figure 1. The schematic view of the experimental setup around the SAMURAI spectrometer.

The SBTs were used to produce the beam trigger (threshold was set to $Z > 2$). The beam PID was performed on an event-by-event basis by measuring the energy loss in SBTs and the ToF of the beam particles in BigRIPS between F7 and F13. The secondary cocktail beam consisted of ^{11}Li at 182 MeV/u with intensity of 2.5×10^5 particle/s and ^{14}Be at 198 MeV/u with intensity of 1×10^5 particle/s with purity of 48% and 19%, respectively. The triton contamination was below 30%. The neutron detector setup on the left and right sides of LHT consisted of 27 PANDORA and 13 WINDS [8] plastic scintillator bars. The neutron kinetic energies were deduced by the time-of-flight (ToF) technique. PANDORA was optimized to detect neutrons with a kinetic energy of 0.1–5 MeV by measuring the related ToF in the range of 50 – 300 ns on 1.25 m flight path. The ToF time reference was taken from SBTs. The left and right wings with respect to the beam line covered the laboratory recoil angular region of 47°–113° and 62°–134°, respectively, with 3.25° steps. The light output threshold was set to be 60 keV$_{ee}$.

The reaction residues entered into SAMURAI after passing through the forward drift chamber, FDC0. The magnetic field of the spectrometer was set to 2.75 T. At the focal plane of SAMURAI, a wall (HODF24 detector) of 24 plastic scintillator bars with dimensions of $1200^W \times 100^H \times 10^D$ mm^3 was installed, to measure the trajectories, energy loss, and ToF (from SBTs) of the reaction residues. Further downstream, an additional wall, HODP, with 16 plastic bars (same as HODF24 bars) was installed. Those 2 bars of HODF24 which were hit by the unreacted beam were excluded from trigger. Figure 2 shows a typical PID spectrum detected in HODF24 for events generated by the ^{11}Li or ^{14}Be beams. The reaction products and decay particles can be clearly identified. NEBULA was used to detect the fast decay neutrons of the reaction products (decays by 1n and 2n emissions).

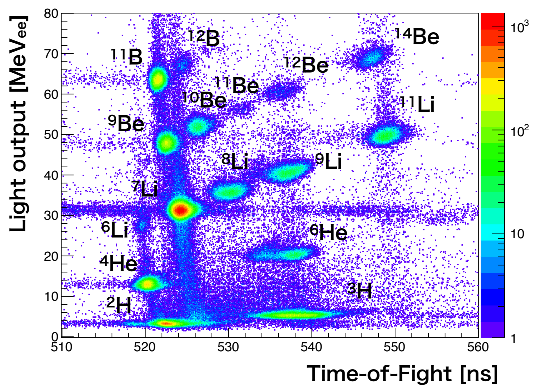

Figure 2. A PID spectrum in the focal plane of SAMURAI spectrometer, measured by one bar (bar ID=7) of HODF24.

The digital data-acquisition (DAQ) of PANDORA [9]was combined with standard DAQ of SAMURAI. Data from PANDORA bars (each with a signal from both ends) were read out with duplicated readout; CAEN V1730 modules were used for charge and pulse shape discrimination information while an analog circuit (discriminators and CAEN V1290 TDC modules) was used for timing and triggering.

For the digital DAQ we daisy chained six CAEN V1730B and one CAEN V1730D waveform digitizers using an optical connection. The unpublished software of digiTES, based on Digital Pulse Processing for the Pulse Shape Discrimination (DPP-PSD) firmware [10] was used to manage different modules in the daisy chain condition and control the digitizers. A LUPO (Logic Unit for Programmable Operation) module [11] was used to generate a 62.5 MHz signal to synchronize timestamps of the seven modules, as well as to share clock with an other LUPO in the DAQ system. The acquisition in the digitizers was not based on the self-triggering of each channel. The local triggering option of the two-two coupled channels, in V1730 two neighboring channels are paired, was used to ensure the coincidence between the top and bottom photomultiplier of PANDORA. The digitizers were configured so that the validation of the local triggers came from an external trigger based on the costumer configured software criteria. In order to manage the coincidence requirements between the two separate acquisition systems, the first channel (ch 0) of each digitizer was dedicated to a logic signal. This external trigger was validating the PANDORA self-triggers in an about 1-μs-wide time window.

The neutron-gamma discrimination of PANDORA is based on comparison of integrated charges measured over two different time regions of the input signal. The PSD parameter is defined as

$$\mathrm{PSD} = \frac{Q_{Long} - Q_{Short}}{Q_{Long}}, \tag{1}$$

where Q_{Long} and Q_{Short} are the charges integrated in long (width = 450 ns) and short (width = 42 ns) gates, respectively. The arithmetic mean of PSD values of two single-end readouts of each PANDORA bar (PSD_{bottom} and PSD_{top}) was defined as, PSD_{mean} [5], an additional parameter to the ToF for each event. The combination of the measured neutron ToF with the new PSD parameter improved the discrimination of neutron- and gamma-like events Figure 3 shows the two-dimensional plot of PSD_{mean} vs. total light output of a PANDORA bar for events associated with ^{11}Li beam. Clear separation of neutron-like events even at the low-light output region is observed.

Figure 4 shows the plot of kinetic energy as a function of laboratory scattering angle for recoil neutrons associated with the ^{11}Li beam. We required the simultaneous detection of ^{9}Li and d in HODF24 and neutron detection in PANDORA (offline PSD cut was applied). A clear kinematical correlation between the measured kinetic energy and the laboratory scattering angle, above 18 MeV excitation energy, was obtained. This forward scattering peak (2°-7° in the center-of-mass system) suggests a GT transition. The $^{9}Li + d$ decay channel of ^{11}Be is observed for the first time. Reconstruction of the excitation-energy spectrum up to about 30 MeV, including the GT giant resonance region, is ongoing.

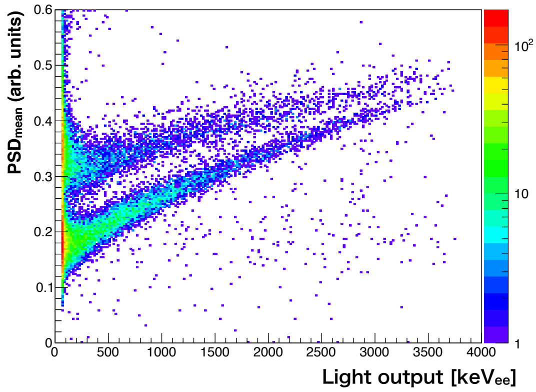

Figure 3. PSD_{mean} as a function of total light output (bar ID=7). Signals from neutrons are located in the upper distribution of the graph, whereas signals from gamma rays are in the lower band.

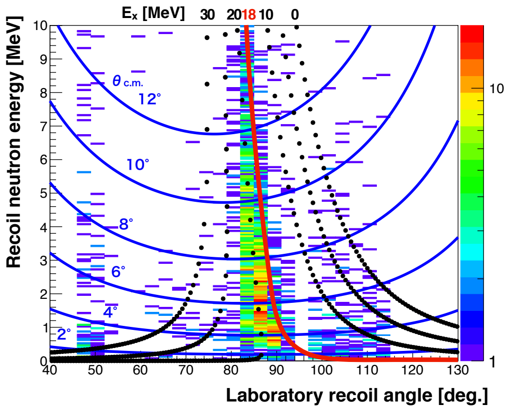

Figure 4. Recoil neutron energy spectrum as a function of scattering angle in the laboratory frame.

References

[1] K. Nakayama, et al., Phys. Lett. B 114 (1982) 217.
[2] M. Sasano, et al., Phys. Rev. Lett. 107 (2011) 202501.
[3] M. Sasano, et al., Phys. Rev. C 86 (2012) 034324.
[4] J. Yasuda, et al., Phys. Rev. Lett. 121 (2018) 132501.
[5] L. Stuhl, et al., Nucl. Instrum. Meth. A 866 (2017) 164.
[6] T. Kobayashi et al., Nucl. Ins. Meth. B 317 (2013) 294.
[7] L. Stuhl, et al., Nucl. Instrum. Meth. A https://doi.org/10.1016/j.nimb.2019.05.057
[8] K. Yako, et al., RIKEN Accel. Prog. R. 45 (2012) 137.
[9] L. Stuhl, et al., Proceedings of Sci. (INPC2016) 085.
[10] http://www.caen.it/csite/CaenProd.jsp
[11] https://ribf.riken.jp/RIBFDAQ/index.php?DAQ

Proton/deuteron-induced reactions of ^{93}Zr using the slow RI beam

J.W. Hwang, K. Iribe[a], M. Dozono, N. Imai, S. Michimasa, T. Sumikama[b], N. Chiga[b], S. Ota, O. Beliuskina, S. Hayakawa, C. Iwamoto, S. Kawase[c], K. Kawata, N. Kitamura, S. Masuoka, K. Nakano [c], P. Schrock, D. Suzuki[b], R. Tsunoda, K. Wimmer[d], D. S. Ahn[b], N. Fukuda[b], E. Ideguchi[e], K. Kusaka[b], H. Miki[f], H. Miyatake[g], D. Nagae[b], M. Nakano[h], S. Ohmika[b], M. Ohtake[b], H. Otsu[b], H. J. Ong[e], S. Sato[h], H. Shimizu, Y. Shimizu[b], H. Sakurai[b], X. Sun[b], H. Suzuki[b], M. Takaki, H. Takeda[b], S. Takeuchi[f], T. Teranishi[a], H. Wang[b], Y. Watanabe[c], Y. X. Watanabe[g], H. Yamada[f], H. Yamaguchi, R. Yanagihara[e], L. Yang, Y. Yanagisawa[b], K. Yoshida[b], and S. Shimoura

Center for Nuclear Study, Graduate School of Science, University of Tokyo
[a]*Department of Physics, Kyushu University*
[b]*RIKEN Nishina Center for Accelerator-Based Science*
[c]*Department of Advanced Energy Engineering Science, Kyushu University*
[d]*Department of Physics, the University of Tokyo*
[e]*Research Center for Nuclear Physics, Osaka University*
[f]*Department of Physics, Tokyo Institute of Technology*
[g]*WNSC, IPNS, KEK*
[h]*Department of Physics, Rikkyo University*

Reprocessing of radioactive waste generated by nuclear reactors has been one of the long-standing issues in the use of nuclear energy. In 2013, the amount of spent fuel discharged from nuclear power plants reached about 360,000 tons worldwide, and is still increasing by about 12,000 tons every year [1]. Nuclear transmutation is one of the solutions to reduce such high-level waste (HLW). Several ways of nuclear transmutation such as accelerator-driven system and fast reactors were proposed, and a great deal of effort has been devoted to put them to practical use [2].

^{93}Zr is one of the long-lived fission products (LLFPs), which are the most intractable components in HLW. It accounts for 6% of production yield in thermal neutron fission of ^{235}U and has an enormously long half-life of 1.53×10^6 years. The ImPACT program has been proposed to establish the procedures of nuclear transmutation to reprocess LLFPs. The previous studies on ^{93}Zr and ^{107}Pd reported that proton/deuteron-induced reactions at 100 – 200 MeV/u are effective for the nuclear transmutation [3–6]. Even at lower energies (10 – 50 MeV/u), those reactions would be more considerable due to larger cross sections to be expected, which has not been experimentally investigated yet. This research, as a part of the ImPACT program, aims to measure the cross sections of the products of the proton/deuteron-induced reactions of ^{93}Zr at the low energy, 30 MeV/u, in inverse kinematics. Note that this report is the subsequent one by K. Iribe *et al.* [7].

The experiment was carried out at the RIBF at RIKEN, using the BigRIPS [8] and OEDO beamline [9] as presented in Fig. 1. A ^{238}U primary beam at 345 MeV/u impinged on a 5-mm-thick ^{9}Be primary target at F0, the entrance of the BigRIPS. Then, ^{93}Zr produced by the in-flight fission was seperated from other isotopes with the proper ion optics including the Al wedge degrader at the focal plane F1.

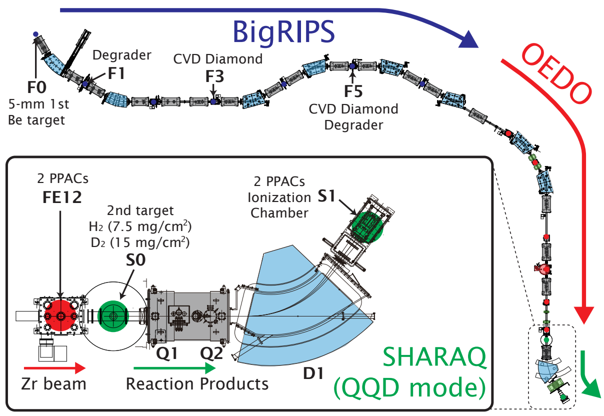

Figure 1. BigRIPS and OEDO beamlines together with the experimental setup in the inset.

The time-of-flight (TOF) between the focal plane F3 and F5 measured with the CVD diamond detectors [10] provided us the clear identification of the ^{93}Zr beam, with the mass-to-charge ratio (A/Q) resolution of 1.9×10^{-3}. The purity of ^{93}Zr in the secondary beam contaminated by neighboring nuclei such as ^{92}Y and ^{94}Nb was 35.9%. The beam was slowed down in the another Al degrader at F5 and well focused at the reaction point S0, thanks to the OEDO beamline, employing a radio-frequency deflector and two superconducting triplet quadrupole magnets. To obtain the properties of the beam event-by-event, we used parallel-plate avalanche counters (PPACs) at FE12 [11]. The average energy of the ^{93}Zr beam at S0 was 32 MeV/u from the TOF between F5 (Diamond) and FE12, and the horizontal and vertical widths were 50.5 and 14.3 mm in FWHM, respectively. The typical beam intensity was 1.5×10^3 pps.

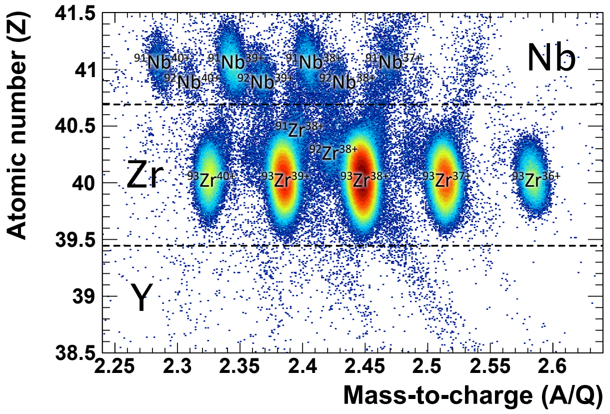

Figure 2. Preliminary identification of reaction products with A/Q and Z in the case of the H_2 target. The data from all $B\rho$ settings are accumulated.

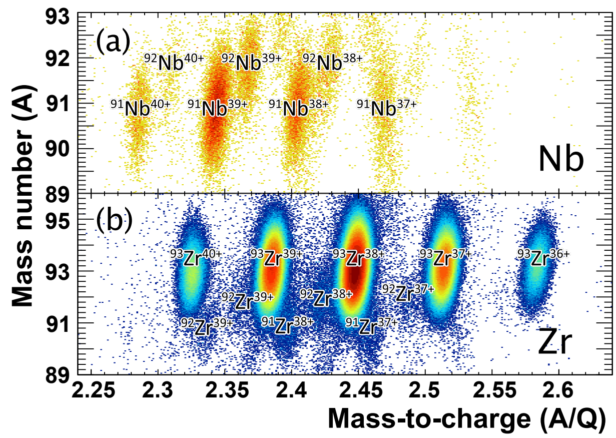

Figure 3. Preliminary identification of reaction products with A/Q and A in the case of the H_2 target for (a) Nb and (b) Zr isotopes. The data from all $B\rho$ settings are accumulated.

As shown in the inset in Fig. 1, we installed the H_2 and D_2 gas targets at 40 K and 2.2 atm at S0, with the thickness of 7.5 and 15 mg/cm^2, respectively. The SHARAQ spectrometer was used to identify the reaction products and to determine their momenta in the QQD configuration, the first half with two quadrupole and one dipole magnets [12, 13]. The momentum acceptance is $\pm 3\%$ and the angular acceptance is ± 30 mrad for both horizontal and vertical directions. Two PPACs and an ionization chamber (IC) [14] at the focal plane S1 detected ions passing through the spectrometer. A/Q was reconstructed by the magnetic rigidity ($B\rho$) and TOF from the position and timing measured by the PPACs at S0 and S1. Atomic number (Z) and mass (A) were determined using the information from the IC by the Bragg curve fitting. Five different $B\rho$ settings were applied to cover a wide momentum range of reaction products.

The analysis of the experimental data is in progress, which includes the particle identification of reaction products and their reaction cross sections. Figure 2 shows the preliminary result of the identification using A/Q and Z with the H_2 target. The clear separation of Z was achieved into Nb ($Z = 41$) and Zr ($Z = 40$) with the resolution $\sigma_Z/Z = 4.3 \times 10^{-3}$. There is no evidence of existence of Y ($Z = 39$) with the sensitivity of our measurement. Several charge states were also well identified, in particular, in the case of ^{93}Zr, the beam nucleus, and ^{91}Nb, the most abundant product estimated by TENDL [15]. The resolution of A/Q is $\sigma_{A/Q}/(A/Q) = 2.6 \times 10^{-3}$. More precise identification with A for each element is described in Fig. 3. For Nb isotopes, the different masses and charge states are well separated. The preliminary reaction cross section for ^{91}Nb was 778 ± 21(stat.) mb, which is consistent to the result of TENDL, 674 mb, within the order of magnitude. However, the Zr isotopes lighter than the ^{93}Zr beam are not distinguished well because of the dominant intensity of the beam and relatively low resolution of A/Q. In the follow-up analysis, we will concentrate on the unambiguous identification of Zr isotopes and the extraction of their cross sections.

This work was funded by the ImPACT Program of the Council for Science, Technology and Innovation (Cabinet Office, Government of Japan).

References

[1] INTERNATIONAL ATOMIC ENERGY AGENCY, Status and Trends in Spent Fuel and Radioactive Waste Management, Nuclear Energy Series No. NW-T-1.14, IAEA, Vienna (2018).
[2] OECD Nuclear Energy Agency, OECD/NEA Report No. 3109 (2002).
[3] H. Wang *et al.*, Phys. Lett. **B754** (2016) 104.
[4] H. Wang *et al.*, Prog. Theor. Exp. Phys. **2017** (2017) 021D01.
[5] H. Wang *et al.*, Comm. Phys. **2** (2019) 78.
[6] S. Kawase *et al.*, Prog. Theor. Exp. Phys. **2017** (2017) 093D03.
[7] K. Iribe *el al.*, CNS Annual Report 2017, CNS-REP-**97** (2019) 5-6.
[8] T. Kubo, Nucl. Instrum. Methods Phys. Res. Sect. B **204** (2003) 97.
[9] S. Michimasa *et al.*, Prog. Theor. Exp. Phys. **2019** (2019) 043D01.
[10] S. Michimasa *et al.*, Nucl. Instrum. Methods Phys. Res. Sect. B **317** (2013) 710.
[11] H. Kumagai *et al.*, Nucl. Instrum. Methods Phys. Res. Sect. B **317** (2013) 717.
[12] T. Uesaka *et al.*, Prog. Theor. Exp. Phys. **2012** (2012) 03C007.
[13] M. Dozono *et al.*, Nucl. Instrum. Methods Phys. Res. A **830** (2016) 233.
[14] N. Chiga *et al.*, RIKEN Accel. Prog. Rep. **50** (2017) 164.
[15] A.J. Koning *et al.*, Nuclear Data Sheets 155 (2019) 1.

Simulation studies of the performance of THGEMs

N. T. Zhang[a,b], S. Ota[a], R. Kojima[a], C. Iwamoto[a], and H. Tokieda[a]

[a] Center for Nuclear Study, Graduate School of Science, University of Tokyo
[b] Institute of Modern Physics, Chinese Academy of Sciences, Lanzhou, China

A GEM-based TPC detector (time projection chambers), called CNS Active Target (CAT), has been developed at CNS [1]. To avoid the charge build-up of field cage with very intense beams, a segmented multi-layer thick gas electron multiplier (DG-M-THGEM) has been designed at CNS to realize different gains in the beam region and recoil region. The DG-M-THGEM has four electrode layers, which are insulated by three FR4 foils. Total thickness of DG-M-THGEM is 1.2 mm and the hole size and pitch are 300 μm and 700 μm, respectively. Fig. 1 shows a sketch of CAT detector and GEM cell. The performance evaluation of the prototype of DG-M-THGEM will be presented in our other work [2].

The main software tool used for the simulation of gas detectors is Garfield++, a powerful toolkit for the detailed simulation of physically electron transport in the gas medium [3]. One of main limitations of Garfield++ is that its built-in MAXWELL softpackage could only simulate two-dimensional fields [4]. In this work, the open-source field solver Elmer, a finite elements electrostatics software, was used to calculate the three-dimensional electric fields, while Gmsh was used as mesh generator for Elmer [5, 6]. A 3d geometrical GEM model built by Gmsh is shown in Fig. 1. The entire GEM foil was produced by replicating periodically this elementary "cell". The electron transport and avalanches in the gas were done by Magboltz, where the electrons drift velocity and the longitudinal and transverse diffusion have been automatically considered in the Garfield++ calculation.

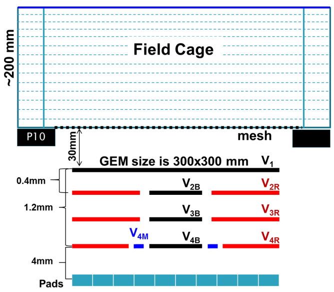

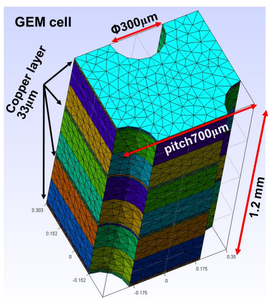

Figure 1. Schematic representation of CAT structure (left) and GEM cell used in the simulation (right).

The effective gain was measured as the ratio of the electron charges collected at the anode to the ionized primary charges in the drift region. In the Garfield++, the gain is calculated for each primary electron and the comparison with the measurements is shown in Fig. 2. The agreement indicated in Fig. 2 shows that the simulation has a good predictive power on the gain tendency. At the last data point with the reduced field of 322.4 V/cm/kPa, the gain by simulation is 20% higher than the measured value. A possible reason is the insulator charging-up, which is not included in this work. The charging-up effect always induces the gain variation in the order of a few tens of percent.

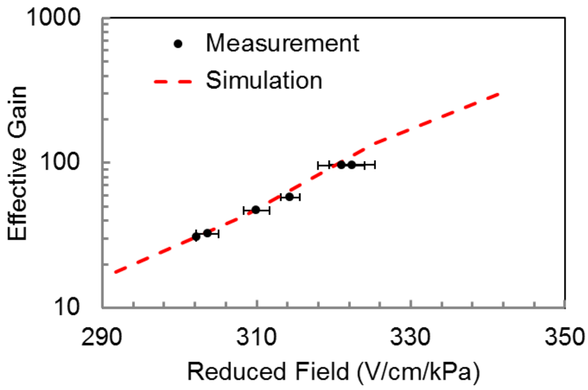

Figure 2. Comparison of effective gain between the simulation result and experimental measurement. The field ratio applied in the three GEM layers is 1:1:1. The reduced field is the field inside the GEM holes.

In the avalanching process in the GEM detectors, the generated avalanche ions back-flowing to the drift volume can drastically influence the detector operation and lifetime [7]. The reduction of ion backflow (IBF) is very important for the good performance of TPC with high incident beam intensity, where the beam ions induce serious feedback effects in the GEM avalanches. To achieve a better understanding of IBF and search for an efficient IBF suppression, we also performed detailed simulation of the transportation of electrons/ions in the GEM holes. Fig. 3 gives the IBF dependence on the drift field between the grid mesh and GEM foil. One can see that decreasing the drift field can provide a good electron transmission. This result is reasonable since IBF is proportional to the ratio between the drift and the avalanche fields. In the test experiment performed at Heavy Ion Medical Accelerator in Chiba (HIMAC) in 2018, the electric field in the beam region was 1.5 kV/cm/atm, corresponding to a calculated IBF ratio of 84%. If this IBF value is true, the positive ions will induce serious space charge and worsen the spatial position resolution. We also did the IBF measurements in a testing chamber and the current ratio between the cathode and anode was 55%, comparable to our simulation. In the same time, we carried out the IBF simulations with different GEM configurations and found the two DG-M-THGEMs could significantly suppress the ion back-flow, in which the top GEM foil acts as a stopper by collecting the back-flowing ions. Note that the electron/ion transparency passing through the grid mesh was not considered in the simulation, but these results could guide us in the configuration setups seeking the IBF suppression. A paper on the simulation of the trajectory distortion by IBF is currently being prepared.

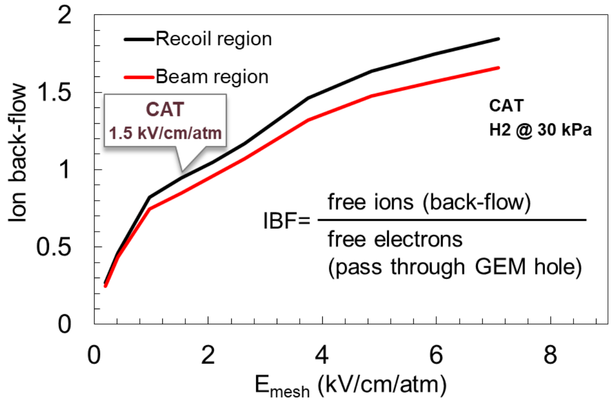

Figure 3. The dependence of ion back-flow on the drift field. E_{mesh} is the field in the drift region between the grid mesh and GEM foil.

In the experiments using TPC as an active target, the detector is often required to work with intense heavy-ion beams. The generated ion feedbacks will induce severe limits on the TPC operation and attainable amplification gain. Our calculations were able to simulate the detector response quickly and provided values for the gain, electron distributions and ion back-flow. This is very helpful to optimize the TPC configurations. Further simulation work is to be performed for extensively calculations on different GEM setups. In order to make a direct IBF comparison with the measurements, a very fine mesh structure must be included in the TPC models.

References

[1] S. Ota et al., J. of Radioanal. Nucl. Chem. 305, 907 (2015).

[2] C. Iwamoto et al., to be published in CNS Annual Report 2018.

[3] R. Veenhof, Garfield — simulation of gaseous detectors, 1984 - 2010. http://garfield.web.cern.ch.

[4] S. Biagi, Magboltz—A programto solve the Boltzmann transport equations for electrons in gas mixtures, 2000. http://consult.cern.ch/writeup/magboltz

[5] Elmer, https://www.csc.fi/web/elmer/elmer.

[6] C. Geuzaine and J. Remacle, Gmsh. http://gmsh.info/

[7] D. Attie, Nucl. Instrum. Meth. A 598, 89 (2009).

Production of isomer around ^{52}Fe nucleus via projectile fragmentation

Keita Kawata [a,b], Shinsuke Ota [a], Masanori Dozono [a], Juzo Zenihiro [b], Chihiro Iwamoto [a], Noritaka Kitamura[a], Hideyuki Sakai[b], Shoichiro Masuoka[a,b], Shin'ichiro Michimasa[a], Kentaro Yako[a], Tomoya Harada[b,c], Hiroki Nishibata[b], Rieko Tsunoda[a], Nobuyuki Imai[a], Tomoya Sato[b], Jongwon Hwang[a], Ningtao.Zhang[d], Fumitaka Endo [e]

[a]*Center for Nuclear Study,University of Tokyo* [b]*Riken Nishina Center,* [c]*Toho Universicity* [d]*Institute of Modern Physics* [e]*Tohoku University*

Study of the structure and reaction of nucleus in metastable excited state called isomer is one of the most attractive topics since the smaller overlap of its wave function than the wave function of ground state may provide another probe for two-body interactions within the same nucleus. In particular isomers with high spin state, ^{52}Fe(12+) for instance, are expected to have very pure wave function due to the spin alignment.

To perform the nuclear reactions on such isomers, beams of isomers should be prepared since the isomers are still short-lived nuclei. Typical way to prepare the short-lived nuclei is to use projectile fragmentation. Production mechanism of isomers is so far discussed based on the systematic measurement of production yield by changing the linear momentum transfer (or velocity change) [1] and the mass difference between projectile and fragment (mass loss) [2] [3]. Angular momentum transfer in projectile fragmentation has not been discussed explicitly although the production of high spin isomer may be affected by it. This is because the production of the ground state includes all the possible angular momentum transfers.

On the other hand, the production of isomers is mainly expected to include the angular momentum transfer larger than the spin state of isomer. In this study, we aim to make a comprehensive understanding of the production of isomers via projectile fragmentation including the role of angular momentum transfer in the projectile fragmentation by measuring the production of isomers from different initial spin state as a functions of linear momentum transfer and from different mass region nucleus.

In our previous study, we already measured the production of isomers from large mass loss using the primary beam of ^{82}Kr. In this paper, we report a new systematic measurement of production cross sections of isomers ^{52}Fe(12+),^{53}Fe(19/2-), ^{54}Co(7+) and ^{54}Fe(10+) from the primary beams of ^{58}Ni and ^{59}Co, whose spin is 0+ and 7/2-.

The experiment of project number of H362 was performed at SB2 course in HIMAC, the synchrotron facility in Chiba. Figure 1 shows the experimental setup at SB2 course. The primary beams of ^{58}Ni and ^{59}Co at the 350 MeV/u bombarded the production target of 14-mm thick ^{9}Be target. The fragments of ^{52}Fe,^{53}Fe, ^{54}Co, ^{54}Fe and contaminants are separated and momentum analyzed by a fragment separator consisting two dipole magnets and quadrupole magnets. At the first focus on F1, a wedge-shaped aluminum energy degrader of 3.5-mm thickness was

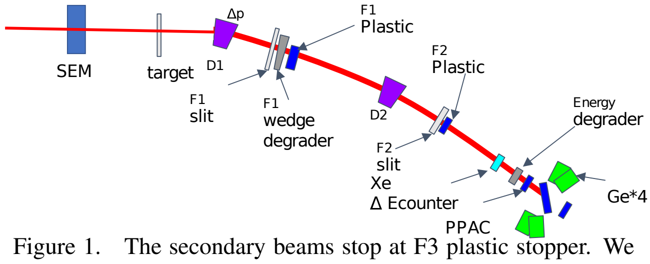

Figure 1. The secondary beams stop at F3 plastic stopper. We identified the fragment by using ToF-ΔE method, ToF was measured from F2 to F3 ,ΔE was measured by Xe scintillator detector. The number of total fragment was counted by Xe and the number of isomer was counted by Ge detector.

located to make a better separation of fragments. A momentum slit was also located to define the linear momentum transfer to the fragments. At the second focus on F2, a plastic scintillator (F2PL) was located. At the last focus F3, a Xe gas scintillator, a parallel plate avalanche counter, an energy degrader, an active stopper of plastic scintillator (Stopper) and four co-axtial germanium detectors were located. The fragments were particle identified by using ToF-ΔE method on an event-by-event basis. The ToF was measured by using the F2PL and the Xe, and the dE was measured by the using Xe. The Stopper was 5-mm thick plastic scintillator tilted by 45 degrees respected to the beam axis.

In order to measure the momentum distribution of the production cross section, the intensity of the primary beam was monitored by using the secondary emission monitor(SEM). The SEM was located in front of the target. The SEM consisted of a thin film of copper and emission charge detector.

Figure 2 shows the signal of the SEM. In the circuit of SEM the raw signal of voltage which is proportional to the charge in sampling rate of a few kHz and this voltage is converted to the frequency for recording. Ch2 is the frequency to which the positive voltage of the signal is proportional. Ch3 is the frequency to which the negative voltage of the signal is proportional. We obtained the intensity from ch2 and ch3.

The signal of the $SEM_{negative}$ shows the undershoot of the raw voltage(ch 1). In the low-intensity beam setting, the number of the primary beam was counted by the Xe. In the high intensity beam settings same intensity as the physics run, the primary beam cannot be counted by the Xe scintillator due to the pile-up. Then, the secondary beam is used as a reference for the calibration. The conversion factor form the number of the secondary beam to the number of primary

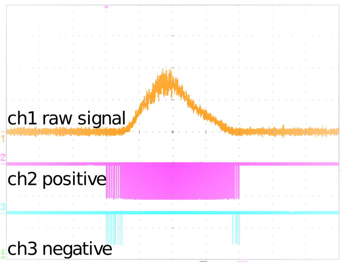

Figure 2. Ch1 is the raw signal of voltage. Ch2 is the frequency to which the positive voltage of the signal is proportional. Ch3 is the frequency to which the negative voltage of the signal is proportional.

beam was measured with the intermediate intensity of 10^5 pps.

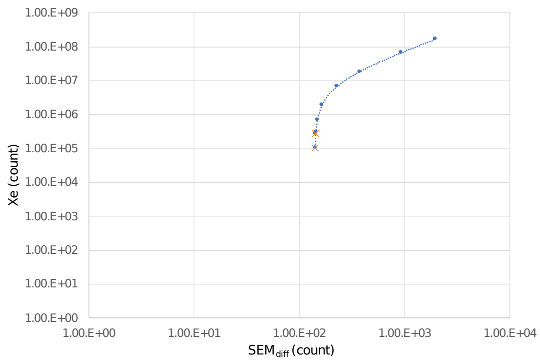

Figure 3. The horizontal axis shows SEM_{diff} which is $SEM_{positive}$-$SEM_{negative}$ and vertical axis shows the number of Xe scintillator counts. Blue circles show the calibration points by secondary beams where red crosses shows the points with the primary beam.

Figure 3 shows the correlation between the SEM signal and the primary beam intensity. The red cross and blue dot points correspond to direct measurement and indirect measurement using secondary beam, respectively. The primary bean intensity during the physics measurement is calculated by using 4-th order polynomial fitted to the measured correlation.

In order to calculate isomer ratio the number of the fragment and γ ray from isomer will be counted. The number of the each nuclei was counted from the Xe scintillator which is projection to the ΔE plot. The number of the γ rays in the certain peak from the isomer was counted from the energy spectrum of the Ge detectors. Isomer ratio is defined as $R = N_{isomer}/N_{ion}$ whose values are calculated with the correction of the each efficiency.

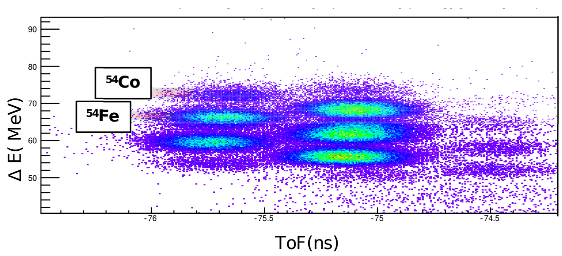

Figure 4. The horizontal axis shows the Time of Flight(ns) and the vertical axis shows ΔE

Figure4 shows the particle identification plot, ToF is calculated from the time difference between F2PL and Xe scintillator and ΔE is calculated from Xe scintillator.

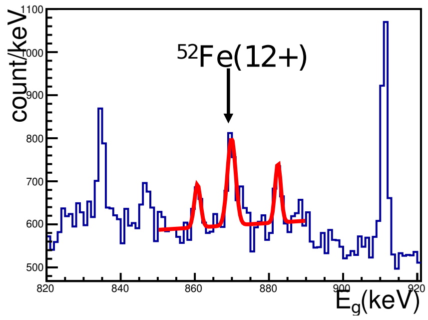

Figure 5. This figure shows the γray energy spectrum which is sum of the 4 Ge detectors.

Figure 5 shows the γ ray energy spectrum which come from ^{52}Fe(12+).The peak at 870 keV is fitted by gaussian function. Reaction was assumed to occur in the center of the target in this analysis.

When the velocity of the fragment is same as the projectile, longitudinal momentum transfer is defined as 0 MeV/c. The velocity before reaction is calculated from the beam energy with the target information and the velocity after reaction is calculated from the value of Bρ in D1.

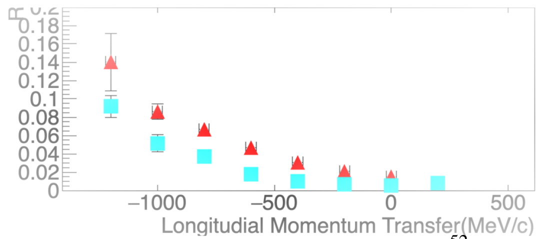

Figure 6. The figure shows the Isomer ratio of ^{52}Fe(12+).Red triangle means the projectile is ^{59}Co(7/2-),and blue square means ^{58}Ni(0+)

In the Figure 6 the preliminary result of isomer ratio of ^{52}Fe(12+) is shown. In the same as the previous study , isomer ratio depends on the momentum transfer. The value of isomer ratio in the setting of ^{59}Co(7/2-) shows larger than the value one in ^{58}Ni(0+). It is inferred that the initial angular momentum of the projectile has a significant effect in isomer production.

In the next study we will discuss about the difference of the momentum distribution between total ion and isomer, and the effective condition for the population of the high spin isomer via projectile fragmentation.

References

[1] M. Notani*et al.*, Phys. Rev. C.**15** ,044605(2007).
[2] A.S. Goldhaber*et al.*, Physics Letters B**53**306 - 308(1974).
[3] M.De Jong*et al*, Nuclear Physics A **613** (1997) 435-444

Present status of fundamental symmetry experimental project with laser cooled heavy elements

Y. Sakemi, H. Nagahama, T. Hayamizu, N. Ozawa,
K.S. Tanaka[a], K. Harada[a], A. Uchiyama[a], J. Tsutsumi[b]

Center for Nuclear Study, Graduate School of Science, The University of Tokyo
[a]Cyclotron and Radioisotope Center, Tohoku University
[b]Department of Physics, College of Science, Rikkyo University

It is thought that there was an equal amount of matter and antimatter at the beginning of the universe, but it has not been understood fully how the antimatter had been disappeared in the history of the universe for more than 13.5 billion years. The understanding of this matter-antimatter symmetry violation (CP violation) has led to the search for new physics beyond the standard model, and is always of interest. Supersymmetry theory (SUSY), which is one of the ideas for solving the hierarchy problem of particle masses, unifying gauge coupling constants, and the candidate of the physical entity of dark matter, predicts the partner particles (SUSY particles) to each quark and lepton flavors. Although the SUSY particles are not observed directly with EDM measurement, its existence can be proved by the precise detection of the quantum correction effect generated through the SUSY particle propagations [1]. The permanent electric dipole moment (EDM) of heavy elements such as Francium (Fr) is one of the candidates to search for the CP violation and SUSY particles [2].

The EDM for Fr atoms will be measured by atomic interferometry using quantum optics techniques such as laser trapping in an optical lattice (OL) to achieve longer interaction times with external fields. Low-energy Fr ions will be produced by nuclear fusion reactions with a surface ionization process, and will be transported to the EDM measurement area. They will be trapped in a magneto-optical trap (MOT) at the first stage. They will then be transferred to an OL equipped with electric field plates. The spin precession of the Fr will be measured using the Ramsey resonance method to extract the EDM. However the slight shift of the magnetic field due to external environment such as the geomagnetism or magnetic field changes generated from beam line magnets and an accelerator causes a false signal of the EDM through the first term in the equation (1).

$$H = -\mu \frac{\mathbf{s}}{|s|} B - d \frac{\mathbf{s}}{|s|} E \qquad (1)$$

Then, the MOT and OL will be installed inside magnetic shielding with an active field cancellation system to suppress the effects of environmental magnetic field fluctuations. The remaining fluctuations of the magnetic field have to be monitored using a magnetometer installed inside an EDM measurement cell referred to as a co-magnetometer.

In the EDM experiment, we measure two atomic resonance frequencies that are in the electric field parallel to the magnetic field, and anti-parallel to the magnetic field in the OL [3]. The frequency difference is generated by the interaction between the applied electric field and the EDM. The fluctuation of the Zeeman shift, which is caused by the interaction between the magnetic moment and the magnetic field, and the vector light shift (VLS) caused by the high intensity laser field in the OL will lead to dominant components of systematic errors. The VLS can be changed due to the fluctuations of the power and the polarization of the laser source for the OL. The unique solution to eliminate these errors are to monitor the spin frequencies of two atomic species, which have no EDM contribution compared with Fr, and measure the magnetic field and VLS explicitly. Based on this idea, the dual species co-magnetometer is now developed for evaluating the fluctuations of the Zeeman shift and VLS. As the first step, the dual species MOT was developed with two rubidium isotopes of ^{85}Rb and ^{87}Rb using a single external cavity diode laser (ECDL) and an electro-optic modulator (EOM) [4] as shown in Fig. 1. For loading the atoms to the OL, the atoms should be sufficiently cooled. The temperature of atoms was evaluated by the time evolution of the radius of the atomic cloud, which is measured by the absorption imaging method.

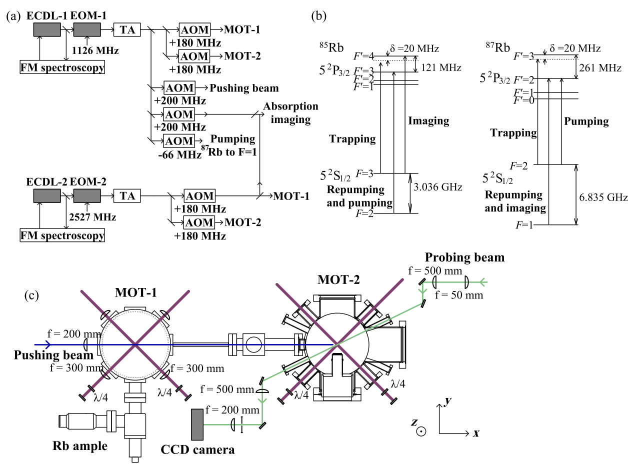

Figure 1. Experimental overview. (a) Schematic diagram of the optical system. (b) Energy levels of ^{85}Rb and ^{87}Rb. (c) Layout of MOT-1 and MOT- 2.

The experimental setup is shown in Fig.1. Four different frequencies of lights were required for the dual-Rb-isotope MOT. Two external cavity diode lasers (ECDL-1 and ECDL-2) were used as light sources as shown in Fig. 1 (a). The light for trapping ^{85}Rb and ^{87}Rb was generated using ECDL-1 and an electro-optic modulator (EOM-1). The frequency difference between the transition of $5S_{1/2}$, F=3

$\rightarrow$ F$'$ =4 in ^{85}Rb and the transition of 5S$_{1/2}$, F=2 $\rightarrow$ F$'$ =3 in ^{87}Rb was 1126 MHz. The frequency of ECDL-1 was stabilized to the resonant frequency of the transition in ^{85}Rb. The RF signal with frequency of 1126 MHz was put into EOM-1 to generate sidebands. The light for repumping ^{85}Rb and ^{87}Rb from the state of 5S$_{1/2}$, F=2 in ^{85}Rb and 5S$_{1/2}$, F=1 in ^{87}Rb was produced using ECDL-2 and EOM-2. The frequency difference between the transition 5S$_{1/2}$, F=2 $\rightarrow$ F$'$ =3 in ^{85}Rb and the transition5S$_{1/2}$, F=1 $\rightarrow$ F$'$ =2 in ^{87}Rb was 2527 MHz. The frequency of ECDL-2 was stabilized to the resonant frequency of the transition in ^{87}Rb. The RF signal with frequency of 2527 MHz was put into EOM-2 for generation of sidebands. The powers of the laser beams with sidebands were amplified by the tapered amplifiers. The frequencies of the lights for trapping and repumping were shifted by +180 MHz using acousto-optic modulators.

First, Rb atoms were cooled and trapped in MOT-1. A pushing beam was used to transfer cold Fr atoms from MOT-1 to MOT-2 (right chamber shown in Fig. 1 (c)) where the ^{85}Rb and ^{87}Rb are trapped at the same time to be used as the co-magnetometer. The typical vacuum pressure in MOT-1 was 3×10^{-8}Pa, and that in MOT-2 was 5×10^{-10}Pa. The magnetic fields are 10 G/cm and 22 G/cm around the center in MOT-1 and MOT-2. To evaluate the temperature and number of trapped atoms, the atomic cloud distribution in MOT-2 was observed. The absorptive shadow image formed by the cloud in the probe beam was captured with a charge-coupled-device (CCD) camera. Fig. 2 shows the absorption images of ^{85}Rb and ^{87}Rb atoms. The temperature of the atoms T can be estimated by the time-evolution of the radius of the atomic clouds r(t), as follows.

$$r(t) = \sqrt{r_0^2 + \frac{2k_B T}{m} t^2} \tag{2}$$

where k$_B$ is the Boltzmann constant and m is the mass of the atom. Fig. 3 shows the radius of each isotope that was obtained after a certain delay time. The black lines represent the theoretical curve of Eq. (2) fitting to each data. The obtained temperature T of ^{85}Rb and ^{87}Rb atoms were $(2.1 \pm 0.4) \times 102\ \mu$ K and $(1.1 \pm 0.3) \times 102\ \mu$ K, respectively. To load atoms to the OL efficiently, the temperature of the atoms should be lowered further using polarization gradient cooling.

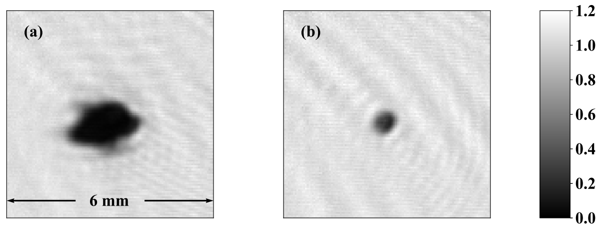

Figure 2. Absorption images of (a) ^{85}Rb and (b) ^{87}Rb atoms.

The dual species co-magnetometer, which measures

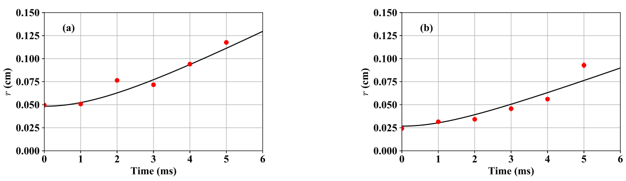

Figure 3. Time of flight of (a) ^{85}Rb and (b) ^{87}Rb atoms.

both the magnetic field and the VLS, is crucial in the electron EDM search using laser-cooled Fr atoms. The present status of the development of the dual-Rb-isotope co-magnetometer was reported. At present, the MOT system was successfully developed using two individual lasers and EOMs. The number and temperature of the two isotopes were measured for ^{85}Rb and ^{87}Rb. In the next step, the ^{85}Rb and ^{87}Rb will be loaded into the optical lattice, and the spin frequencies for those isotopes will be measured in the OL.

References

[1] Maxim Pospelov, Adam Ritz, Annals Phys. **318** (2005) 119-169.

[2] B.K. Sahoo, T. Aoki, B.P. Das, Y. Sakemi, Phys.Rev. A**93** (2016) 032520.

[3] Y. Sakemi, KOGAKU:光学 (Optical Society of Japan) Vol.**47** (2018) 301-305

[4] A. Uchiyama et. al., Rev. Sci. Instrum. **89** (2018) 123111

Development of a Novel Surface Ionizer for the Electron EDM Measurement using Francium

N. Ozawa, H. Nagahama, T. Hayamizu, J. Tsutsumi[a], K. S. Tanaka[b], K. Harada[b], A. Uchiyama[b], and Y. Sakemi

Center for Nuclear Study, Graduate School of Science, University of Tokyo
[a]Department of Physics, Rikkyo University
[b]Cyclotron and Radioisotope Center, Tohoku University

Our Universe today consists of more matter than antimatter, despite the scenario that they originated as pairs. A possible origin for this asymmetry is the violation of the CP symmetry [1], which also could be considered as the violation of T symmetry under the CPT theorem. A finite electron electric dipole moment (eEDM) would be an indication of a T violation in the lepton sector [2].

We plan to use ^{210}Fr to conduct an experiment for the high-precision measurement of the eEDM. The advantages for using Fr are the eEDM enhancement factor of $\approx 10^3$ which is the largest among the ground state atoms [4,5], the possibility of high-intensity production through fusion reaction [6], and the possibility of laser cooling [7]. The high-intensity production leads to a large number of Fr atoms being measured and the laser cooling allows a long measurement time, both of which improves the measurement precision.

For the high-intensity Fr beam production, we have developed a Fr ion source. ^{210}Fr ions are produced through the fusion reaction ^{197}Au (^{18}O, xn) $^{215-x}$Fr. The reaction cross-section is maximized for $x = 5$ when a 100 MeV beam of ^{18}O is used [6].

The fusion takes place inside the Au target where the primary ^{18}O beam is injected into. The produced Fr diffuses thermally within the solid Au, of which some of them reach the top surface of the target where they are desorbed due to thermal energy. Since the first ionization potential of Fr is smaller than the work function of Au, the majority of the desorbed Fr are emitted as ions. By applying a high voltage to the Au target itself, these ions are electrostatically pushed away to form a Fr$^+$ ion beam. The extracted Fr$^+$ ions are then neutralized to form a Fr atom beam, and then laser cooled.

Our ion source consists of the chamber, the Au target, and a plate electrode which maneuvers the desorbed Fr ions from the target surface. In the RIKEN facility, the primary beamline is directed vertically downwards, thus requiring the Fr beam to be bent as it is extracted. Considering the balance between the geometrical limitations of the experimental area and the feasibility of beam transportation, the bending angle of 45 degrees has been chosen, as shown in Fig. 1.

Since the target will be heated due to the injected beam, care must be taken not to melt it, and even when it is accidentally melted, the Au must stay in position. Therefore, the surface of the Au target must be kept horizontally flat. Since the target also works as an electrode to push the Fr

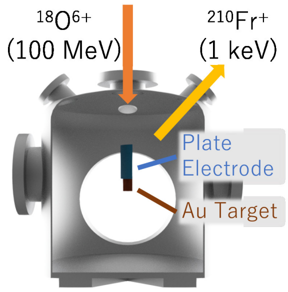

Figure 1. The conceptual image of the Fr ion source. The Au target is kept horizontally flat to avoid accidental spillovers. The plate electrode must be used to guide the Fr beam to the 45-degree extraction direction.

ions outwards, it creates an electric field in the upwards direction. By using the additional plate electrode with an applied voltage V_C, the beam is bent 45 degrees.

In the design process, each electrode part has been constructed graphically using the Autodesk Inventor 3D CAD software. Then, by importing the graphics into SIMION, an electromagnetic field and particle trajectory simulation software using the finite element method, the resulting particle trajectory has been calculated. To evaluate the performance of the plate electrode, a virtual beam profile monitor is placed outside of the chamber where the slice of the beam is observed.

For the particle trajectory simulation, 10^5 ^{210}Fr$^+$ ions with thermal energy 0.1 eV has been ejected isotropically from the surface of the Au target. The initial positions on the Au surface follow a Gaussian distribution of standard deviation 1.5 mm, which is assumed to resemble the injected ^{18}O beam profile. The Au target itself was applied a voltage of $V_A = 1000$ V. The beam profile is displayed as a 2D histogram. Also, the transmission rate has been defined as the percentage of the generated Fr ions that reached the beam profile monitor.

The first attempt using the plate shown in Fig. 2 is shown in Fig. 3. Here, similar ion sources created at the CYRIC, Tohoku University [8], and the LNL (Italy) [6] are used as references. The transmission rate is less than 1%. Based on the numerous simulations conducted with this plate electrode, the beam is bent more as V_C is increased with $V_C > V_A$, but at the same time the transmission rate decreases. It can be observed that the produced Fr ions are trapped at the surface of the Au target, since the plate electrode forms a high electrostatic potential for the ions at the surface of the target.

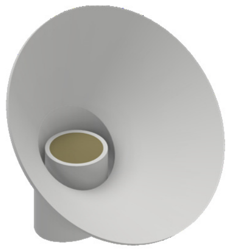

Figure 2. The plate electrode designed as a first attempt. It is a 45-degree tilted version of the electrodes developed at CYRIC [8] and LNL [6]. The coin in the center is the Au target.

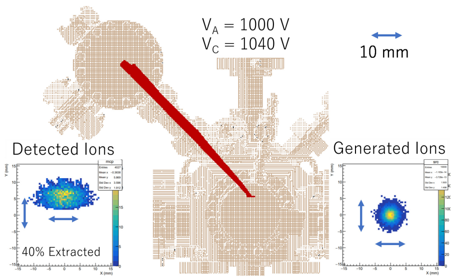

Figure 3. The beam trajectory simulation using the electrode in Fig. 2. The applied voltage was $V_C = 1040$ V, and the transmission rate was 40%. The beam is not bent enough, and most of the Fr ions are not extracted.

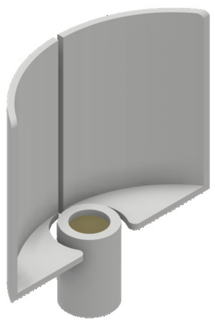

Figure 4. The plate electrode optimized for the 45-degree extraction. The coin in the center is the Au target.

The electrostatic field created by this plate electrode in the 45-degree direction is distorted by that of the Au target kept horizontally flat. This distortion is compensated for by altering the plate electrode geometry as shown in Fig. 4. By using this plate, the beam trajectory in Fig. 5 can be obtained.

It must be pointed out that the relationship of V_C and V_A differ in the two cases. In the former case, by applying a V_C larger than V_A, the beam is bent forcibly. In the latter case however, the geometry of the plate electrode is optimized so that the beam is excessively bent already when $V_C = V_A$. By lowering the value of V_C from V_A, the beam direction approaches 45 degrees while the beam focal point moves further away, creating a thin beam. By finding the balance between these two effects in the $V_C < V_A$ region, the beam in Fig. 5 can be achieved.

The installation of this ion source is planned in the autumn of 2019, where the first test using an ^{18}O beam from the RIKEN AVF cyclotron will be conducted. The ion source in LNL [5] was capable of producing 10^6 ^{210}Fr$^+$ ions

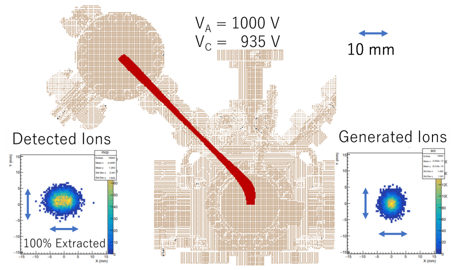

Figure 5. The beam trajectory simulation using the electrode in Fig. 4. The applied voltage was $V_C = 935$ V, and the transmission rate was 100%. The beam is directed straight towards the 45 degrees direction, and it is focused far enough not to hit the walls of the beamline.

per second given the primary ^{18}O beam of 10^{12} per second. Since the primary beam intensity at the RIKEN AVF Cyclotron is expected to reach 10^{13} per second, the produced Fr ion beam is expected to reach 10^7 per second, if the extraction efficiency of the ion source reaches 100%, as simulated. This corresponds to a factor 10 improvement of the number of produced Fr compared to the LNL experimenal setup, which is equivalent to a factor $\sqrt{10}$ improvement of the EDM measurement precision.

The resulting EDM measurement precision could be improved even more if each component of the experimental apparatus is optimized. This includes the neutralization of Fr ions, the laser cooling of the produced Fr atoms, and the beam transport efficiency due to the beam size. By developing the other components with the efficiencies of at least those of CYRIC, the eEDM measurement precision could reach the current limit of the order of 10^{-29} $e$cm.

References

[1] A. D. Sakharov, Sov. Phys. Usp. **34** (1991) 392.
[2] M. Popeslov and A. Ritz, Ann. Phys. **318** (2005) 119.
[3] ACME Collaboration, Nature **562** (2018) 355.
[4] D. Mukherjee, B. K. Sahoo, H. S. Nataraj, and B. P. Das, J. Phys. Chem. A **113** (2009) 12549.
[5] T. M. R, Byrnes, V. A. Dzuba, V. V. Flambaum, and D. W. Murray, Phys. Rev. A **59** (1999) 3082.
[6] G. Stancari, S. Veronesi, L. Corradi, S. N. Atutov, R. Calabrese, A. Dainelli, E. Mariotti, L. Moi, S. Sanguinetti, and L. Tomassetti, Nucl. Instrum. Meth. A **557** (2006) 390.
[7] J. E. Simsarian, A. Ghosh, G. Gwinner, L. A. Orozco, G. D. Sprouse, and P. A. Voytas, Phys. Rev. Lett. **76** (1996) 3522.
[8] H. Kawamura, S. Ando, T. Aoki, H. Arikawa, K. Harada, T. Hayamizu, T. Inoue, T. Ishikawa, M. Itoh, K. Kato, L. Köhler, K. Sakamoto, A. Uchiyama, and Y. Sakemi, Rev. Sci. Instrum. **87** (2016) 02B921.

Experimental Nuclear Physics: PHENIX Experiment at BNL-RHIC and ALICE Experiment at CERN-LHC

Highlights of ALICE data taking in 2018

T. Gunji

Center for Nuclear Study, Graduate School of Science, The University of Tokyo, Japan

1. Introduction

ALICE is one of the experiments at the Large Hadron Collider (LHC) in CERN [1]. ALICE is dedicated to the studies of strongly interacting matter at extreme energy densities, where a new phase of matter composed of quarks and gluons, called quark-gluon plasma, forms.

The ALICE detector is designed to measure as many observables as possible in relativistic heavy-ion collisions for a wide coverage of transverse momentum and pesudorapidity [1]. ALICE detector consists of many different subdetectors, where each provides a different piece of information.

There are three main forward detectors in ALICE. T0 is the fast timing and trigger detector in ALICE, that is composed of two arrays (T0-A and T0-C) of Cherenkov counters with the interaction point (IP) in between. The V0 detector consists of two arrays of 32 scintillating counters, called V0A and V0C, that are located on either side of IP. V0 provides minimum bias triggers and centrality triggers. The ZDCs are located 115 meters away from the IP on both sides. The ZDCs are the calorimeters which detect the energy of the spectator nucleons and determine the geometry of collisions. It is composed of four calorimeters, two to detect protons (ZP) and two to detect neutrons (ZN).

Central barrel detector is an ensemble of cylindrical detectors, that includes of 6 layers of silicon detectors (ITS), time projection chamber (TPC), transition radiation detector (TRD), and time-of-flight detector (TOF). It is installed in the L3 solenoid magnet. It measures charged particle trajectories and charged particle's momenta and determines the collision vertices. It also provides the particle identification ($e^{\pm}$, $\pi^{\pm}$, $K^{\pm}$, $p(\bar{p})$, d, etc) by using several techniques such as dE/dx in the ITS, TPC, and TRD, transition radiation from electrons in the TRD, and arrival time of each particle in the TOF. The ITS and TPC are so precise that they can identify the secondary vertices of heavy-flavors ($D^{0,\pm}$, Λ_c) and hyperons (Λ, Ξ, Ω).

The EMCal and PHOS are the electromagnetic calorimeters in the central barrel with limited coverage in azimuth and measure photons and jets. They provide photon and jet triggers to the ALICE.

There is the muon spectrometer in ALICE at forward rapidity. It consists of a front absorber, five tracking stations with the third one located inside a warm dipole, an iron wall and triggering chambers. It mainly measures muons from vector meson and heavy-flavor decays and provides the muon triggers.

The author was endorsed as Deputy Run Coordinator in 2018 and was responsible to conduct ALICE experiment and to take high quality data. Below is the summary of ALICE data taking in pp and Pb-Pb collisions in 2018.

2. ALICE pp running in 2018

The goal of 2018's pp collisions is to deliver 60 fb^{-1} to ATLAS and CMS. ALICE's plans in 2018 were to accumulate minimum bias (MB), high-multiplicity events (HM) triggered by V0 and ITS, and rare triggered data for photons, jets, and muons. The availability of the LHC over the time was 66% and 50% of the time was spent for the physics beam. ALICE was running at 200-250 kHz pp interaction rate and downscaled minimum bias (MB) and rare triggered data (HM, γ, jets, muons) were taken simultaneously. Average efficiency of ALICE data taking was 92%. Total delivered luminosity in ALICE was 27.3 pb^{-1}. ALICE accumulated $\sim$ 1000 M MB events, 450 M and 400 M HM events by V0 and ITS, 12 pb^{-1} muon triggered data, and 5 pb^{-1} photon and jets triggered data. Those samples were the largest samples ever taken yearly in ALICE.

During pp period, we raised the interaction rate up to 750 kHz and 4 MHz, where particle fluxes are similar to 8 kHz and 50 kHz Pb-Pb collisions, respectively. Both are the expected rates in Pb-Pb collisions in 2018 and beyond 2021. By conducting those tests, we tried to identify the issues for the detectors in running under high rate of Pb-Pb collisions. Based on the tests at 750 kHz, further optimizations of running parameters (HV settings, front-end parameters, and so on) for each subdetector were made for 2018's Pb-Pb collisions. Another special tests for mitigating the field distortions in the TPC were performed under various collision rates and various settings of gating grid voltage and cover electrode voltages.

3. ALICE Pb-Pb running in 2018

The goal of the LHC for 2018's Pb-Pb collisions was to deliver 1 nb^{-1} to ATLAS, CMS, and ALICE. New beam optics with lowest β^* of 0.5 m for ALICE was firstly employed. However, for the first 1/3 of the Pb-Pb running period, ALICE luminosity was found to be lower than expected. It was found that the beam sizes at IR2 (ALICE) were 40% larger in both planes compared to IR1 (ATLAS) and IR5 (CMS). LHC had adjusted two skew quadrupoles on both sides of IR2. ALICE got 0.905 nb^{-1} delivered in 2018, that is 50% larger luminosity compared to 2015.

In the beginning of 8 kHz Pb-Pb collisions, field distortions of the TPC were checked. Figure 1 and Figure 2 show space-point distortions ($\delta r\phi$) as a function of TPC sectors (azimuthal angle) and radius from the IP. One can see that the maximum distortions in 2015 were 6 cm, while those in 2018 were 1 cm.

The availability of the LHC over the time was 85% and 50% of the time was spent for the physics beam of Pb-Pb collisions. Average efficiency of ALICE data taking was 85%, that is 7% lower than the efficiency in pp collisions.

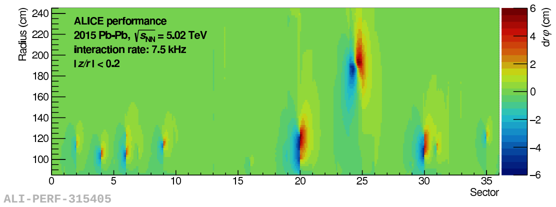

Figure 1. Space point distortion in the TPC in 2015 Pb-Pb collisions

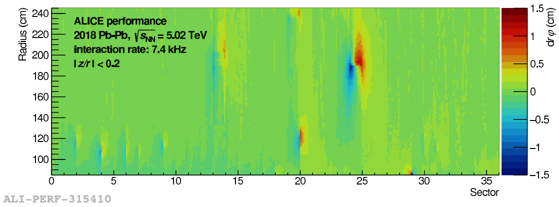

Figure 2. Space point distortion in the TPC in 2018 Pb-Pb collisions

One of the reasons of lower efficiency was that there were some DAQ issues in the first days of Pb-Pb running. Periodically, the number of incomplete events that failed to be flushed in the storage farm and kept in the pileline buffer shot up suddenly and on-going run had to be paused to let DAQ process events, which caused up to 17% loss of the efficiency if affected. Second reason was that due to high particle fluxes in 8 kHz Pb-Pb collisions, SEU of some key detectors happened and had to be recovered. Figure 3 and Figure 4 show the number of recorded events for min bias and centrality triggers and integrated luminosity for various rare triggers, respectively. By mixing MB and centrality triggers, ALICE accumulated 160 M, 133M, and 118M events for MB, 0-10% central, 30-50% mid-central collisions, respectively. The increase of central and mid-central triggered data was x5 in 2018 compared to 2015. ALICE took x2 larger data samples with rare triggers for muons, photons, jets, and ultra-peripheral collision in 2018.

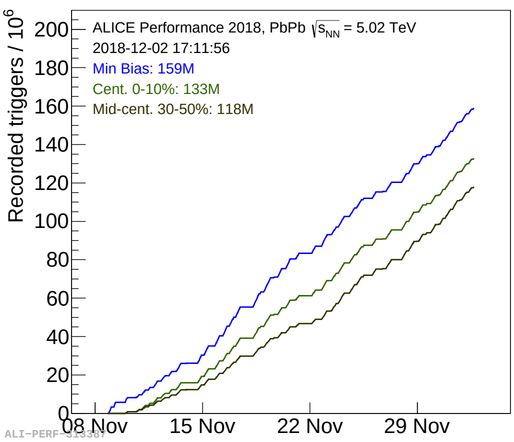

Figure 3. Number of recorded events for min bias and centrality triggers in Pb-Pb collisions (2018 run)

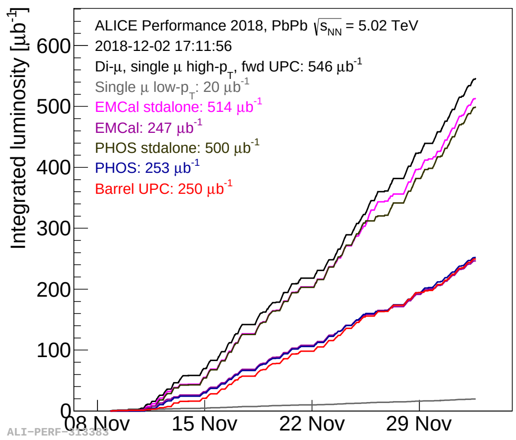

Figure 4. Integrated luminosity for various rare triggers in Pb-Pb collisions (2018 run)

4. ALICE in LS2

After LHC Run2 (2015-2018) operation was over, ALICE was switched to the upgrade mode. During LHC long shutdown 2 (LS2, 2019-2020), ALICE will replace ITS to new 7 layers of all silicon MAPS detectors [2], install five layers of this silicon MAPS detector in front of the muon spectrometer [3], install new GEM readout chambers in the TPC [4], and employ new readout and DAQ systems in order to cope with 50 kHz Pb-Pb collisions [5]. Such upgrade activities are on-going and global commissioning with all detectors and new DAQ systems will start from 2020.

References

[1] ALICE Collaboration, Int. J. Mod. Phys. A 29 (2014) 1430044

[2] ALICE Collaboration, CERN-LHCC-2012-013, CERN-LHCC-2013-024

[3] ALICE Collaboration, CERN-LHCC-2015-001

[4] ALICE Collaboration, CERN-LHCC-2013-020

[5] ALICE Collaboration, CERN-LHCC-2013-019, CERN-LHCC-2015-006

Inclusive J/ψ production in p-Pb collisions with the ALICE detector

S. Hayashi, and T. Gunji

Center for Nuclear Study, Graduate School of Science, University of Tokyo

The study of cold nuclear matter (CNM) effects is essential to understand the properties of a state of matter composed of deconfined quarks and gluons, the quark-gluon plasma, created in relativistic heavy-ion collisions. For the study of CNM effects, p–Pb collisions is be suitable. Furthermore, some results in high-multiplicity p-Pb collisions show collective behavior that is similar to that in Pb-Pb collisions. For J/ψ production, a positive second-order flow coefficient (v_2) was observed at forward and backward rapidity and the origin of this J/ψ v_2 remains an open question [1]. The centrality dependent nuclear modification factor ($Q_{\rm pPb}$) as a function of transverse momentum ($p_{\rm T}$) was also measured at backward and forward rapidity [2]. At backward rapidity, an enhancement of the J/ψ yield was observed around intermediate $p_{\rm T}$ in central p-Pb collisions. On the other hand, the J/ψ yield is strongly suppressed at low $p_{\rm T}$ at forward rapidity. These two observations are qualitatively consistent with Cronin enhancement and the modification of gluon distribution function inside Pb. In this report, collision centrality dependence on the inclusive J/ψ production at mid-rapidity is evaluated to investigate CNM and further nuclear matter effects by sistematicaly investigating J/ψ production as a function of rapidity. The analysis in this report is performed using the data collected with the ALICE detector in 2016 [3]. The collision energy of p–Pb collisions provided by LHC is 5.02 TeV per nucleon in the center-of-mass frame. The events are triggered by minimum bias condition that requires the coincidence of hits in both forward scintillators called as V0A (Pb-going side) and V0C (p-going side) detectors, respectively. The corresponding integrated luminosity is 300 μb^{-1}.

In p–Pb collisions, if there is no nuclear matter effects, particle yield should be proportional to the number of binary collisions ($\langle N_{\rm coll}\rangle$). Therefore we introduce the nuclear modification factor $Q_{\rm pPb}$ expressed as,

$$Q_{\rm pPb} = \frac{\dfrac{dN_{\rm pPb}}{dp_{\rm T}dy}}{T_{\rm pPb}\dfrac{d\sigma_{\rm pp}}{dp_{\rm T}dy}} \quad (1)$$

where $dN_{\rm pPb}/dp_{\rm T}dy$ and $d\sigma_{\rm pp}/dp_{\rm T}dy$ are J/ψ yields in p–Pb collisions and J/ψ cross section in pp collisions, respectively. $T_{\rm pPb}$ is called thickness function defined by $\langle N_{\rm coll}\rangle/\sigma_{NN}$. σ_{NN} is the nucleon-nucleon inelastic cross section. The pp-reference in $Q_{\rm pPb}$ calculation is determined by the measurement recorded in 2017 [4].

In order to suppress selection bias due to the auto-correlation in particle multiplicity distribution, collision centrality is determined by the deposited energy in Zero-Degree Calolimeter (ZDC) located in the Pb-going direction at 112 m away from interaction points.

In the ALICE central barrel, charged track reconstruction is performed using the Inner Tracking System (ITS) composed of silicon pixel, strip, drift detectors and Time Projection Chamber (TPC). Electrons are identified by the deposited energy in the TPC.

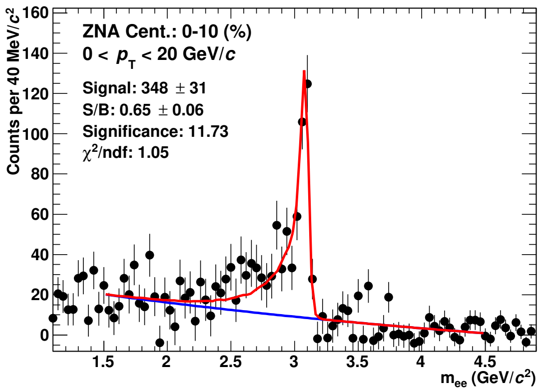

Figure 1. Example of signal and residual background fit for the J/ψ signal extraction in 0-10% centrality. The black marker shows the opposit-sign dielectron invariant mass spectrum after mixed pair subtraction.

After electron selection, the invariant mass is calculated for all electron-positron pairs. In order to extract J/ψ signal from the invariant mass spectrum, 2 steps of background subtraction is adopted. First combinatorial background is subtracted by the event mixing technique. Combinatorial pairs are generated by taking pairs of electrons in a corresponding event and a positron (or electron) in other events which have similar detector acceptance and event activity (i.e. collision vertex, event multiplicity). Mixed pairs are scaled by the ratio of of the yield of same-event and same-sign pairs to the yield of mixed-event and same-sign pairs. After subtraction of combinatorial pairs, residual background mainly from the correlated pairs of heavy flavor decays still exists as shown in Fig 1. To extract J/ψ signal, simultaneous fit with signal shape plus exponential function is applied. J/ψ signal shape is parametrized using Geant 3 based Monte Carlo simulations of J/ψ decays with ALICE detector response. The fit quality is acceptable and the raw yield is evaluated by bin-counting from 2.92 to 3.16 GeV/c^2. Raw yield is corrected by detector acceptance and efficiencies, where same Monte-Carlo as used in signal extraction was used.

The systematic uncertainties on track reconstruction ($\sim$ 4%), electron identification ($\sim$3%), signal extraction ($\sim$1–5%), pp-reference ($\sim$ 7%), and thickness function ($\sim$1-5%) are considered.

Figure 2 shows $p_{\rm T}$-integrated inclusive J/ψ $Q_{\rm pPb}$ as a function of the mean $N_{\rm coll}$. The global uncertainties on the evaluation of integrated luminosity in the pp collisions ($\sim$2.1%) and the calculation of the thickness function($\sim$ 1.8%). The low values of $Q_{\rm pPb}$ from unity is consistent with gluon shadowing or saturation effects.

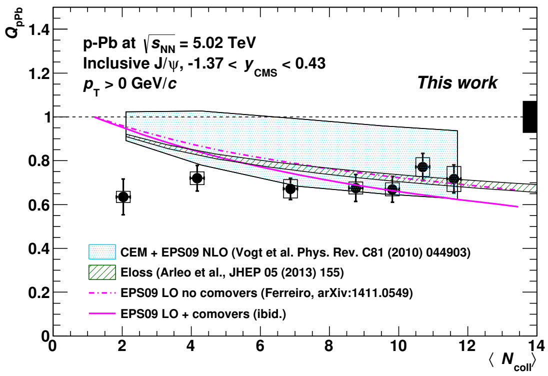

Figure 2. $p_{\rm T}$-integrated inclusive J/ψ $Q_{\rm pPb}$ as a function of the mean $N_{\rm coll}$. The black box around unity shows the global uncertainty.

Figure 3 shows inclusive J/ψ $Q_{\rm pPb}$ as a function of the mean $N_{\rm coll}$ in lower $p_{\rm T}$ ($0 < p_{\rm T} < 3$ GeV/c) and higher $p_{\rm T}$ ($3 < p_{\rm T} < 14$ GeV/c) ranges. Monotonic increase of $Q_{\rm pPb}$ can be seen with respect to $N_{\rm coll}$ at higher $p_{\rm T}$. At low $p_{\rm T}$, suppression is very slightly stronger up to $\langle N_{\rm coll} \rangle \sim 10$. The suppression trend as a function of $p_{\rm T}$ is qualitatively consistent with the trend in forward J/ψ $Q_{\rm pPb}$. In central collisions ($< 20\%$), the low $p_{\rm T}$ samples also show the increasing trend similar to higher $p_{\rm T}$ samples. The enhancement at high $p_{\rm T}$ is qualitatively described by Cronin effect [5]. This effect only modified the momentum distribution and the total yield is not affected.

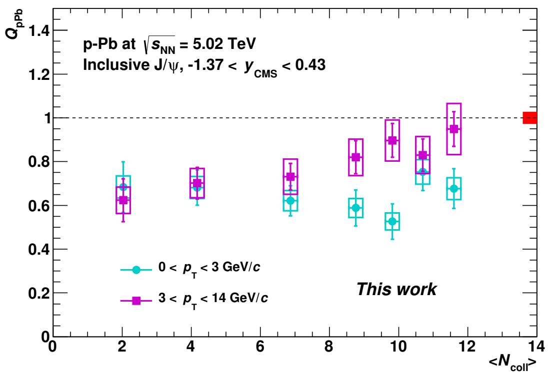

Figure 3. J/ψ $Q_{\rm pPb}$ as a function of the mean $N_{\rm coll}$ in lower $p_{\rm T}$ ($0 < p_{\rm T} < 3$ GeV/c) and higher $p_{\rm T}$ ($3 < p_{\rm T} < 14$ GeV/c) ranges. The red box around unity shows the global uncertainty.

As a summary, the centrality dependence of the inclusive J/ψ production in p–Pb collisions is presented. In the $p_{\rm T}$ dependent $Q_{\rm pPb}$ at mid–rapidity, increasing trend can be seen for high $p_{\rm T}$ J/ψ in central collisions. The $p_{\rm T}$-integrated yield increases as increasing $\langle N_{\rm coll} \rangle$at backward rapidity, where the charged particle multiplicity is relatively higher than mid and forward rapidity. Therefore the multiplicity dependence on J/ψ production is a key measure to understand J/ψ production in p–Pb collisions. The detail analysis such as the correlation of J/ψ production and the collective motion in high multiplicity events is promising in LHC-Run3 and Run4.

References

[1] ALICE Collaboration, Phys. Lett. B **780** (2018) 7
[2] B. Paul for the ALICE Collaboration, Nucl. Phys. A **982** (2019) 739
[3] ALICE Collaboration, Int. J. Mod. Phys. A **29** (2014) 1430044
[4] ALICE Collaboration:https://cds.cern.sh/record/2317188
[5] J. W. Cronin *et al* , Phys. Rev. D **11** (1975) 3105
[6] P. Braun-Munzinger and J. Stachel, Nature **448** (2007) 302 - 309
[7] C. Zhang *et al*, Phys. Rev. Lett **122** (2019) 172302
[8] ALICE Collaboration, arXiv:1907.03169 (2019)

Pseudo-rapidity dependence of v_2 in p–Pb collisions with ALICE

Y. Sekiguchi and T. Gunji for the ALICE Collaboration

Center for Nuclear Study, Graduate School of Science, the University of Tokyo

1. Introduction

Measurements of long-range two-particle correlations provide critical insights into the properties of the matter created in heavy-ion collisions. The long-range correlations in the rapidity space in near-side angular pairs, called ”ridge”, were firstly observed in Au–Au collisions at $\sqrt{s_{\rm NN}}$= 200 GeV at RHIC [1, 2]. The long-range correlations are derived from the collective expansion of the initial collision geometry and its fluctuations. A similar structure has also been observed in high-multiplicity *pp* and p–Pb collisions at the LHC [3]. The measurements of the particle productions with large rapidity gaps and the centrality dependence are important for quantifying the collective expansion. This analysis aims to explore the partonic collectivity by measuring long-range two-particle correlations using forward detectors in p–Pb collisions at $\sqrt{s_{\rm NN}}$=5.02 TeV.

2. Analysis

The minimum bias data of p–Pb collisions at $\sqrt{s_{\rm NN}}$=5.02 TeV in 2016 are used (∼600M events). The main subsystems in ALICE used in this analysis are the Time Projection Chamber (TPC) and the Forward Multiplicity Detector (FMD). The TPC is used for tracking of charged particles. Its acceptance covers 2π in azimuthal angle and a pseudo-rapidity interval $|\eta| < 0.8$. The FMD is composed of three arrays at -3.4< η <-1.7 ,1.7< η <3.68, and 3.68< η <5, respectively (Table 1). The position of the reconstructed

Array	Ring	φ segments	η coverage
FMD1	-	20	3.68 -5.03
FMD2	FMD2i	20	2.28 -3.68
	FMD2o	40	1.70 - 2.29
FMD3	FMD3i	20	-2.29 - -1.70
	FMD3o	40	-3.40 - -2.01

Table 1. FMD pseudo-rapidity coverage and azimuthal segments.

vertex along the beam direction is required to be within 10 cm from the interaction point. To determine centrality, V0A detector which is located in the Pb-going direction is used. The V0A detector consists of 32 scintillating counters. The correlations between trigger particles and associated particles are measured as a function of the azimuthal angle difference $\Delta\varphi$ and pseudo-rapidity difference $\Delta\eta$. The trigger particles are unidentified charged hadrons detected in the TPC, while associated particles are measured by the FMD. The multiplicities measured in each FMD segment are treated as the number of tracks in the average φ and η of each segment. The correlation function as a function of $\Delta\eta$ and $\Delta\varphi$ between two charged particles is defined as

$$\frac{1}{N_{\rm trig}}\frac{{\rm d}^2 N_{\rm asso}}{{\rm d}\Delta\eta {\rm d}\Delta\varphi} = \frac{S(\Delta\eta,\Delta\varphi)}{B(\Delta\eta,\Delta\varphi)}, \qquad (1)$$

where $N_{\rm trig}$ is the total number of triggered particles in the event class, the signal distribution $S(\blacksquare\eta,\blacksquare\varphi) = \frac{1}{N_{\rm trig}}\frac{{\rm d}^2 N_{\rm same}\times w_i}{{\rm d}\Delta\eta{\rm d}\Delta\varphi}$ is the associated yield per trigger particle from the same event, and the background distribution $B(\Delta\eta,\Delta\varphi) = \alpha\frac{{\rm d}^2{\rm N_{mixed}}\times{\rm w_i}}{{\rm d}\Delta\eta{\rm d}\Delta\varphi}$ accounts for pair acceptance and pair efficiency. It is constructed by taking the correlations between trigger particles in one event and associated particles from other events in the same event class. $w_{\rm i}$ is the multiplicity in each FMD segment. The α factor is chosen so that $B(\Delta\eta,\Delta\varphi)$ is unity at the maximum bin. Figure 1 shows the associated yield per unidentified hadron trigger particles for TPC-FMD1,2 at 2.9 < η <3.1 (left) and TPC-FMD3 at -3.1< η <-2.9 (center) with 0.2< $p_{T,trig}$ <3GeV and FMD1,2–FMD3 correlations between 4.6 < η <4.8 and -3.1< η <-2.9(right) in 0–5% and 60–100% centrality classes, respectively. Centrality class corresponds to the collision impact parameter b. The long-range correlations in the near-side ($-\pi/2 < \Delta\varphi < \pi/2$), called ridge, can be observed in 0–5% events for TPC-FMD1,2 (Pb-going), TPC-FMD3 (p-going), and FMD1,2-FMD3, while it is not significant in 60–100% events.

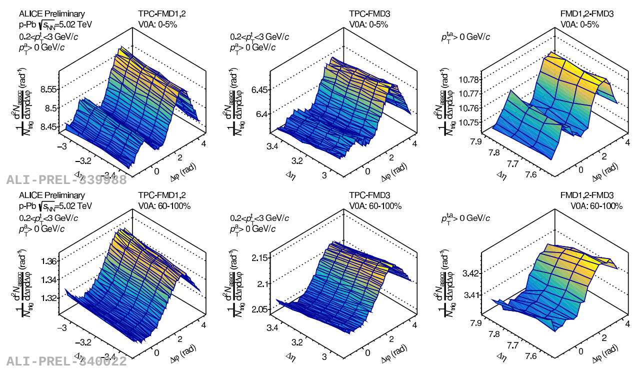

Figure 1. Correlation functions between TPC-FMD1,2, TPC-FMD3, and FMD1,2-FMD3 in central and peripheral collisions, respectively

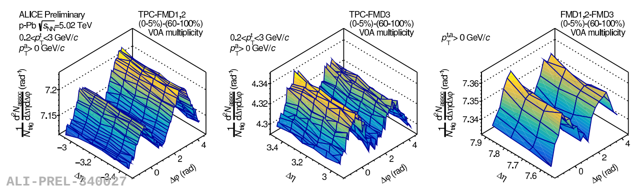

Figure 2. Correlation functions after the peripheral subtraction between TPC-FMD1,2, TPC-FMD3, and FMD1,2-FMD3 , respectively

The correlation function in the peripheral collisions (60–100%) is subtracted from that in the central collisions (0–5%) to reduce the non-flow contaminations from jets and

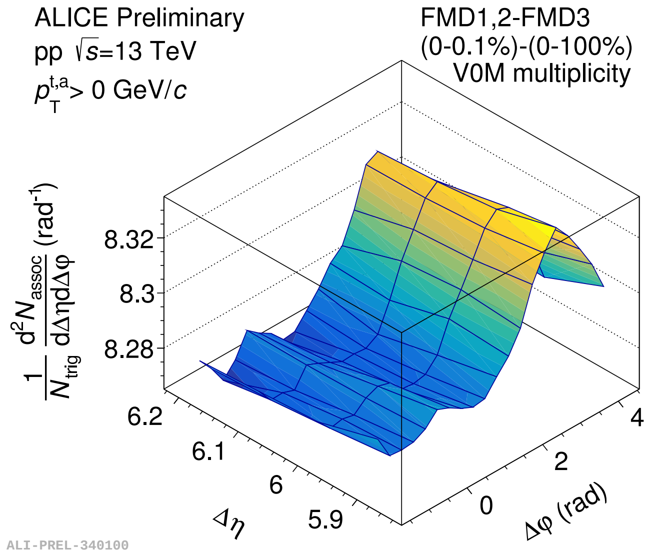

Figure 3. Projection onto $\Delta\varphi$ of correlation functions after the peripheral subtraction between TPC-FMD1,2, TPC-FMD3, and FMD1,2-FMD3 , respectively

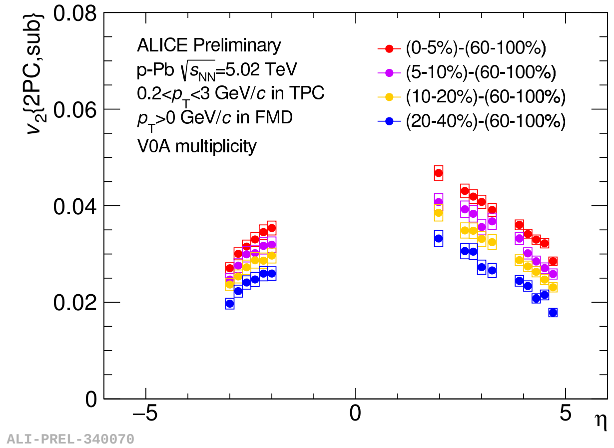

Figure 4. v_2 as a function of η.

resonance decay. Figure 2 shows correlation functions in central events after the peripheral subtraction ((0–5%)-(60–100%)) for TPC-FMD1,2 (left) and TPC-FMD3 (center), and FMD1,2-FMD3(right). Long-range structure on both the near and away side is observed up to $\Delta\eta \sim 8$ in central p–Pb collisions. Figure 3 shows the projection of correlation functions to $\Delta\varphi$ in central collisions after the peripheral subtraction ((0–5%)-(60–100%)) for TPC-FMD1.2 (left),TPC-FMD3 (center), and FMD1,2-FMD3(right). To quantify the near-side and away-side excess structures, the Fourier function is used to fit to the data.

$$\frac{1}{N_{\text{trig}}}\frac{\text{dN}_{\text{asso}}}{\text{d}\Delta\varphi} = a_0 + 2\sum_{n=1}^{3} cos(n\Delta\varphi). \tag{2}$$

Form the relative modulations $V_n(2PC) = a_n/(a_0+b)$, the azimuthal anisotropy at a certain η can be obtained by using the three-sub event method as below. b is the baseline which is the minimum yield of the 60–100% event class. To assume common event plane over pseudo-rapidity, V_2(2PC) is the product of $v_2(\eta_1)$ and $v_2(\eta_2)$. The pseudo-rapidity dependent of v_2 is the obtained as

$$v_2(\eta_{FMD1,2}) = \sqrt{\frac{V_2(\eta_{TPC},\eta_{FMD1,2})V_2(\eta_{FMD1,2},\eta_{FMD3})}{V_2(\eta_{TPC},\eta_{FMD3})}}. \tag{3}$$

Figure 4 shows the extracted v_2 as a function of η for different event class. The v_2 has centrality and pseudo-rapidity dependence. The v_2 in the Pb-going direction is larger than in the p-going direction. The trend is similar to the distribution of $dN_{ch}/d\eta$.

3. Summary and Outlook

The long-range two-particle correlations are measured by using the TPC and the FMD in p-Pb collisions at $\sqrt{s_{\text{NN}}}$=5.02 TeV. The long-range correlations are observed up to $\Delta\eta \sim 8$ in central p–Pb collisions. The pseudo-rapidity dependence of v_2 is extracted by using the three-sub event method. The pseudo-rapidity dependence of v_2 has centrality and pseudo-rapidity dependence. The trend is similar to the distribution of $dN_{ch}/d\eta$. We will discuss the properties of created hot matter in small system with comparisons with theoretical calculations. To investigate onset of "flow" and non-flow in small system, the same measurement in pp is ongoing.

References

[1] STAR Collaboration, Phys. Rev. C80 (2009) 064912.
[2] PHOBOS Collaboration, Phys. Rev. Lett. 104 (2010) 062301.
[3] CMS Collaboration, JHEP 09 (2010) 091.

Direct photon measurement via external conversions in pp and -pPb collisions at LHC-ALICE

H. Murakami, T. Gunji[a], for the ALICE collaboration

Department of Physics, University of Tokyo
[a]*Center for Nuclear Study, Graduate School of Science, University of Tokyo*

1. Introduction

High energy heavy-ion collisions provide an unique opportunity to study quark gluon plasma (QGP), a deconfined state of quarks and gluons. For years, experiments were carried out at the RHIC and the LHC, observed many interesting phenomena in heavy-ion collisions that confirm formation of QGP. In particular, enhancement of direct photon production at low transverse momentum is thought to be thermal radiation from QGP and interpret as an evidence of the QGP [1, 2].

In recent years, collective behavior of hadrons in small colliding systems such as high multiplicity pp and p-Pb collisions was found at the LHC [3, 4]. The discovery was surprising because such behavior was believed to be a unique phenomenon of heavy-ion collisions. So far, it is not yet clear if it indicates the formation of thermalized systems such as QGP even in small collision systems [5], or it is due to the dynamics of initial gluon fields [6]. If the QGP is created in such colliding systems, the thermal photons are expected to be emitted from the QGP.

In this study, we looked for the direct photons in p-Pb collisions at $\sqrt{s_{\mathrm{NN}}} = 5.02$ TeV to discuss the possibility of thermalized system in p-Pb collisions. To detect photons, photon conversion method (PCM) is employed since the method is advantageous to measure photons down to low p_{T}, where thermal photons dominate. This report presents the status of direct photon measurement in p-Pb collisions.

2. Analysis overview

The term direct photons indicates photons emerge from particle collisions and not from particle decays. Direct photons include the thermal radiations and photons produced in elementary hard QCD process such as $q\bar{q} \to g\gamma$ and $qg \to q\gamma$. They are distinguished from decay photons such as π^0 and $\eta \to \gamma\gamma$. To extract direct photon signal, the subtraction technique is used. In this method, we first deduce the inclusive photon spectrum and then statictically subtract the spectra of decay photons. The invariant yield of direct photons $\gamma_{\mathrm{dir}}(p_{\mathrm{T}})$ can be expressed in terms of the inclusive photons $\gamma_{\mathrm{inc}}(p_{\mathrm{T}})$ and that of decay photons $\gamma_{\mathrm{dec}}(p_{\mathrm{T}})$:

$$\gamma_{\mathrm{dir}}(p_{\mathrm{T}}) = \gamma_{\mathrm{inc}}(p_{\mathrm{T}}) - \gamma_{\mathrm{dec}}(p_{\mathrm{T}}) \quad (1)$$

$$= (1 - R_{\gamma}^{-1}(p_{\mathrm{T}})) \cdot \gamma_{\mathrm{inc}}(p_{\mathrm{T}}) \quad (2)$$

where $R_{\gamma}(p_{\mathrm{T}}) = \gamma_{\mathrm{inc}}(p_{\mathrm{T}})/\gamma_{\mathrm{dec}}(p_{\mathrm{T}})$ is the fraction of photons from hadron decays. If $R_{\gamma}(p_{\mathrm{T}}) > 1$, it implies direct photon signal. In order to obtain decay photon spectra, π^0 and η, which are the major sources of decay photons, are deduced by photon conversion method. Other sources are estimated by using m_T scaling [7] from measured π^0 and η spectra.

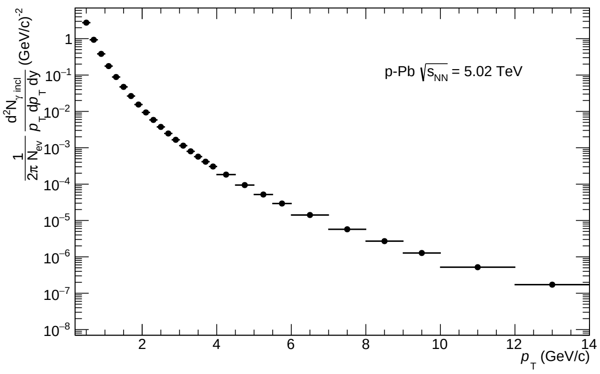

Figure 1. Inclusive photon spectrum in p-Pb collisisons at $\sqrt{s_{NN}} = 5.02$ TeV

3. Experimental setup

A brief description of experimental setup is given. Details of ALICE detectors can be found in [8]. Photons are reconstructed via e^+e^- pairs which are converted in a detector material. Tracking is made by using ALICE central detector system consisting of the Inner Tracking System (ITS), the Time Projection Chamber (TPC). The event multiplicity is estimated with V0 detectors, which are made of two arrays of scintillation counters (V0A and V0C) placed on forward and backward of the ALICE interaction point. V0 detectors also provide trigger information. The minimum bias trigger requires a hit in the V0A and the V0C.

4. Data analysis

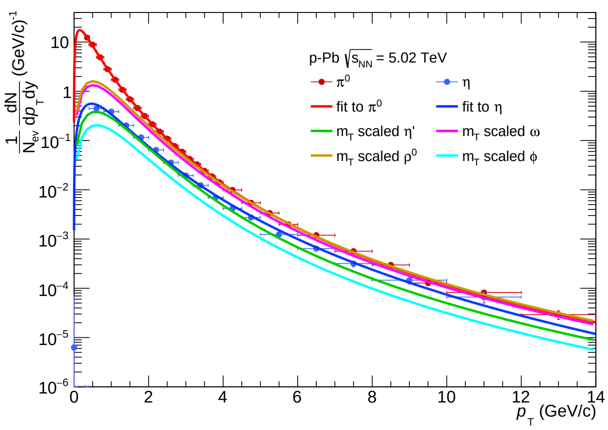

Figure 2. Invariant yield of π^0 (red point) and η (blue point). The spectra are fitted with modified Hagedorn respectively. Other particles (η', ω, ρ, ϕ) are obtained via m_{T} scaling.

In 2016, ALICE collected 600 M events of minimum bias

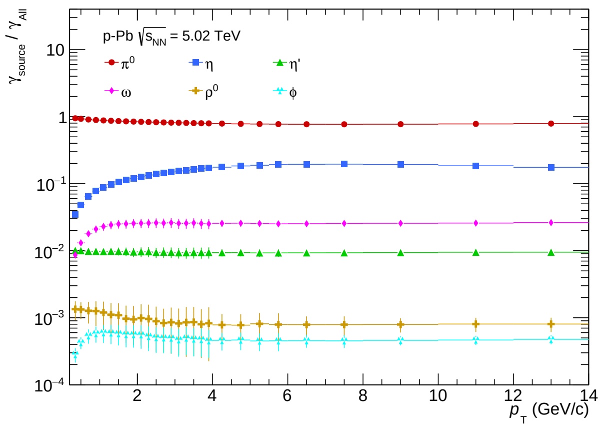

Figure 3. Relative decay photon contribution to the total decay photon yield.

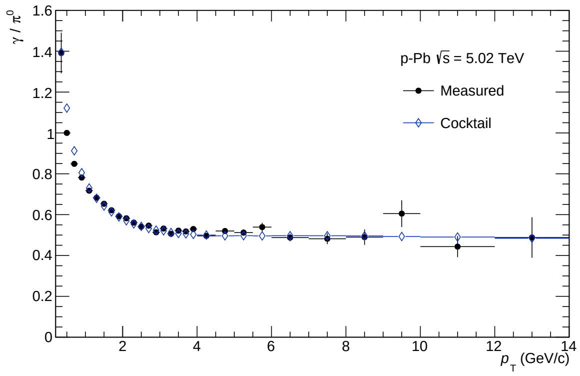

Figure 4. Ratio of inclusive photon over the π^0 spectrum.

triggered data in p-Pb collisions at $\sqrt{s_{NN}} = 5.02$ TeV. The e^+e^- pairs from photon conversions are reconstructed with the V^0 reconstruction method which finds particles from offvertex decay. Electrons identified by the dE/dx information of TPC. To improve photon purity, several selection criteria, like constraints on invariant mass, opening angle, and topological cuts are applied. Radius distribution of reconstructed photons are compared with MC simulations, the difference between and MC is treated as the correction factor.

Inclusive photon spectra $\gamma_{\mathrm{inc}}(p_{\mathrm{T}})$ is given by as follows:

$$\gamma_{\mathrm{inc}}(p_{\mathrm{T}}) = \gamma_{\mathrm{rec.}}(p_{\mathrm{T}}) \times P(p_{\mathrm{T}}) \times \frac{1}{\varepsilon(p_{\mathrm{T}})} \times \frac{1}{C(p_{\mathrm{T}})}, \tag{3}$$

where $\gamma_{\mathrm{rec.}}(p_{\mathrm{T}})$ denotes raw photon spectra that is corrected by out-of-bunch pileup effects and secondary photon contributions, $P(p_{\mathrm{T}})$ is the purity of photon sample, $\varepsilon(p_{\mathrm{T}})$ is the reconstruction efficiency, $C(p_{\mathrm{T}})$ is conversion probability. Correction factors are evaluated using Monte Carlo simulations. The purity, the reconstruction efficiency and the conversion probability, which are momentum dependent quantities, are 99 %, 60 % and 8 % at 1 GeV/c respectively. Figure 1 shows inclusive photon spectrum.

Decay photon spectra $\gamma_{\mathrm{dec}}(p_{\mathrm{T}})$ is obtained based on a particle decay simulation called "cocktail". The step is as follows: first we measure π^0 and η spectra in p-Pb collisions, and then, the spectra are fitted with a Modified Hagedorn function [9]. Since other hadrons such as η', ω, ρ, ϕ are not measured, m_{T} scaled function to π^0 spectrum is employed. For the scaling, normalization factor ($\eta' = 0.4$, $\omega = 0.85$, $\rho = 1$, $\phi = 0.13$) is applied. Then all particles are generated and decay into photons using Pythia decayer. Figure 2 shows source of decay photon spectra. Figure 3 shows relative decay photon fraction to the total photon yield.

To obtain direct photon excess ratio R_γ, we calculate double ratio as follows:

$$R_\gamma = \left(\frac{\gamma_{\mathrm{incl}}}{\pi^0}\right)_{\mathrm{meas}} \Bigg/ \left(\frac{\gamma_{\mathrm{decay}}}{\pi^0}\right)_{\mathrm{sim}}, \tag{4}$$

where the numerator denotes measured inclusive photon yield over neutral pion yield, and the denominator is constructed in the same way but photon yield obtained by decay photon simulation and parametrization of the neutral pion yield. The advantage of using double ratio is cancellation of common systematic uncertainties such as material budget and photon reconstruction. Figure 4 shows γ/π^0 ratios mentioned above, black circle points are measured and blue diamond points are calculated from cocktail simulations. As a next step, R_γ will be calculated.

In this report, current status of direct photon measurement in pPb collisions is presented. Currently, systematic uncertainty estimation and systematic checks are ongoing. In parllel, multiplicity dependent analysis is underway.

References

[1] PHENIX collaboration, A. Adare *et al*, Phys. Rev. Lett. 104 (2010) 132301

[2] ALICE collaboration, J. Adam *et al*, Phys. Lett. B754 (2016) 235-248

[3] CMS collaboration, J. High Energy Phys. 09 (2010) 091

[4] CMS collaboration, Phys. Lett. B718 (2013) 795

[5] C. Shen *et al*, Phys. Rev. Lett. 116 (2016) 072301

[6] K. Duslingand *et al*, Phys. Rev. D87. (2013) 054014

[7] M. Bourquiin and J. M. Gaillard, Nucl. Phys. B114 (1976) 334-364

[8] B. B Abelev *et al*, Int. J. Mod. Phys. A 29 (2014)

[9] PHENIX collaboration, A. Adare *et al*, Phys. Rev. C81. (2010) 034911

Accelerator and Instrumentation

High-resolution spectroscopy at OEDO-SHARAQ

S. Michimasa, M. Dozono, J.W. Hwang, S. Ota, N. Imai, K. Yako, and S. Shimoura

Center for Nuclear Study, Graduate School of Science, University of Tokyo

The Optimized Energy Degrading Optics for radioactive ion beams (OEDO) system [1] was constructed in 2017, and successfully demonstrated RI beam productions with slow-down scheme from $\sim$ 200 MeV/u down to 15–50 MeV/u. The starting point of the OEDO system was an upgrade of the High-Resolution Beamline (HRB) [2] and the Spectroscopy with High-resolution Analyzer of RadioActive Quantum beams (SHARAQ) spectrometer [3] for opening up new possibilities in nuclear experimental studies with low-energy RI beams. The idea of OEDO is to manipulate a degree-of-freedom in the longitudinal phase space of RI beam. To obtain a beam with a small spot size and a small energy spread, the OEDO system transforms the spreads of horizontal position and angle of the beam to the timing spread, which corresponds to the rotation of the phase space ellipse on the position- (angle-) timing plane to obtain a small position (angle) spread. In the commissioning and physics experiments, the new beamline with OEDO system has exercised the performance well. The achievements were reported recently in the refereed articles [1, 4].

While at the same time, the high-resolution RI spectroscopy at 100–300 MeV/u is still an attractive performance of the SHARAQ spectrometer. Practically, because several beamline magnets were rearranged in the construction of the OEDO beamline, the performance of the high-resolution RI spectroscopy at the OEDO+SHARAQ scheme should be checked for future high-resolution experimental studies. This report describes applicability evaluation of such high-resolution studies at OEDO.

In upgrade from HRB to OEDO, we carefully studied the compatibility between the high-resolution and energy-degradation performances. Figure 1 shows a list of magnet arrangements for HRB or OEDO beamline, where the boxes with "STQ," "D," and without labeling indicate a Superconducting Triplet Quadrupole magnet, a Dipole magnet and a normal-conducting quadrupole magnet, respectively. The wiring with two magnets means that these magnets are controlled by a power supply. The arrangement

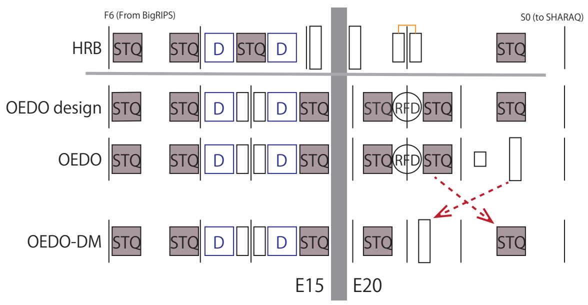

Figure 1. Magnet arrangements for the HRB or OEDO beamline. Details are written in the text.

labeled by "HRB" is the original before OEDO. "OEDO design" is the proposed configuration at the OEDO planning, described in Ref. [5]; "OEDO" is the present magnet configuration where the commissioning and previous experiments were done. The present OEDO beamline could not satisfy the designed compatibility due to insufficient performances of quadrupole magnets. Thus, we found a solution to obtain the compatibility by minimum re-arrangements of quadrupole magnets. The "OEDO-DM" in Fig. 1 is a new magnet configuration of the OEDO beamline for high-resolution spectroscopy. The relocation of magnetic elements from OEDO to OEDO-DM is indicated by the dotted arrows. An important advantage of the OEDO-DM is that the rearrangement of magnets is completed in the E20 experimental room. Accordingly, the change can be even possible during the irradiation beam time to the other experimental areas in RIBF.

The dispersion matching ion optics in BigRIPS-OEDO-SHARAQ scheme is shown in Fig. 2. The ion trajectories in the figure show the results of the first-order calculation. The beam parameters at F3 is assumed to be 3 mm of horizontal spot size (x), 10 mr of horizontal outgoing angle (a), 3 mm of vertical spot size (y), 30 mr of vertical outgoing angle (b), and 0.3% of momentum spread (δ_p). The magnet settings for this mode were the same between F3 and FE7, while modified between FE7 to S0. The setting of SHARAQ spectrometer is similar to the previous setting for the SHARAQ03 experiment [6]. The S0 and S2 are the secondary target position and the final focal plane of the SHARAQ spectrometer, respectively. The ion optics between FE7 and S0 were modified under conditions that the transport matrix elements of F3–S0 are similar values in the HRB and OEDO-DM magnet configurations.

Table 1 shows the transport matrix elements calculated based on the HRB and OEDO-DM configurations. The ma-

HRB	$\langle x\|$	$\langle a\|$	$\langle y\|$	$\langle b\|$
$\|x\rangle$	-0.97	+0.27	+0.00	+0.00
$\|a\rangle$	+0.00	-1.04	+0.00	+0.00
$\|y\rangle$	+0.00	+0.00	+1.15	-0.40
$\|b\rangle$	+0.00	+0.00	+0.00	+0.87
$\|\delta_p\rangle$	-14.4	+4.49	+0.00	+0.00
OEDO-DM	$\langle x\|$	$\langle a\|$	$\langle y\|$	$\langle b\|$
$\|x\rangle$	-1.09	+0.26	+0.00	+0.00
$\|a\rangle$	+0.00	-0.92	+0.00	+0.00
$\|y\rangle$	+0.00	+0.00	+2.00	+3.79
$\|b\rangle$	+0.00	+0.00	+0.00	+0.50
$\|\delta_p\rangle$	-14.7	+3.72	+0.00	+0.00

Table 1. Transport matrix elements between F3–S0 calculated based on the HRB and OEDO-DM configurations.

trix elements in a horizontal (vertical) row are concerned to the same final (initial) beam parameters. Comparing the

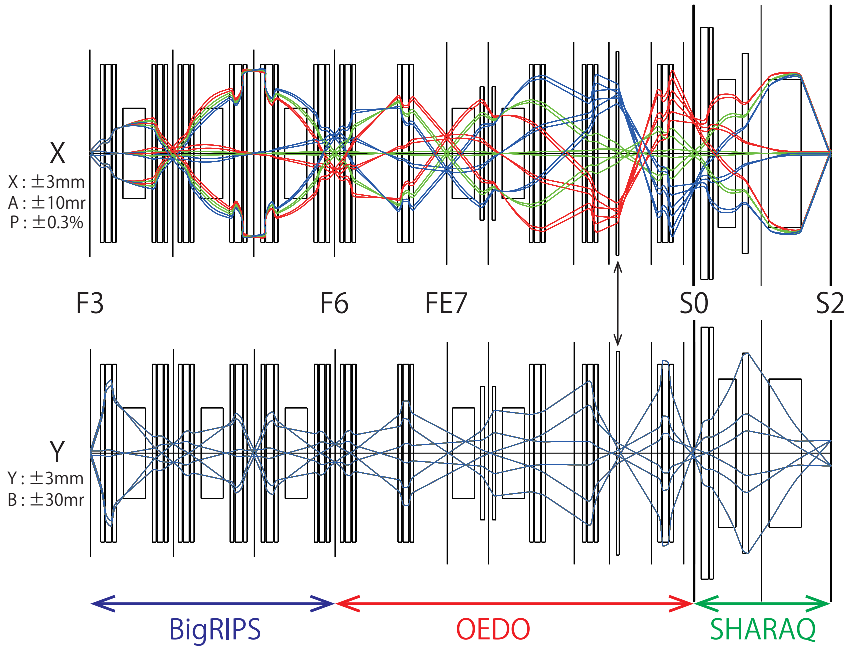

Figure 2. Ion-optical trajectories of the DM mode in BigRIPS-OEDO-SHARAQ scheme.

HRB and OEDO-DM configuration, the corresponding matrix elements are almost identical, therefore the OEDO-DM configuration is able to provide the DM ion optics for high-resolution spectroscopy.

When the OEDO beamline is tuned to compose the ion trajectory shown in Fig. 2, field strengths of the component magnets are set in proportion to the magnetic rigidity of the RI beam and the ratios of the field strengths among the magnets are kept constant. Therefore, the applicable limit of the OEDO-DM transport is determined by a magnet which reaches the performance limit at the lowest magnetic rigidity. The applicable limit of the OEDO-DM transport is 5.3 Tm and is much lower than that of the HRB, which is 8 Tm. Since 5.3 Tm corresponds to 140 MeV/u of triton, a matching with neutron-rich RI beams produced by BigRIPS is practically insufficient. The limit is determined by the magnet indicated by an arrow in Fig. 2, and all of the other magnets are applicable to 8-Tm RI beams. For optimized transportation of 8-Tm beams, the 1.5-times enhancement of the maximum GL of the pointed magnet is necessary. This is critical for high-resolution spectroscopy at OEDO-SHARAQ.

To enhance the performance of the OEDO-SHARAQ system not only in the OEDO mode but also in the OEDO-DM mode, we continue to study possible improvements of the whole system. At present, it is the best possible solution to replace the magnet with limited field into a normal conducting quadrupole magnet with a large bore radius and a stronger magnetic field. We aim at continuous progress of experimental performance of the OEDO-SHARAQ system as well as accelerating various researches in nuclear physics by using the system.

References

[1] S. Michimasa *et al.*, Prog. Theor. Exp. Phys. **2019**, 043D01 (2019).

[2] T. Kawabata *et al.*, Nucl. Istrum. Meth. Phys. Res., Sect. B **266**, 4201 (2008).

[3] T. Uesaka *et al.*, Prog. Theor. Exp. Phys. **2012**, 03C007 (2012).

[4] J. Hwang *et al.*, Prog. Theor. Exp. Phys. **2019**, 043D02 (2019).

[5] S. Michimasa *et al.*, CNS annual report 2014, CNS-REP-93, 47 (2016).

[6] S. Michimasa *et al.*, Phys. Rev. Lett. **121**, 022506 (2018).

Activation measurements of the $^{\mathrm{nat}}\mathrm{Yb}(\alpha,xn)\,^{172,175}\mathrm{Hf}$ reactions toward large-scale production of $^{178\mathrm{m}2}\mathrm{Hf}$

N. Kitamura, N. Imai, H. Haba[a], Y. Yamaguchi, S. Shimoura S. Michimasa

Center for Nuclear Study, Graduate School of Science, University of Tokyo
[a]RIKEN Nishina Center

Nuclear isomers have been identified throughout the nuclear chart [1]. Among them, the second isomeric state of ^{178}Hf located at 2.447 MeV has attracted much attention because of its long half-life (31 y) and high spin ($16\hbar$) [2]. The long lifetime of this isomer allows us to use it for nuclear-reaction studies. In fact, several attempts to fabricate isomer targets have been made so far. More than two decades ago isomer targets were produced at Dubna [3], and intensive studies have been carried out using these targets. It has been possible to study Coulomb excitation, deuteron inelastic, two-neutron transfer, neutron capture, photon- and electron-induced reactions on $^{178\mathrm{m}2}$Hf. In addition to these reactions, the possibility of exploring unique features arising from the nuclear structure of $^{178\mathrm{m}2}$Hf through fusion reactions was proposed [4]. This report focuses on results from the recent development for target fabrication that will enable such reaction studies.

Among several reactions populating $^{178\mathrm{m}2}$Hf, the $^{176}\mathrm{Yb}(\alpha,2n)^{178\mathrm{m}2}\mathrm{Hf}$ fusion-evaporation reaction has been chosen for future large-scale production of $^{178\mathrm{m}2}$Hf as this reaction is reported to have the largest cross section [5]. Prior to the large-scale production, it is desirable to verify the excitation function of $^{176}\mathrm{Yb}(\alpha,2n)^{178\mathrm{m}2}\mathrm{Hf}$ to determine the optimum bombardment energy. Moreover, from a practical point of view, the production cross sections for other radioactive Hf isotopes should be assessed experimentally. This is because the production cross sections are expected to be higher than that of the isomeric state by several orders of magnitude, and the total beam flux could be subject to safety limitations due to their high radioactivities.

An experiment based on the activation method in combination with the stacked-foil technique has been performed at the RI Beam Factory (RIBF), RIKEN. Ten metallic $^{\mathrm{nat}}$Yb foils 99.9 % purity) were prepared for the measurement. The size and thickness of each were respectively 15 mm×15 mm and 17 mg/cm^2. For monitoring the beam energy, the stack of Yb foils was sandwiched by two 0.92-mg/cm^2 thick $^{\mathrm{nat}}$Ti foils. The $^{\mathrm{nat}}\mathrm{Ti}(\alpha,X)^{51}\mathrm{Cr}$ reaction [6] provided an additional beam energy reference for a cross-check purpose. The target stack was tightly attached to a target holder that acts as a Faraday cup to measure the beam current. The AVF cyclotron at RIBF supplied an α beam at 40 MeV with a maximum intensity of 10 μA. The beam passed through thin Be windows and He gas, and finally impinged on the target stack. The gas was continuously flown so that the heat is taken away from the target surface, in addition to the water cooling of the target holder. The target stack was irradiated for eight hours and the total beam flux amounted to 8.5×10^{17} particles, which is equivalent to $2.7\times10^5\,\mu$C. The upstream Ti foil and the first nine layers of Yb adhered to each other due to the heating of the target, and these foils could not be separated after the irradiation. This resulted in two data points of the excitation function. The production cross sections of the main radioactive products of the $^{\mathrm{nat}}\mathrm{Yb}(\alpha,xn)$ reactions, ^{172}Hf and ^{175}Hf, were obtained by measuring γ rays emitted from the irradiated samples using a HPGe detector. As shown in Figure 1, the measured cross sections were compared with excitation functions calculated by TALYS-1.8 [7] and PACE4 [8], showing good agreement with the measurement.

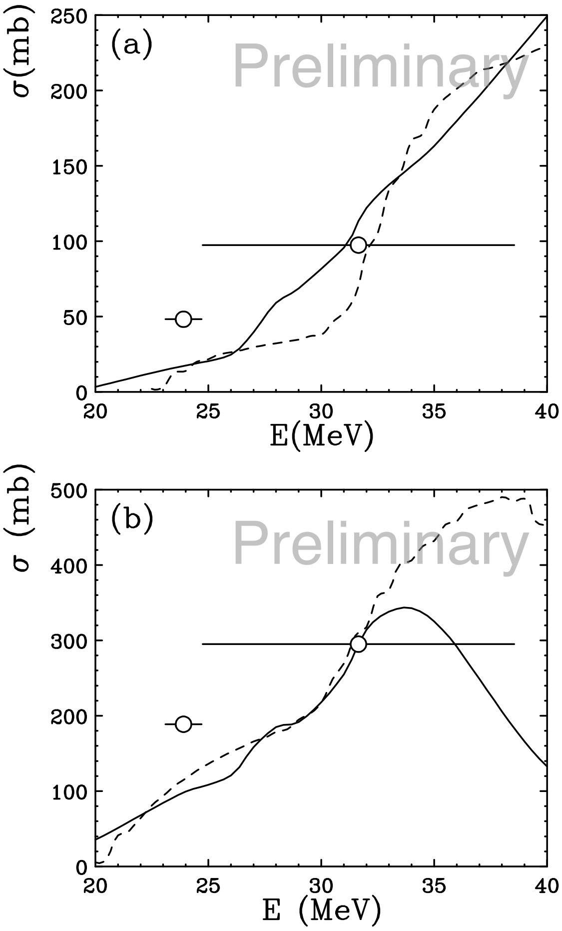

Figure 1. Cross sections of the (a) $^{\mathrm{nat}}\mathrm{Yb}(\alpha,xn)^{172}\mathrm{Hf}$, and (b) $^{\mathrm{nat}}\mathrm{Yb}(\alpha,xn)^{175}\mathrm{Hf}$ rections, in comparison with the calculated excitation functions employing TALYS-1.8 (solid) and PACE4 (dashed). The horizontal error bar denotes the energy loss in the target.

To summarize, we conducted a test experiment toward the large-scale production of $^{178\mathrm{m}2}$Hf. It has been proven that, in combination with the standard activation setup at the

AVF cyclotron facility, the metallic Yb foils can withstand a high-intensity 10 μA alpha beam, without complete melting of the foils or the blister formation on the surface. The production cross sections of the main by-products ^{172,175}Hf were assessed by employing the activation method. A production run with an ^{176}Yb enriched target is currently planned.

References

[1] P. M. Walker and G. D. Dracoulis, Nature **399**, 35 (1999).

[2] R. G. Helmer and C. W. Reich, Nucl. Phys. A **211**, 1 (1973).

[3] Yu. Ts. Oganessian *et al.*, Hyperfine Interact. **107**, 129 (1997).

[4] D. J. Hinde *et al.*, Phys. Rev. C **68**, 044606 (2003).

[5] S. A. Karamian, Yad. Fiz. **68**, 1827 (2005).

[6] "Charged particle cross-section database for medical radioisotope production: diagnostic radioisotopes and monitor reactions", IAEA-TECDOC-1211, Vienna (2001).

[7] TALYS-1.8, http://www.talys.eu/.

[8] O. B. Tarasov and D. Bazin, Nucl. Instrum. Methods Phys. Res. B **266**, 4657 (2008); A. Gavron, Phys. Rev. C **21**, 230 (1980).

Development of a self-supporting large area titanium-deuteride target

K. Wimmer[1a], N. Imai [2], Y. Hatano[b], J. Wang[b], D. Sekiba[c], Y. Sugisawa[c]

Center for Nuclear Study, Graduate School of Science, University of Tokyo
[a]Department of Physics, Univ. of Tokyo
[b]Hydrogen Isotope Research Center, Univ. of Toyama
[c]Graduate School of Pure and Applied Sciences, Univ. of Tsukuba

For future experiments looking for shape coexistence in atomic nuclei and BCS-BEC cross-over phenomenon of neutron pairing predicted in very neutron-rich nuclei, the development of a tritium-loaded titanium (Ti^3H) target has been initiated in collaboration with the Hydrogen Isotope Research Center at the University of Toyama. For the planed future experiments at OEDO, neutron-rich Ni and Sn will be impinging on Ti^3H target at Coulomb barrier energies. This requires a rather large target area of 3×3 cm^2 and a high $^3H/Ti$ ratio.

In order to develop and test the fabrication procedure for such a large, self-supporting target with a high hydrogen concentration, prototypes with deuterium have been fabricated. In order to avoid mechanical deformation, the 3 μm thick Ti foils were sandwiched between two porous Al_2O_3 plates. Under vacuum, the samples were heated to $\approx 500°$ C and then exposed to a deuteron gas atmosphere. Then the temperature was gradually decreased and the deuterium gas was absorbed into the Ti matrix, partially converting it to titanium-deuteride.

A first batch of 2×2 cm^2 prototype targets was produced under various temperature, time, and pressure conditions, and a measurement using the $d(^{12}C,d)$ elastic scattering reaction at 20 MeV beam energy at Kyushu University [1] was performed. The analysis of the data showed that the deuterium loading ratios varied in the different samples.

Within the OEDO commissioning it turned out that the beam spot is larger than anticipated, therefore in 2018 3×3 cm^2 target were made. Based on the experience from the first series, the temperature, time, and pressure conditions were optimized. Fig. 2 shows some of the TiD foils that were produced at the University of Toyama. By monitoring the pressure decrease a constant temperature the loading ratio was obtained to be around 0.7. Even by increasing the initial deuterium gas pressure a maximum of $^2H/Ti = 1.0$ was reached. Instead of porous Al_2O_3 plates a Ni mesh was used to eliminate the possibility that the ceramic inhibits the absorption.

In order to verify the production success and measure the deuterium content of the targets, the elastic recoil detection analysis (ERDA) method was employed. A ^{4}He beam of 2.5 MeV at Tandem accelerator facility in University of Tsukuba was elastically scattered of the DTi foils. Figure 1 shows the energy spectra of elastically scattered deuterons at 30°.

The peak-like structures around channel 250 correspond to the resonance of ^{4}He and d at 2.3 MeV. The yield above channel 300 was used to evaluate the concentration ratio. In addition, Rutherford back-scattering was measured to determine the amount of Ti. The resulting concentration ratio was $^2H/Ti \approx 0.6$ for the three targets tested. This is consistent with the values determined from the final gas pressure. A more detailed analysis is ongoing. In order to improve the loading ratio, and eventually reach more than 1.0 further tests are needed. One approach focuses on the Ti surface which might be compromised, and the quality of the vacuum before the deuterium gas is introduced to the chamber.

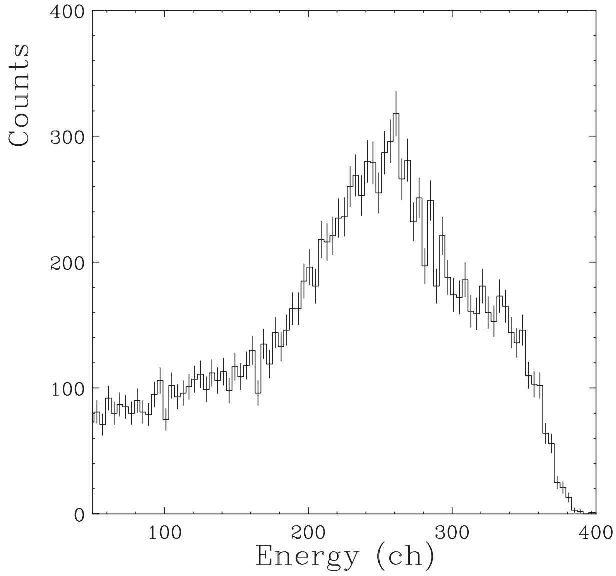

Figure 1. The deuteron energy spectra for a TiD foil.

As a result, the ratio was found to be around 0.6. It is unclear why the concentration ratio was not above 1.0. The surface treatment of the titanium foil may be needed. Further development is ongoing to increase the ratio.

References

[1] K. Wimmer et al., CNS Annual report 2017, p.7.

[1]Present address; CSIC Madrid, Spain
[2]Corresponding author

Figure 2. 3×3 cm^2 and 3 μm thick titanium foils after exposure to deuterium gas.

Track distortion due to ion back flow in CAT-S and correction for the distortion

S. Ota,[a] H. Tokieda,[a] C. Iwamoto,[a] M. Dozono,[a] U. Garg,[b] S. Hayakawa,[a] K. Kawata,[a] N. Kitamura,[a] M. Kobayashi,[a] S. Masuoka,[a] S. Michimasa,[a] A. Obertelli,[c,d] D. Suzuki,[d] R. Yokoyama,[a] J. Zenihiro,[d] R. Kojima,[a] H. Baba,[d] O. Beliuskina,[a] S. Chebotaryov,[d] P. Egelhof,[e] T. Harada,[f] M.N. Harakeh,[g] K. Howard[b] N. Imai,[a] M. Itoh,[h] Y. Kiyokawa,[a] C.S. Lee,[a] Y. Maeda,[i] Y. Matsuda,[h] E. Milman,[d] V. Panin,[d] H. Sakaguchi,[j] P. Schrock,[a] S. Shimoura,[a] L. Stuhl,[d] M. Takaki,[a] K. Taniue,[i] S. Terashima,[k] T. Uesaka,[d] Y.N. Watanabe,[l] K. Wimmer,[a,d,l] K. Yako,[a] Y. Yamaguchi,[a] Z. Yang,[d] and K. Yoneda[d]

[a] *Center for Nuclear Study, the University of Tokyo*
[b] *Department of Physics, University of Notre Dame*
[c] *Le Centre CEA de Saclay*
[d] *RIKEN Nishina Center*
[e] *GSI Helmholtzzentrum für Schwerionenforschung GmbH*
[f] *Department of Physics, Toho University*
[g] *KVI, Center for Advanced Radiation Technology*
[h] *Cyclotron and Radio Isotope Center, Tohoku University*
[i] *Department of Applied Physics, University of Miyazaki*
[j] *Research Center for Nuclear Physics, Osaka University*
[k] *Dept. of Nucl. Sci. and Tech., Beihang University*
[l] *Department of Physics, the Univerisity of Tokyo*

The equation of state (EoS) of nuclear matter not only governs the femto-scale quantum many-body system, namely nuclei, but also plays an important role in the structure of neutron stars and in supernova phenomena. In particular, the EoS of isospin asymmetric nuclear matter has attracted much interest from the viewpoint of the existence of heavy neutron stars. Although the asymmetric term of incompressibility, K_τ, can be a benchmark for various EoSs thanks to the direct accessibility via the measurements of isoscalar giant monopole resonances [1], the ambiguity of the K_τ is still larger than those of other EoS parameters. The measurement of deuterium inelastic scattering of ^{132}Sn was performed at RIBF in RIKEN, aiming at a more precise determination of the K_τ value.

An active target CAT-S [2] has been employed for the measurement of the forward angle scattering, which is sensitive to the monopole transition, together with the backward angle scattering in combination with silicon detectors. A cocktail beam of ^{132}Sn, ^{133}Sb, and ^{134}Te having the total intensity of 3.2×10^5 particles per second bombarded the CAT-S filled with 0.4-atm pure deuterium gas. A set of three 400-μm thick THGEMs is used for the electron multiplication device in TPC of CAT-S. The detail of the measurement was described in ref. [3]. In this paper, we report the observed field distortion due to the injection of the high-intensity heavy-ion beam and its treatment in the tracking procedure.

There is a phenomenon called ion back flow (IBF) where the ions produced in the THGEMs go back to the drift region through the hole of the THGEMs. The drift velocity of the ion is as slow as 0.01 cm/μs and a significant number of ions exist along the beam axis like a wall if the IBF rate is large. Since the geometrical configuration and voltage settings of THGEMs in RIBF113 were not optimized for the reduction of the IBF rate, the effect of space charge due to the ions is observed. The simulation study of the voltage setting for reduction of IBF is separately reported in ref. [4].

This effect on the trajectory of recoil particle is observed in the vertex position dependence of the excitation energy (shown in the right panel of Fig 1), because the position displacement along the beam axis changes the angle of trajectory. A locus around the excitation energy of zero corresponds to elastic scattering. Large deviations at the entrance (Z=-50) and exit (Z=50) are clearly seen. The field distortion is estimated by using the finite element solver (FEniCS project) assuming a certain ion density along the beam axis in the active volume. The resultant position displacement between the electron generated point and the observed point are estimated by the simulation of electron transportation taking the estimated field distortion into account. The detail of the electron trajectory simulation is reported in ref. [5]. Left panel of Fig. 1 shows the result with taking the position displacement into account in tracking procedure. In this procedure, an IBF rate of 32% is assumed. Now the locus of elastic scattering becomes straight and the effect of the IBF is compensated. The best estimator of the IBF rate can be obtained by comparing the widths of elastic peaks assuming various IBF rates.

The excitation energy with beam particle identification is obtained and significant statistics is observed in the GMR energy region in excitation energy spectrum of each isotope. The analysis to finalize the excitation energy spectra at for-

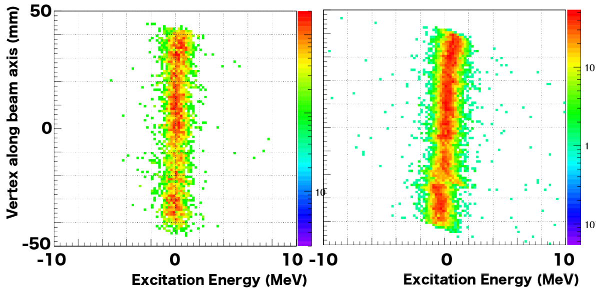

Figure 1. Corrected (left) and uncorrected (right) correlation

ward angle is ongoing and the further analysis for backward angle will be performed.

References

[1] T. Li *et al.*, Phys. Rev. Lett. **99**, 162503 (2007).
[2] S. Ota *et al.*, J. Radioanal. Nucl. Chem. **305**, 907-911 (2015).
[3] S. Ota *et al.*, CNS Annual Report 2016 (2018) 19-20
[4] N. Zhang *et al.*, CNS Annual Report 2018 (2019).
[5] R. Kojima *et al.*, CNS Annual Report 2018 (2019).

Dual gain multi-layer thick GEM with high-intensity heavy-ion beams in low-pressure hydrogen gas

C. Iwamoto, S. Ota, R. Kojima, H. Tokieda, S. Hayakawa, Y. Mizoi[a], T. Gunji, H. Yamaguchi, N. Imai, M. Dozono, R. Nakajima, O. Beliuskina, S. Michimasa, R. Yokoyama, K. Kawata, D. Suzuki[b], T. Isobe[b], J. Zenihiro[b], Y. Matsuda[c], J. Okamoto[c], T. Murakami[d], and E. Takada[e]

Center for Nuclear Study, Graduate School of Science, University of Tokyo
[a]Osaka Electro-Communication University
[b]RIKEN Nishina Center
[c]Cyclotron Radioisotope Center, Tohoku University
[d]Department of Physics, Kyoto University
[e]National Institutes for Quantum and Radiological Science and Technology

We are developing a gaseous active target CAT-M based on a time projection chamber with using GEMs for the study of unstable nuclei using missing mass spectroscopy [1]. CAT-M employs a GEM called dual-gain multi-layer thick GEM (DG-M-THGEM) [2] which has two characteristic structures. First, electrodes of the GEM are separated to control the gain at each segment independently. The GEM is called as dual-gain thick GEM (DG-THGEM). The DG-THGEM can reduce the number of secondary electrons by controlling the gain of a region which measures beams to be low gain even if high intensity beams is injected [3]. An active target CAT-S have been operated successfully by using the DG-THGEMs in a physics experiment of a deuteron inelastic scattering with the high intensity ^{132}Sn beam of several 10^5 Hz [4]. Second is a structure of alternating layers of electrodes and insulators, which was developed by Cortesi as multi-layer thick GEM (M-THGEM) [5]. Because the total thickness of the M-THGEM become thick, the structure is expected to result in a minimal amount of the bending even by mounting without tension and support. In this paper, performance of the prototype DG-M-THGEM with an active area of 10×10 cm^2 was investigated with a high intensity heavy ion beam up to 10^6 Hz. Effect of space charges due to ion backflow from the GEM with the high intensity beam was also considered.

The performance of the prototype DG-M-THGEM with high intensity heavy-ion beam was evaluated by employing the active target CAT-S filled with hydrogen gas at the pressure of 40 kPa. A ^{132}Xe beam with the energy of 185 MeV/u was impinged into CAT-S at a synchrotron accelerator facility HIMAC of National Institutes for Quantum and Radiological Science and Technology.

The effective gas gain for the beam was measured with the low-intensity beam of 5 k particle per pulse. The potential differences among the electrodes in the beam region were changed while those in the recoil region were fixed at the effective gain of about 2000. Figure 1 shows the result of the effective gas gain as a function of the reduced bias in the GEM holes. The effective gas gain G_{eff} is defined as ratio of the amplified charges to the initial charge,

$$G_{eff} = \frac{Q}{e \cdot \Delta E / W} \tag{1}$$

where Q is the collected charges on the readout pad, ■E is the energy deposit of the incident particles above the readout pad, W = 36.5 eV [6] is the mean energy for ion-electron pair creation of the H_2 gas and e is the elementary charge. The gain lower than 100 can be achieved in the beam region with any high voltage setting while the gain of the recoil region was kept the value of about 2000. According to comparison between the open squares and the solid circles, the effective gain measured during beam injection does not seem different from the one without the beam.

Charge resolutions were also measured by changing the setting of the potential differences of the DG-M-THGEM. In order to evaluate the charge resolution, groups consisting of 4 pads were defined as shown in Fig. 2 (a), where the axes of x and z are defined as the direction perpendicular and parallel with the beam axis, respectively. In the figure, 4 hatched red triangles, open green triangles, solid blue triangles are one group to sum up the collected charges defined as variables of Q_{i-1}, Q_i and Q_{i+1}, respectively. The sum of the collected charges of a specific group is almost same with the average value of the collected charges of neighboring groups because the range of the beam is long enough and the energy deposit varies linearly in the active region. Thus a residual of the total charge of the specific group from the average of the total charge of neighboring groups should become almost zero. Here a charge resolution in each group was defined as the standard deviation of the residual distribution which is explained as following equation.

$$\varepsilon = Q_i - \frac{(Q_{i-1} + Q_{i+1})}{2} \tag{2}$$

A dependence of the charge resolutions on the effective gas gain is shown in Fig. 2 (b). The charge resolutions significantly depended on the gain value regardless of the setting to supply voltage to the electrodes. The result indicates that the charge resolution mainly depends on the effective gas gain and independent of the electric field strength in individual region of the GEM.

Beam intensity dependence of the measured charges were studied by investigating position dependence of the energy deposit along the beam axis. Figure 3 shows the measured energy deposit in the each pad group defined as Fig. 2 (a). The energy deposits with the low intensity beam

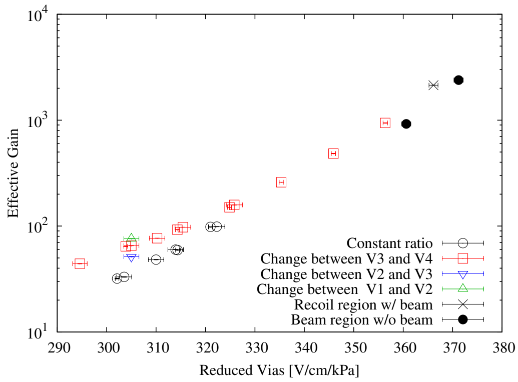

Figure 1. The gain curve as a function of the reduced bias by using the ^{132}Xe beam with the low-intensity of 5 k particles per pulse. Open circles, squares and triangles are the gain of the beam region measured with the beam. The open circles are the data that the ratio among the potential differences between V_1 and V_2, V_2 and V_3, and V_3 and V_4 was kept constant. Open squares are the data that the only potential difference between the electrode V_3 and $V_4$was changed. Open inverted triangle is the data that the only potential difference between the electrode V_2 and V_3 was changed. Open triangle is the data that the only potential difference between the electrode V_1 and V_2 was changed. Cross mark is the gain of the recoil region measured with the alpha particles while the beam passed in the beam region which had the gain of about 100. Solid circles are the gain of the beam region measured with the alpha particles when the beam was off.

of 1.2 kHz are almost constant. On the other hand, the energy deposits with 1 MHz beam intensity are 4 % larger than that of the intensity of 1.2 kHz at the center position at z = 0 mm and becomes even larger for positions farther from the center. Assuming the effective gain is constant to the increase of the beam intensity, the reason for this phenomenon can be explained as the effect of space charges in the drift region along to the beam axis. The space charges attracted electrons produced outside of the active region. The attracted electrons were collected by the readout pads around the edge of the active area. Such as the measured electrons around the edge increase with higher space charge density due to the high intensity beam. Development to reduce the ion back flow and keep the strength distribution of the electric field uniform is ongoing.

References

[1] S. Ota *et al.*, CNS Annual Report **2016** CNS-REP-96, 49 (2017).

[2] C. Iwamoto *et al.*, CNS Annual Report **2016** CNS-REP-96, 51 (2017).

[3] S. Ota *et al.*, Journal of Radioanalytical and Nuclear Chemistry, **305**, 907-911(2015).

[4] S. Ota *et al.*, CNS Annual Report **2016** CNS-REP-96,19 (2017).

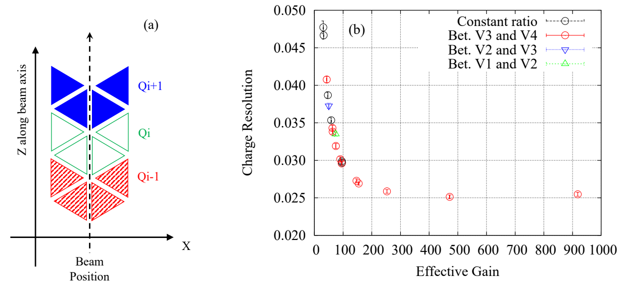

Figure 2. (a) The definition of the pad groups to evaluate the charge resolutions with the equation (2). 4 triangles are one group at each low to obtain the collected charges Q_{i-1}, Q_i and Q_{i+1}, respectively. (b) The Charge resolution as a function of the effective gas gain. Legends are the same with figure 1.

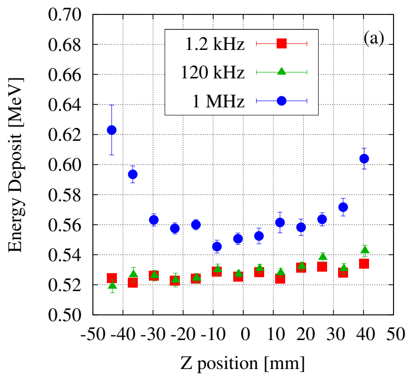

Figure 3. Position dependence of the energy deposit along to the beam axis by changing the beam intensity.

[5] M. Cortesi *et al.*, Review of Scientific Instruments **88**, 013303 (2017).

[6] C. Simon Wedlund *et al.*, Ann. Geophys., **29**, 187 - 195 (2011).

Effect of Ion Back-flow on electron trajectory in drift field of CAT

R. Kojima and S. Ota

Center for Nuclear Study, Graduate School of Science, The University of Tokyo

A series of active targets named CAT-S [1] and CAT-M [2] have been developed in CNS for the purpose of the missing mass spectroscopy in inverse kinematics. Each CAT consists of a time-projection chamber (TPC) and an array of silicon detectors. In an active volume of the TPC, beam and target nuclei react. The trajectories including the ranges of low-energy particles and the vertex of the reaction are reconstructed, which enables us to measure inelastic scattering at very forward angles, for example, ^{132}Sn(d,d') [3] and ^{136}Xe(p,p') [4] scatterings. In the TPC, some part of ions generated at the electron amplification part come back into the active area. Such an ion current is called Ion Back-Flow (IBF). When the total amount of IBF becomes large, it causes a non uniformity of the electric field and modifies the electron trajectory. Thus, in the high-rate beam experiments with a beam intensity around one million particles per second, the tracking performance is affected by IBF. In order to evaluate this effect, we have simulated the electric field induced by IBF and the electron trajectory distortion at the condition of the experiment in ref. [3]. In this report, we present the simulation result.

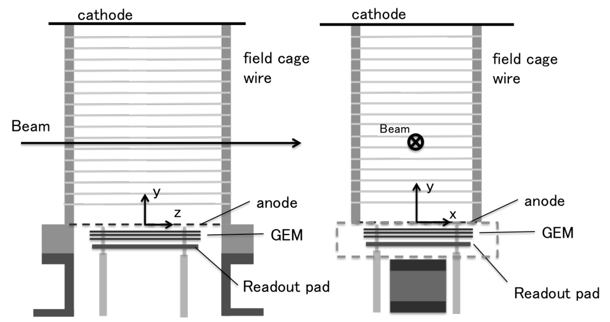

Figure 1. Schematic layout of TPC of CAT-S.

Figure 1 shows a schematic layout of TPC of CAT-S. The TPC has a box-shaped field cage, a cathode plate and an anode mesh 25 cm below the cathode. The inner size of the field cage is $11\times\ 25\ \times\ 23$ cm^3. The top layer of three DG-THGEMs [1] locates 7 mm below the anode followed by a readout pad. Beam and recoil particles traveling in the active area generate electron-ion pairs along their paths. The primary ions are guided towards the cathode along an uniform electric field generated by the field cage. The primary electrons, on the other hand, travel to the opposite direction and collected into DG-THGEM holes. They make avalanches in the holes due to the strong electric field applied to DG-THGEM. The amplified electrons are then detected by the readout pad to provide the projection of particle paths on the readout pad. The ions produced in the avalanche process partly go into the active area through the holes. Due to the small mobility of ion in a gas, they are accumulated in the active area during the measurement. Because the energy loss of the beam is much bigger than that of recoil particles, IBF concentrates in the beam region inside the field cage even though the amplification in the beam region is reduced to about one-tenth of that in the recoil region. Thus we only consider IBF in the beam region for the simulation of electric field. For the simplicity of calculation, the following assumptions are made,

Table 1. Parameters of the space charge simulation.

Target gas	Deuterium	
Gas pressure		40 kPa
Typical Beam Rate	R_{beam}	350 kpps
Energy loss per meter	E_{loss}	100 MeV/m
Energy per ion pair	W	37 eV
Nominal drift field	E_{cage}	-400 V/cm
Ion drift velocity [7]	v_{ion}	$\sim$10.2 cm/msec
Electron drift velocity	v_D	$\sim$1.02 cm/μsec
Active area volume		$11\times25\ \times23$ cm^3
DG-THGEM size		10×10 cm^2
Beam spot size	d_x	2 cm
IBF efficiency	ε_{ion}	32

- Constant beam rate : R_{beam}.
- Homogeneous beam distribution.
- Constant energy loss per unit length : E_{loss}.
- Electric field between ions can be neglected.
- Diffusion-less motion of ion.

Moreover, we ignore the primary ions as we assume the number of ions immigrating to the active area per one primary electron ε_{ion} is much larger than 1. As a consequence of these assumptions, the space charge generated by IBF can be considered as an ion column with a constant density ρ_{ion}. The area of ion column is shown in Fig. 2. The density of ions is given as,

$$\rho_{ion} = e\cdot\varepsilon_{ion}\cdot\frac{R_{beam}}{d_x}\cdot\frac{E_{loss}}{W}\cdot\frac{1}{v_{ion}}, \tag{1}$$

where e is the elementary electric charge, W is the average energy to create one electron-ion pair and v_{ion} is an ion drift velocity. With the parameters for our experiment summarized in Table 1, the ion density becomes $\rho_{ion} = 2.38\times10^{-6}$ C/m^3. ε_{ion} is estimated from IBF simulation using Garfield [5] for this configuration. The electrostatic potential ϕ generated by this ion density distribution can be obtained by solving Poisson's equation:

$$\Delta\phi = -\frac{1}{\varepsilon_0}\rho_{ion}(x,y,z). \tag{2}$$

Using a finite element solver FEniCS [6], this partial differential equation is solved numerically. Dirichlet boundary condition $\phi = 0$ is entailed at the positions of field cage wires, the cathode and the anode. Electric field $\mathbf{E}$ caused by the ions is finally deduced from the gradient of the resulting potential. Figure 2 depicts the electric field components, E_z along beam direction , E_y along drift direction and E_x at the entrance of DG-THGEM ($z = -50$ mm). Electron trajectory distortion is evaluated by tracking electron motions in this field. The nominal drift field $E_{cage} = -400$ V/cm is superimposed on E_y for this purpose.

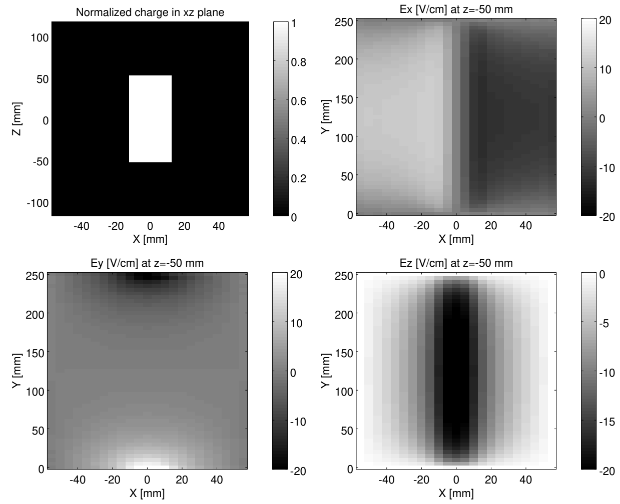

Figure 2. The space charge distribution normalized to 1 in x-z plane (upper left), calculated electric field of E_x (upper right), E_y (lower left) and E_z (lower right) in x-y plane at the entrance of DG-THGEM ($z = -50$ mm) with an ion density of $\rho_{ion} = 2.38 \times 10^{-6}$ C/m^3.

The electron motion in a gas media is governed by Langevin equation :

$$m\frac{d\mathbf{v}}{dt} = e\mathbf{E} - \frac{\mathbf{m}}{\tau}\mathbf{v}, \tag{3}$$

where $\mathbf{v}$ is the drift velocity and τ is the mean time between collisions with gas. The last term in the equation represents the stopping force due to the collision, which depends on the drift velocity and time between collisions. The drift velocity will be saturated, namely the righthand side of Eq.(3) equals 0. In that case, a steady flow is achieved. Thus the solution is given by,

$$e\mathbf{E} = \frac{\mathbf{m}}{\tau}\mathbf{v_D}. \tag{4}$$

From this equation we can find that, in macroscopic view, the electrons move along the electric field with a drift velocity defined by the local electric field. Rewriting Eq.(4), the drift velocity is given as $\mathbf{v_D} = \mu\mathbf{E}$, where μ is the electron mobility in a gas. We calculate μ for deuterium gas in various electric field strengths by Magboltz [8]. Using the relation between the drift velocity and the electric field strength, and the three dimensional electric field map calculated by FEniCS, we track the electron positions with a fourth order

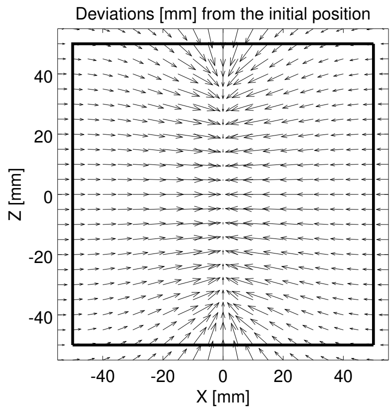

Figure 3. Deviation of electron trajectory in x-z plane starting from 5 mm grid at the beam line ($y = 48$ mm) with ε_{ion}= 32, magnified by 4 for easy viewing. The square indicates the position of DG-THGEM.

Runge-kutta algorithm with a time interval of 5 nsec, which corresponds to about 50 μm in length. Figure 3 shows the distortion of electron trajectory starting from 5 mm mesh grid in x-z plane at the beam line ($y = 48$ mm). Trajectory distortion is defined as a position difference between the initial and the final positions on the anode mesh in x-z plane denoted by δ_x and δ_z. The arrows in the figure indicate the direction and the length of distortion as $\sqrt{\delta_x^2 + \delta_z^2}$, which are magnified by 4 for easy viewing. One can see that the electrons are attracted towards the ion column in the beam region.

This simulation result is implemented into the tracking procedure of data analysis to correct the IBF effect. The details of correction is reported in ref. [9] .

References

[1] S. Ota *et al.*, J. Radiational. Nucl. Chem. **305**, 907-9011(2015).

[2] S. Ota *et al.*, CNS Annual Report 2016, CNS-REP-96, 51-52 (2018) .

[3] S. Ota *et al.*, CNS Annual Report 2016, CNS-REP-96, 19-20 (2018).

[4] C. Iwamoto *et al.*, CNS Annual Report 2017, CNS-REP-97, 17-18 (2019).

[5] R. Veenhof, Garfield, http://cern.ch/garfield

[6] A. Logg *et al.*, Automated Solution of Differential Equations by the Finite Element Method, Springer, 2012.

[7] G. Sinnott, Phys. Rev. Lett. **136**, A370 (1964).

[8] S.F. Biagi, Magboltz, http://magboltz.web.cern.ch/magboltz

[9] S. Ota *et al.*, CNS Annual Report 2018 (2019).

Development of Gamma-ray Tracking Detector and its performance test

A. Kohda[a], Y. Yamamoto[a], N. Aoi[a], E. Ideguchi[a], M. Kumar Raju[a], H.T. Hoang[a], T.T. Pham[a], T. Shima[a], S. Miyamoto[b], T. Shizuma[c], N. Imai[d], J.W. Hwang[d], K. Wimmer[e], P. Doornenbal[f], and M.L. Cortes[f]

[a]*Research Center for Nuclear Physics (RCNP), Osaka University*
[b]*Laboratory of Advanced Science and Technology for Industry (LASTI), University of Hyogo*
[c]*National Institutes for Quantum and Radiological Science and Technology (QST)*
[d]*Center for Nuclear Study (CNS), University of Tokyo*
[e]*Department of Physics, The University of Tokyo*
[f]*RIKEN Nishina Center for Accelerator-Based Science*

We evaluated the performance of the Gamma-ray Tracking Detector at NewSUBARU facility by using gamma ray beam from GACKO beam line.

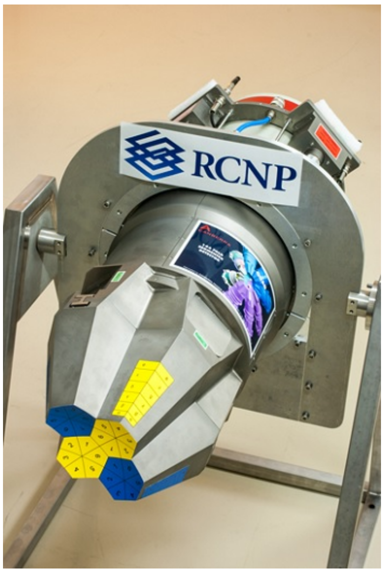

Figure 1. Gamma-ray Tracking Detector of RCNP

The Gamma-ray Tracking Detector [1] is a Ge detector realizing both high efficiency and Compton background suppression by reconstructing the scattering process of the incident gamma-rays from the positions and energy deposits of the gamma-rays at each interaction points in the detector. Its high position resolution is also beneficial for accurate Doppler correction. In the tracking detector, the interaction positions are determined three-dimensionally with high resolution by analyzing the waveform of the signal from the segmented electrodes.

Our Gamma-ray Tracking Detector is a GRETINA [2] type detector. This is the first gamma-ray tracking detector to be started developing in Japan.

The interaction points are obtained by waveform analysis. Here, a method is used to find the most similar waveform by comparing with the theoretically calculated waveform at each position.

We mesured position resolution, not only the "Precision σ", the spread of the interaction point distribution, but also the "Accuracy δ", difference with the real interaction position.

We evaluated the performance of the position resolution using colimated gamma-ray beam at NewSUBARU [3]. In this experiment, we used 3.9 MeV gamma ray beam obtained by collision between 1.5 GeV electron and CO_2 laser. We can obtain high intensity gamma ray beam with the intensity of 10^5 cps with 2 mm diametor, and it is about 200 times stronger than when we used a 10 MBq ^{137}Cs source.

We did two types of experiments, Pencil beam measurement and Coincidence measurement. In pencil beam measurements, we can check the linear distribution of interaction points obtained by irradiating collimated gamma rays on the detector.

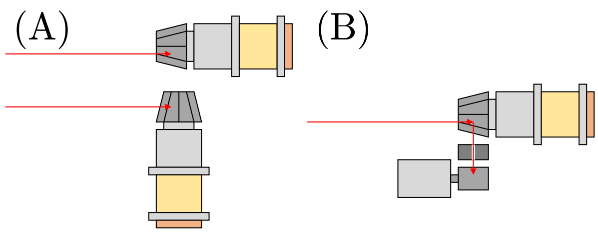

Figure 2. Pencil beam measurement (A) and coincidence measurement (B)

The result of pencil beam measurement which is distribution of interaction positions reproduced by waveform analysis is shown in Fig. 3. The red band in the figure is the position of the beamline determined by photogrammetry, and the width of the band represents the error (including the size of the beam itself).

From this result, the size of the spread of the interaction point distribution is taken as the accuracy σ and the difference between the beamline position obtained by photogrammetry and the central value of the distribution is taken as the accuracy δ, these are, $(\sigma_x, \sigma_y) = (1.07(24), 1.00(22))$ mm, $(\delta_x, \delta_y) = (1.66(71), 1.15(75))$ mm.

In order to confirm the correctness of the position analysis, we also performed a coincidence measurement. In coincidence measurement, a Pb slit is placed beside the detector on the beam line, and another gamma ray detector (CNS-GRAPE [4]) is placed behind it. As a result, only events scattered 90 degrees at a limited point in the detec-

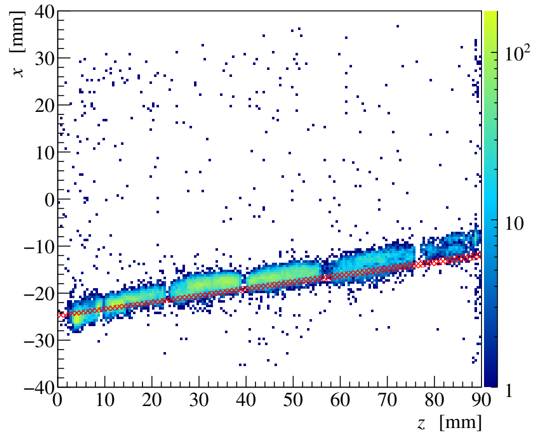

Figure 3. Interaction position distribution in Ge crystal from pencil beam measurement. This is a projection onto the x - z plane. The interaction positions are reproduced by waveform analysis. Red band is real interaction position obtained by photogrammetry.

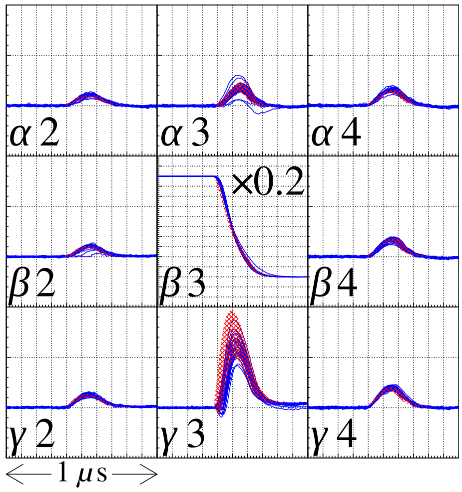

Figure 4. Waveform from Coincidence measurement is shown by blue line. $\alpha 2$, $\alpha 3$ ... etc. are electrode ID. Greek letters part means axial direction, number part means circumferential direction. $\beta 3$ is the electrode where the charge is absorbed and it means that an interaction has occurred in the area. Red band is calculated waveform at real interaction position.

tor is simultaneously counted with the detector, so we can check the output waveform at a particular interaction point.

The waveform obtained as a result of the coincidence measurement is shown in Fig. 4. The red band shown in the figure is the calculated waveform at the interaction position determined by photogrammetry. This figure shows that the calculated waveform and the actual waveform match fairly well.

In the analyzed result, only δ_x showed a particularly large value. One of the possible reasons for this is when the precision is actually low. Even when interaction actually occurs at that position, different waveforms from calculation may be output. Because we use hypothetical values in calculating the waveform on each position such as the impurity concentration of the crystal that can not actually be confilmed. The other is when the photogrammetry used as the “real position” is wrong. (for example, if the shape of the detector is different from the design drawing.)

From this analyzed result, we found that this detector has good enough accuracy for tracking. But also has a problem with the precision of the reproduced interaction point distribution that seems to be due to the uncertainty of the calculated waveform compared with the actual waveform. We can improve tracking performance by improving this from now on. For that purpose, it can be realized by optimizing the calculated waveform by examining the waveform features and trends at specific interaction points.

References

[1] I.Y. Lee, Nucl. Instr. Meth. Phys. Res. A **422**, 195 (1999)

[2] S. Paschalis *et al.*, Nucl. Instr. Meth. Phys. Res. A **709**, 44 (2013)

[3] H. Utsunomiya *et al.*, Nucl. Phys. News **25**, 3, 25 (2015)

[4] S. Shimoura, Nucl. Instr. Meth. Phys. Res. A **525**, 188 (2004)

Improvement of the pepper-pot emittance monitor

Y. Kotaka, Y. Ohshiro, H. Yamaguchi, N. Imai, Y. Sakemi, T. Nagatomo[a], T. Nakagawa[a], J. Ohnishi[a], A. Goto[a], M. Kase[a], K. Hatanaka[b], H. Muto[c], and S. Shimoura

Center for Nuclear Study, the University of Tokyo
[a]Riken Nishina Center
[b]Research Center for Nuclear Physics, Osaka University
[c]Suwa University of Science

1. Introduction

For the purpose of increasing the beam intensity of AVF cyclotron, it is necessary to optimize the beam injection system. Therefore we have developed a pepper-pot emittance monitor [1] (PEM_IH10) and a beam-orbit calculation method by using the 4D emittance measured with PEM_IH10 [2] as initial value. For the performance evaluation, the results of beam-orbit calculations were compared with the measurement of other beam diagnostics. The conformity was quantified by χ^2/DOF, but its relative number is adjusted to 1 when the results of beam-orbit calculations agree with the measurement of other beam diagnostics by visual judgement. In comparison with 15 kinds of measured 2D emittances, the conformities were within 6. [3]

This fiscal year, we improved beam detection part of PEM_IH10 in order to reduce the conformity. The improvement of the camera lens system and the image processing did not improve the conformity but the position accuracy. Meanwhile, it has been found that the thickness of fluorescent agent affects the conformity.

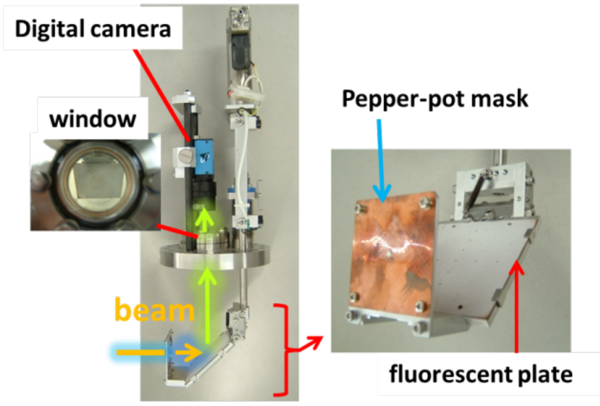

Figure 2. The schematic view of our PEM_IH10. It is composed of pepper-pot mask and fluorescent plate. Pepper-pot mask has 0.3 mm diameter holes opened at 3 mm interval. Fluorescent plate tilted by 45 degrees functions as a beam position detector passing through the pepper-pot mask. The light emitted by fluorescent plate in the region where beam hits is recorded by a digital camera set perpendicular to the beam axis.

2. Alignment improvement of PEM_IH10

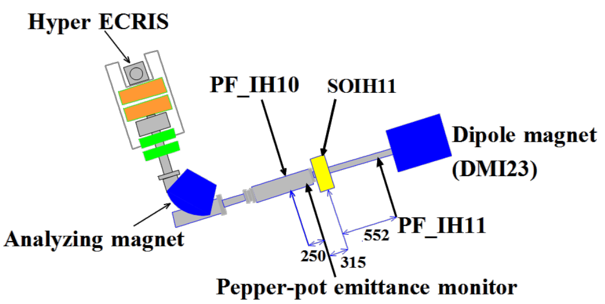

Figure 1. The top view of a part of beam injection line from Hyper ECRIS to dipole magnet (DMI23).

For the alignment of PEM_IH10, another beam profile monitor (PF_IH11) was installed 867 mm behind PEM_IH10 as shown in Fig.1. Until then, PEM_IH10 was aligned only with PF_IH10. Therefore, it took a long time for alignment and it was unreliable. PF_IH11 can be also useful for a simple performance test for PEM_IH10.

3. Optimization of camera lens system

PEM_ IH10 is composed of pepper-pot mask and fluorescent plate shown in Fig.2. The pepper-pot mask made of 0.5 mm thick copper plate has holes with a diameter of 0.3 mm which are arranged at 3 mm interval in a 50 mm diameter circle. The fluorescent plate is made of copper plate (80 $\times$ 80 mm^2) poured with potassium bromide and tilted by 45 degrees. The distance between the pepper-pot mask and the center of fluorescent plate is 55 mm. Beams passing through the holes of pepper-pot mask stop and emit light on the fluorescent plate. The view is recorded by a digital camera set perpendicular to the beam direction.

In November 2017, the camera was changed from Sony HDR-CX720V to Gigabit Ethernet (GigE) camera because of remote control. As the focal length of lens for GigE camera was chosen as 8 mm, we had to adjust object distance so as to keep the image resolution less than 0.1 mm/pixel and remove image distortion. The distortion can be measured with graph paper pasted on the fluorescent plate. We chose 225 fiducial points at 5 mm interval in 70 $\times$ 70 mm^2, measured the bitmap position of fiducial points on the digital image, transformed the bitmap coordinates to the graph paper coordinates using transform coefficients given by correspondence between fiducial points and their bit map positions, and defined the difference between fiducial points and their transformed position as distortion. The distortion of Sony HDR-CX720V is shown in Fig.3. The image resolution is 0.03 mm/pixel and the standard deviation (SD) of x (horizontal) and y (vertical) is 0.03 and 0.04 mm, respectively.

On the other hand, the distortion of GigE camera is shown in Fig.4. The object distance was optimized to 250 mm. The image resolution is 0.08 mm/pixel and the SD of x

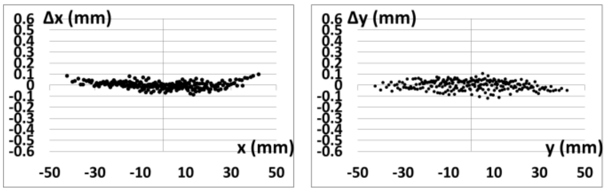

Figure 3. Differences in distribution between fiducial points and measured position on digital image recorded by HDR-CX720V: x-axis (left) and y-axis (right).

and y is 0.08 and 0.07 mm, respectively. Though this camera lens system is inferior to previous one, it was judged to be practical and adopted.

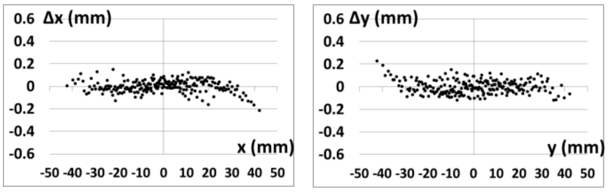

Figure 4. Differences in distribution between fiducial points and measured position recorded by GigE camera and CCTV lens (13VM308AS) with 250 mm object distance: x-axis (left) and y-axis (right).

Until May 2018, the transform coefficients given by correspondence between fiducial points and their bit map positions were made from 15 holes (11 holes with a diameter of 1 mm and 4 holes with a diameter of 2 mm) opened in the fluorescent plate. In order to see this effect, we transformed 225 bitmap positions of fiducial points on the digital image of graph paper recorded by optimized GigE camera, using the transform coefficients given by 15 holes. Figure 5 shows this difference between fiducial points and their transformed position.

From this result, the systematic displacement of x and y is found to be 0.3 mm and -0.3 mm, respectively. The SD of x and y is 0.12 and 0.19 mm, respectively. The differences are inversely related to fiducial points. This means that measured positons on the fluorescent plate are inclined to shrink. However, in fact, measured positons were found to be inclined to enlarge so that the measured angle needed to be corrected by a factor 0.9 to obtain an agreement with the beam-orbit calculation. It was found that the correction factor 0.9 did not result from the transform coefficient given by 15 holes. We will examine the reason for the correction factor 0.9 in a different way. For the transform coefficients, we judged to use the transform coefficients given by graph paper because it was better.

4. Problem of fluorescence agent thickness

In January 2018, a florescent plate was changed to a new one. After that, it seemed that the conformity became larger than before. In October 2018, we changed the fluorescent plate to another one of which thickness of fluorescent agent is thinner. As a result, the conformity seemed to improve. For confirmation, we tested two kinds of fluorescent agent thickness. One thickness is 4.2 μm and another is 30.9 μm. The thickness is defined as a value given by dividing the

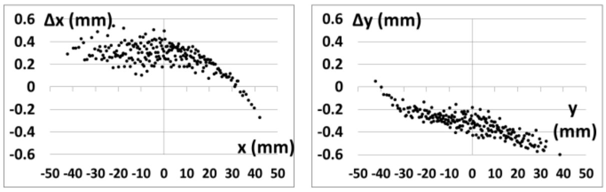

Figure 5. Differences in distribution between fiducial points and measured position on digital image, translated with fiducial points composed of 15 holes in the fluorescent plate, recorded by GigE camera and CCTV lens (13VM308AS) with 250 mm object distance: x-axis (left) and y-axis (right).

weight of the fluorescent agent by the area and the density. Test beam is $^{4}He^{2+}$ 15.4 keV and the beam intensity is 130 eμA. The result of beam-orbit calculation is compared with beam profiles measured by PF_IH11. The excitation current of SOIH11 set between PEM_IH10 and PF_IH11 was 50 A, as shown in Fig.1. The result of the x-profile conformity of thinner one and thicker one is 1.06 and 1.57, respectively. At the same time, the result of the y-profile conformity of thinner one and thicker one is 1.11 and 1.04, respectively. From this result, thicker one has larger conformity than thinner one in the x-axis, but thicker one has same conformity as thinner one in the y-axis. Overall, the conformity of thicker one is relatively large, but there seems to be little difference in this test.

The influence of thickness is considered to be related to the amount of light emission on the fluorescent agent. The amount of light emission recorded by digital camera is also related to the exposure time and amplification degree. This problem is not solved yet. We will examine the optimum combination between the thickness of fluorescent agent, and the exposure time and amplification degree of digital camera.

References

[1] T. Hoffmann et al., AIP Conf. Proc. **546**, 432 (2000).
[2] Y. Kotaka et al., Proc. 14th Annual Meeting of PASJ, (2017) p.1118-1122.
[3] Y. Kotaka et al., CNS Ann. Rep. 2017 (2019) 51.

Production of $^6Li^{3+}$ ion beam in Hyper ECR ion source

Y. Ohshiro, Y. Kotaka, H. Muto[a], H. Yamaguchi, N. Imai, Y. Sakemi, and S. Shimoura

Center for Nuclear Study, the University of Tokyo
[a]*School of General and Management Studies, Suwa Univeristy of Science*

1. Introduction

A Hyper ECR ion source injects various kinds of ion beams from gases and metals into the RIKEN AVF cyclotron [1–3]. This year, metal ion beams such as $^6Li^{3+}$, $^7Li^{2+}$, $^{10}B^{4+}$, $^{24}Mg^{8+}$ and $^{56}Fe^{15+}$ were successfully extracted from the cyclotron. Since the beam intensity of $^6Li^{3+}$ ion was fluctuated during delivery to the user, a crucible position of the ion source was optimized as follows.

The $^6Li^{3+}$ ion is separated in the ion source by watching a plasma light intensity. The beam was identified by analyzing many wavelengths of plasma light from the ion source. Since the beam has a Q/M of 1/2, many ions are mixed. Usually, these same Q/M ions were separated using the cyclotron magnet. However, by light intensity of ^{6}Li III line spectrum, the beam was also separated and adjusted in the ion source.

The beam of $^6Li^{3+}$ ion is stably enhanced at the crucible position near a RF wall of the ion source. The crucible temperature was increased in proportion to the RF power. Then, the amount of Li vapor supplied from the crucible into the plasma was adjusted by RF power and mirror coil current. These results are described.

2. On-axis insertion crucible method

Figure 1 shows a schematic diagram of the Hyper ECR ion source with the crucible. The ECR zone is formed by the mirror coil of MC1, MC2 and a hexapole magnet. In the $^6Li^{3+}$ ion beam production, the values of MC1 and MC2 are typically 588A and 490A, respectively, the length of the ECR zone is about 70 mm, the RF power is 450W and the supporting gas is He. The optimum position of the crucible was found by approaching the ECR zone starting from the RF wall.

The crucible is located away from the ECR zone where the temperature is constant. High RF power and an amount of Li vapor suitable for ion production were supplied to the plasma. The temperature was measured with a platinum rhodium thermocouple attached to the crucible. The vapor volume was determined from the vapor pressure curve. The crucible is a container with 5 nozzles of a 2 mm diameter and a 7 ml volume, filled with ^{6}Li pure metal. Therefore, the crucible position near the RF wall stably increased the $^6Li^{3+}$ ion beam.

3. Beam analysis by light intensity

A grating monochromator with a photomultiplier was installed in a straight line of a magnetic analyzer of the Hyper-ECR ion source [4]. The light intensity of gas and metal ion beams is observed during beam tuning. In the case of $^6Li^{3+}$ beam tuning, it was almost impossible to separate $^6Li^{3+}$, H_2^+, and $^4He^{2+}$ (Q/M = 1/2) by the magnetic analyzer of

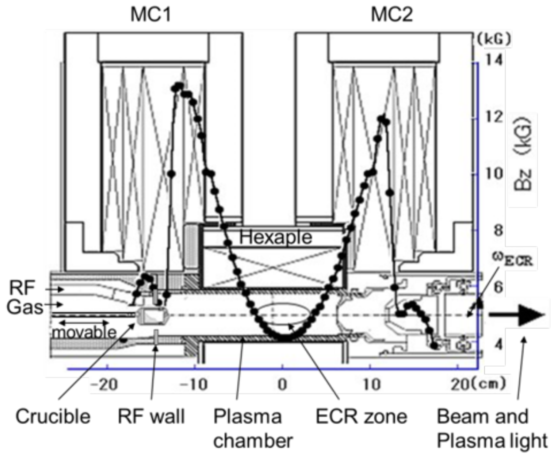

Figure 1. Schematic diagram of a Hyper ECR ion source with a crucible. The optimum position of the crucible was found by approaching an ECR zone starting from a RF wall.

the ion source.

Figure 2 shows the light intensity of ^{6}Li III line spectrum (λ = 516.7 nm) as a function of the analyzed $^6Li^{3+}$ beam intensity [5]. This research proves that the light intensity signal of ^{6}Li III is essential information for the $^6Li^{3+}$ beam tuning. Tuning of the $^6Li^{3+}$ beam without interrupting the beam time by watching the light intensity signal of the photomultiplier was successfully demonstrated.

4. Beam tuning by moving crucible

Figure 3 shows the beam intensity of $^6Li^{3+}$ ion as a function of the crucible position. The intensity increased rapidly at 35 mm in the crucible position from the RF wall and saturated at 40 mm. The maximum crucible temperature and the vapor pressure reached 480°C and 3×10^{-4} Pa, respectively. The final vacuum pressure was 5×10^{-5} Pa. Thus, the beam intensity changed greatly due to the excessive supply of the Li vapor at the crucible position near the ECR zone.

Even at the crucible position away from the ECR zone, it must be delicately controlled. Stabilization time of the beam intensity from the position change of the crucible to the beam enhancement was required for every its movement. Therefore, the stable production of the high intensity $^6Li^{3+}$ beam was difficult by changing the crucible position.

5. Optimization of crucible position

Figure 4 shows the RF power and the temperature as a function of the crucible position moving near the RF wall. They changed periodically with the crucible position. Furthermore, the RF power and the temperature increased to 450 W and 350 degrees, respectively, at the position of 9 mm. As a result, with the crucible fixed at this location,

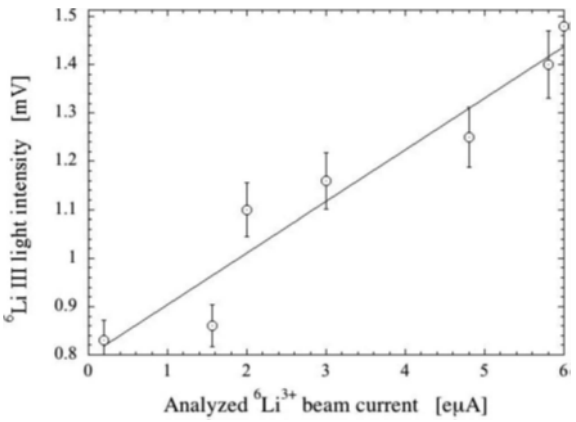

Figure 2. Light intensity of ^{6}Li III line spectrum as a function of analyzed $^6Li^{3+}$ beam intensity. Beam intensity was measured by a Faraday cup positioned at an extraction section after beam deflector of the cyclotron.

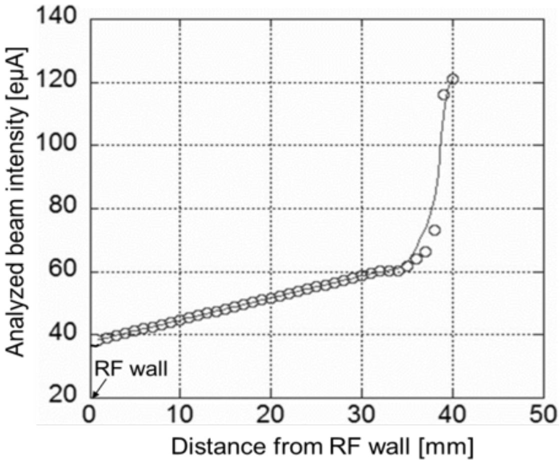

Figure 3. Analyzed beam intensity of $^6Li^{3+}$ ion as a function of a crucible position. The intensity increased rapidly at 35 mm in the crucible position from a RF wall and saturated at 40 mm.

the $^6Li^{3+}$ beam intensity was adjusted to high sensitivity in proportion to the RF power and the mirror coil current.

We have succeeded in providing the high intensity Li beam to the user stably.

1) The $^7Li^{2+}$ beam was delivered to the target at the intensity of approximately 2 eμA without readjustment during beam delivery.

2) The intensity of the $^6Li^{3+}$ beam was enhanced with the crucible fixed at the position of 9 mm from the RF wall in the ion source extracted from the cyclotron with the intensity of 6-8 eμA.

3) The $^6Li^{3+}$ beam was obtained with high intensity of 80-100 eμA from the ratio of $^7Li^{3+}$ and $^7Li^{2+}$ by using the mixed material of ^{6}Li and ^{7}Li in the ion source. The stability was confirmed for about 48 hours.

The quick response to the slight beam fluctuations by watching the plasma light intensity greatly contributed to the enhancement and the stability of Li ion beam without blocking the beam.

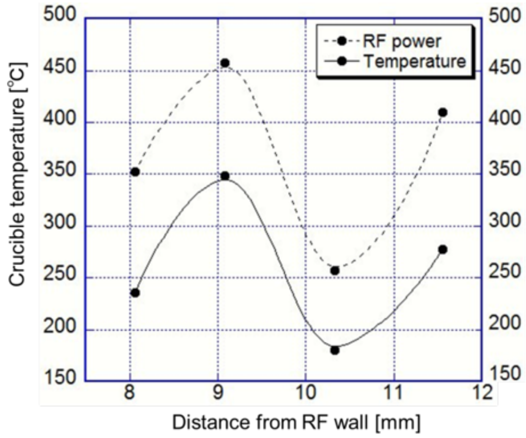

Figure 4. RF power and crucible temperature as a function of the position moving near the RF wall. Both the RF power and the temperature change periodically with the crucible position.

6. Summary

We optimized the crucible position and stably produced the high intensity beam of $^6Li^{3+}$ ion. The beam fluctuation was adjusted by monitoring the crucible temperature and the plasma light intensity in the ion source. By removing the gas mixed in the crucible, further enhancement and the highly stable production of the beam are planned.

References

[1] Y. Ohshiro, S. Yamaka, S. Watanabe, K. Kobayashi, Y. Kotaka et al., Rev. Sci. Instrum. **85**, 02A912 (2014).

[2] Y. Ohshiro, S. Yamaka et al., RIKEN Accel. Prog. Rep. **39**, 231 (2005).

[3] Y. Ohshiro, S. Watanabe et al., CNS Annual Report 2004 71 (2003).

[4] H. Muto et al., Rev. Sci. Instrum. **89** 016103 (2018).

[5] H. Muto et al., Rev. Sci. Instrum. **85** 126107 (2003).

Theoretical Nuclear Physics

Thick-restart block Lanczos method for the shell-model code "KSHELL"

N. Shimizu[a], T. Mizusaki[b], Y. Utsuno[c,a], and Y. Tsunoda[a]

[a] *Center for Nuclear Study, Graduate School of Science, The University of Tokyo*
[b] *Institute of Natural Sciences, Senshu University*
[c] *Advanced Science Research Center, Japan Atomic Energy Agency*

1. Introduction

The large-scale shell model (LSSM) calculation is one of the most useful methods to describe the nuclear spectroscopic information precisely. However, since the dimension of the Hamiltonian matrix in the LSSM tends to be huge, it is important to develop an efficient eigensolver for shell-model codes. In conventional shell-model codes such as OXBASH [1] and ANTOINE [2], the Lanczos method [3] has been used to solve the eigenvalue problem of the eigenvalue problem. The Lanczos method is known to be quite efficient to obtain a small number of the lowest eigenvalues.

As an alternative for the eigensolver of the LSSM calculations, we propose the thick-restart block Lanczos method, which is an extension of the Lanczos method with the block algorithm [4] and the thick-restart method [5]. Thus, we developed a shell-model code, named KSHELL [6], equipped with this method. It is applicable for massively parallel computations, and enables us to reveal nuclear statistical properties which are intensively investigated by recent experimental facilities. We demonstrate that the present method outperforms the conventional one. This report is condensed from Ref. [7].

The KSHELL code is based on the M-scheme representation, which is advantageous for large-scale calculations. In M-scheme, the shell-model wave function is represented as a linear combination of a vast number of Slater determinants, each of which has good J_z quantum number, but is not an eigenstate of the total angular momentum, J^2. The rotational symmetry of the wave function is fully restored as a consequence of the diagonalization of the Hamiltonian matrix [8].

2. Algorithm of the thick-restart block Lanczos method

We begin with the simplest, well-known Lanczos method [3]. In its algorithm, a few of the lowest eigenvalues of the Hamiltonian matrix, H, are approximated by the eigenvalues of a small matrix obtained by the Krylov subspace [9], which is defined as

$$\mathscr{K}_{l_m}(H,\boldsymbol{v}_1) = \{\boldsymbol{v}_1, H\boldsymbol{v}_1, H^2\boldsymbol{v}_1, H^3\boldsymbol{v}_1, \cdots, H^{l_m-1}\boldsymbol{v}_1\} \quad (1)$$

with $\boldsymbol{v}_1$ being an arbitrary initial vector and l_m being the number of the basis states.

The eigenvalue of the Krylov subspace, which is called Ritz value, converges to the lowest eigenvalues quite fast, namely l_m for the convergence is much smaller than the dimension of the matrix. In many shell-model codes including the KSHELL code, the bottleneck of the computation time is on-the-fly generation of the Hamiltonian matrix elements at every matrix-vector product. In order to suppress the cost of the on-the-fly generation, we introduce the block Lanczos method.

The block Lanczos method is one of the block Krylov subspace methods. The block Krylov subspace is defined as

$$\mathscr{K}_m(H,\boldsymbol{V}_1) = \{\boldsymbol{V}_1, H\boldsymbol{V}_1, H^2\boldsymbol{V}_1, \cdots, H^{m-1}\boldsymbol{V}_1\}. \quad (2)$$

The initial block of vectors are defined as $\boldsymbol{V}_1 = \left(\boldsymbol{v}_1^{(1)}, \boldsymbol{v}_1^{(2)}, \cdots, \boldsymbol{v}_1^{(q)}\right)$, where q is the block size. As m increases, the Ritz value is expected to converge faster than that of the Krylov subspace. Since the matrix elements are generated on the fly at every product of the matrix and block vectors, its cost is suppressed.

We also introduced the thick-restart method to suppress the number of vectors in the block Krylov subspace. The practical algorithm of the thick-restart block Lanczos method is shown in Alg. 1, with QR($\boldsymbol{W}$) being the QR decomposition of the matrix $\boldsymbol{W}$.

Algorithm 1 Algorithm of the thick-restart block Lanczos method

$\boldsymbol{V}_1$ be arbitrary vectors with $\boldsymbol{V}_1^T\boldsymbol{V}_1 = \boldsymbol{1}$ and $k_x := 0$.
for $l = 1,2,3,\cdots$ **do**
  for $k = 1,2,\cdots$ **do**
    $\boldsymbol{W} := H\boldsymbol{V}_k$
    $\boldsymbol{\alpha}_k := \boldsymbol{V}_k^T\boldsymbol{W}$
    $T_{k_x+q(k-1)+1:k_x+qk,k_x+q(k-1)+1:k_x+qk} := \boldsymbol{\alpha}_k$
    Diagonalize $T^{(k)}$ and stop if e_n converges
    Orthogonalize $\boldsymbol{W}$ with $\boldsymbol{v}_1, \boldsymbol{v}_2, \cdots, \boldsymbol{v}_{k_x+qk}$
    $\boldsymbol{V}_{k+1}\boldsymbol{\beta}_k :=$ QR($\boldsymbol{W}$)
    $T_{k_x+qk+1:k_x+q(k+1),k_x+q(k-1)+1:k_x+qk} := \boldsymbol{\beta}_k$
    $T_{k_x+q(k-1)+1:k_x+qk,k_x+qk+1:k_x+q(k+1)} := \boldsymbol{\beta}_k^T$
  end for
  Construct $T^{(l_s)}$ and $\boldsymbol{v}_k, 1 \le k \le l_s$ for restart
  $k_x := l_s$
end for

The restart is done so that the number of Lanczos vectors does not exceed the given upper limit l_m. The $T^{(k)}$ matrix after the restart is constructed as

$$T^{(k)} := \begin{pmatrix} E^{(l_s)} & \boldsymbol{r}^T & & & & & 0 \\ \boldsymbol{r} & \boldsymbol{\alpha}_1 & \boldsymbol{\beta}_1^T & & & & \\ & \boldsymbol{\beta}_1 & \boldsymbol{\alpha}_2 & \boldsymbol{\beta}_2^T & & & \\ & & \ddots & \ddots & \ddots & & \\ & & & \boldsymbol{\beta}_{k-2} & \boldsymbol{\alpha}_{k-1} & \boldsymbol{\beta}_{k-1}^T & \\ 0 & & & & \boldsymbol{\beta}_{k-1} & \boldsymbol{\alpha}_k & \end{pmatrix}, \quad (3)$$

where $E^{(l_s)}$ is a diagonal matrix whose matrix elements are the Ritz values $(e_1, e_2, \cdots, e_{l_s})$ of the matrix T which is constructed just before the restart. While the $T^{(k)}$ matrix is block triagonal before the restart, it is no longer block tridiagonal after the restart. The Lanczos vectors up to k-th iterations after the start or the restart are defined as

$$\begin{aligned} & \boldsymbol{v}_{k_x+1}, \boldsymbol{v}_{k_x+2}, \cdots, \boldsymbol{v}_{k_x+qk} \\ & := \boldsymbol{v}_1^{(1)}, \boldsymbol{v}_1^{(2)}, \cdots, \boldsymbol{v}_1^{(q)}, \boldsymbol{v}_2^{(1)}, \cdots\cdots, \boldsymbol{v}_k^{(q)}. \end{aligned} \tag{4}$$

These Lanczos vectors after the restart are constructed as

$$\boldsymbol{v}_k := \sum_j \boldsymbol{v}_j U_{jk} \quad \text{for} \quad k = 1, 2, \cdots, l_s \tag{5}$$

$$\boldsymbol{V}_1 := \boldsymbol{V}_{k_m+1} \tag{6}$$

$$\boldsymbol{r} := \boldsymbol{\beta}_{k_m} U_{k_x+q(k_m-1)+1:k_x+qk_m,1:l_s} \tag{7}$$

where e_k and U_{lk} are the k-th eigenvalue and eigenvector of the $T^{(k)}$ matrix before the restart. The k_m denotes the k just before the restart. See Ref. [7] for further details.

3. Total performance of the Lanczos methods

We describe the total performance of the four Lanczos methods, namely the simple Lanczos, the block Lanczos, the thick-restrat Lanczos, and the thick-restart block Lanczos methods. We measured the elapsed time to obtain the 32 lowest eigenvalues of ^{48}Cr with pf-shell model space and GXPF1A interaction [10]. This benchmark test was done utilizing the KSHELL code on 20 CPU cores of Intel Xeon E5-2680.

Figure 1 shows the elapsed times of these Lanczos methods, and also compares memory usage to store the Lanczos vectors. The block algorithm shortens the time of matrix-vector product and consequently the total time by almost half. On the other hand, the block Lanczos method requires the largest memory size among the four methods because of the largest number of the Lanczos vectors needed. The thick-restart algorithm enables us to constrain the number of Lanczos vectors to be stored. In this case, the maximum number of the Lanczos vectors is taken as $l_m = 200$, namely 3.1 GB. It also shortens the time of the reorthogonalization, which has little effect on the elapsed time when the Lanczos vectors are stored on memory. If one has to store the Lanczos vectors on a hard disk drive due to the lack of memory, the reorthogonalization process has a larger fraction of the elapsed time and the thick-restart algorithm will play a critical role. Thus, the thick-restart block Lanczos method is most efficient both in terms of elapsed time and memory usage.

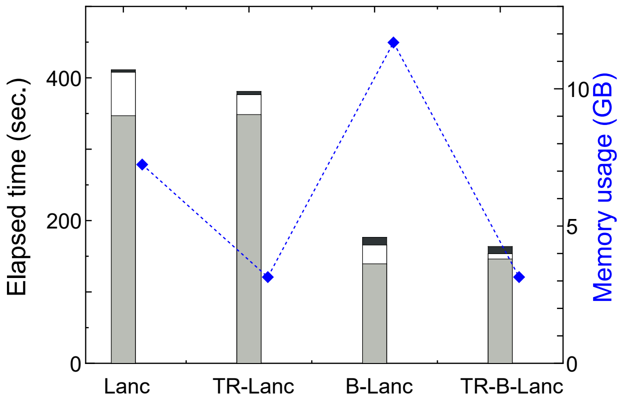

Figure 1. Total elapsed time to obtain the 32 lowest eigenvalues of ^{48}Cr with the simple Lanczos (Lanc), thick-restart Lanczos (TR-Lanc), block Lanczos (B-Lanc), and thick-restart block Lanczos (TR-B-Lanc) methods. The shaded, open, and filled bars denote the elapsed times of matrix-vectors products, reorthogonalizations, and the others, respectively. The memory usage to store the Lanczos vectors is shown as the blue diamonds with the dashed line. We take the block size $q = 8$ for the block methods and the maximum number of the Lanczos vectors $l_m = 200$ for the thick-restart methods. Taken from Ref. [7].

4. Summary

We introduced the thick-restart block Lanczos method as an eigensolver for large-scale shell-model calculations and discussed its performance in comparison with the conventional Lanczos method. Especially when a large number of eigenvalues are required, the block method drastically reduces the number of iterations and the additional cost of the on-the-fly generation of the matrix elements in the KSHELL code. Moreover, the thick-restart algorithm restricts the number of Lanczos vectors and reduces the cost of the reorthogonalization.

The M-scheme shell-model code KSHELL was developed for massively parallel computation and is advantageous to obtain highly excited states thanks to the thick-restart block Lanczos method. We demonstrated that the thick-restart block Lanczos method succeeds in reducing the elapsed time of the LSSM calculations by utilizing the KSHELL code taking ^{48}Cr as examples.

References

[1] B. A. Brown, A. Etchegoyen, and W. D. M. Rae, computer code OXBASH, the Oxford University-Buenos Aires-MSU shell model code, Michigan State University Cyclotron Laboratory Report No. 524, 1985.

[2] E. Caurier and F. Nowacki, Acta Phys. Pol. B **30**, 705 (1999)

[3] C. Lanczos, J. Res. Nat. Bur. Stand, **45**, 255 (1950).

[4] G. H. Golub, and R. Underwood, Proceedings of a Symposium Conducted by the Mathematics Research Center, the University of Wisconsin-Madison, Pages 361-377 (1977).

[5] K. Wu and H. Simon, SIAM. J. Matrix Anal. & Appl., **22**(2), 602 (2000).

[6] N. Shimizu, arXiv:1310.5431 [nucl-th].

[7] N. Shimizu, T. Mizusaki, Y. Utsuno and Y. Tsunoda, Comp. Phys. Comm. **244**, 372 (2019).

[8] E. Caurier, G. Martinez-Pinedo, F. Nowacki, A. Poves, and A. P. Zuker, Rev. Mod. Phys. **77**, 427 (2005).

[9] For review: Z. Bai, Appl. Num. Math. **43**, 9 (2002).

[10]M. Honma, T. Otsuka, B. A. Brown, and T. Mizusaki, Eur. Phys. J. A **25**, 499 (2005).

Ground-state properties of light nuclei from no-core Monte Carlo shell model with nonlocal *NN* interactions

T. Abe[a], P. Maris[b], T. Otsuka[c, d], N. Shimizu[a], Y. Utsuno[e], and J. P. Vary[b]

[a] *Center for Nuclear Study, the University of Tokyo*
[b] *Department of Physics and Astronomy, Iowa State University*
[c] *RIKEN Nishina Center*
[d] *Department of Physics, the University of Tokyo*
[e] *Advanced Science Research Center, Japan Atomic Energy Agency*

In this annual report, the current status of *ab-initio* computations with the Monte Carlo shell model (MCSM) is summarized. No-core MCSM calculations with realistic *NN* interactions have been performed on K computer to obtain ground-state energies and radii of light nuclei. From this investigation, it is found that no-core MCSM calculations with soft *NN* interactions can be carried out in relatively large basis spaces, providing sufficiently converged results for the ground states of light $4n$ self-conjugate nuclei in the p-shell region. In comparison of two interactions employed here, it is also observed that the recently constructed nonlocal *NN* interaction, Daejeon16, gives better agreements with experimental data than the originally proposed interaction, JISP16. Moreover, this study offers the firm ground to proceed further investigation on low-lying excited states of these nuclei where the α-cluster structure, one of the characteristic unveiled features in light nuclei, appears.

One of the major challenges in low-energy nuclear theory is to understand nuclear structure and reactions from first principles. For this purpose, a number of *ab-initio* studies have become actively done these days, mainly due to rapidly growing computational powers and advancing *ab-initio* techniques for quantum many-body calculations. Among them, the no-core shell model (NCSM) is one of the most powerful tools to study nuclear structure of light nuclei (for a recent review, see [1]). In the NCSM calculations, all the nucleon degrees of freedom are activated and nuclear forces from two- and three-nucleon interactions in free space (with some softening procedures of original hard interactions) are used as an input of many-body calculations. Typically, these many-body computations tend to be computationally expensive. Therefore, an alternate way to reduce the computational cost is required for calculations in heavier-mass nuclei beyond the p-shell region. In this direction, a couple of methods have been proposed and are providing an alternative path to *ab-initio* nuclear structure calculations, such as the importance-truncated NCSM [2] and symmetry-adapted NCSM [3].

No-core MCSM is one of the variants pursuing the same direction [4–7]. The MCSM has been originally proposed in the standard shell-model calculations with a valence space on top of an assumed inert core. This approach has succeeded the description of nuclear structure which has not been able to be applied in the standard shell-model calculations (for an earlier review article, see [8]). The MCSM has been still revised and developed so as to accommodate with current state-of-art supercomputers [6, 7]. Recently, it has also been applied to *ab-initio* calculations for light nuclei without assuming an inert core, known as the no-core MCSM.

For the application of the no-core MCSM, we have adopted the so-called JISP16 and Daejeon16 *NN* interactions due to the limitation of handling explicit $3N$ interactions at present. The JISP16 interaction is the J-matrix inverse scattering potential (JISP), one of the realistic nonlocal *NN* interactions constructed through a phase-equivalent transformation (PET) [9]. On the construction of the interaction, the PET parameters are adjusted by the fit of several binding energies of light nuclei up to ^{16}O in addition to two-nucleon scattering data and deuteron properties. The Daejeon16 interaction [10, 11] is the successor of the JISP16 interaction. This interaction is based on an *NN* interaction from chiral effective field theory (χEFT). It starts from the Idaho N3LO χEFT *NN* interaction being applied the similarity-renormalization-group (SRG) transformation with the flow parameter $\lambda = 1.5$ fm^{-1}. Then, the Daejeon16 interaction is constructed using the same technique of the PET for this SRG-evolved χEFT *NN* interaction to further soften the original one and to minimize the effects from many-body forces beyond *NN* in many-body systems. Although we treat only *NN* interactions in the no-core MCSM calculations, it is sufficient to prove the capability of MCSM approach for no-core calculations. It is also interesting to see how far towards the heavier-mass region and to what extent the low-lying nuclear structure can be reproduced under some reasonable uncertainties with such kind of nonlocal *NN* interactions. Note that, in the three-body system, there is a study [12] demonstrating that a given *NN* interaction is equivalent to the other *NN* + $3N$ interaction connected each other by a PET. It seems reasonable to extend this finding to minimize the effects from many-body forces utilizing the PET for the description of nuclear structure beyond few-body systems.

With these interactions, we have calculated ground-state energies and root-mean-square point-proton radii of ^{4}He, ^{8}Be, ^{12}C, ^{16}O and ^{20}Ne nuclei, including the nuclei where the standard NCSM calculations are hardly performed to obtain converged results due to huge dimensionality of Hamiltonian matrix. The no-core MCSM calculations have been done with several basis spaces (two to seven major shells) and harmonic-oscillator frequencies (corresponding $\hbar\omega = 10 - 40$ MeV). Using these results with various basis-space sizes and frequencies, we have extrapolated them to obtain *ab-inito* solution in the infinite basis-space

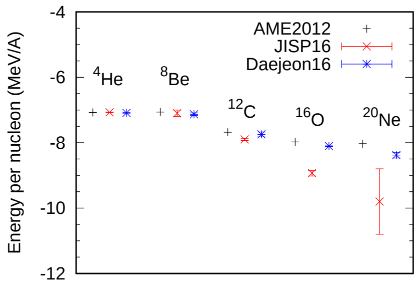

Figure 1. Ground-state energies per nucleon for light $4n$ self–conjugate nuclei, ^{4}He, ^{8}Be, ^{12}C, ^{16}O and ^{20}Ne. The red cross and blue star symbols with estimated uncertainties on extrapolations denote the no-core MCSM results with the JISP16 and Daejeon16 interactions, respectively. The black plus symbols indicate the experimental data taken from the compilation, the AME2012 atomic mass evaluation [13].

limit. Figure 1 shows preliminary extrapolated results of the no-core MCSM calculations for ground-state energies of these nuclei in comparison with experimental data. From a preliminary analysis on the no-core MCSM results, the JISP16 *NN* interaction provides the binding energies consistent with experimental data up to around ^{12}C, but being overbound as the atomic mass A increases, while the Daejeon16 interaction gives reasonable agreements with experimental data beyond the ^{12}C ground state. Note that poor convergence in terms of energy variance resluts in the large uncertainty on the ^{20}Ne energy for the JISP16 interaction.

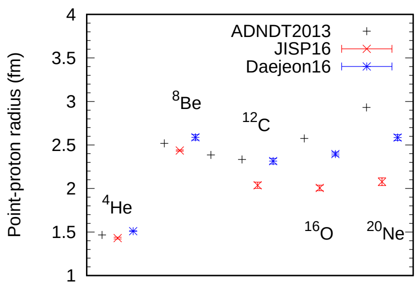

Figure 2. Point-proton radii for the ^{4}He, ^{8}Be, ^{12}C, ^{16}O and ^{20}Ne nuclei. The symbols are the same in Fig. 1. The experimental data are taken from the Atomic Data and Nuclear Data Tables 2013 [14]. Note that the experimental data for the neighboring Be isotopes, ^{7}Be and ^{9}Be, are taken as a reference for the ^{8}Be radius, due to the absence of data for the radius of unstable ^{8}Be nucleus.

Fig. 2 illustrates the point-proton radii for the corresponding nuclei together with experimental measurements. In a similar way, the radii for the JISP16 interaction are consistent with experiments up to around $A \sim 8$, but underestimate from A heavier than 8. On the other hand, the results with the Daejeon16 interaction improve the JISP16 ones, but the Daejeon16 interaction slightly underestimates the radii compared to experimental values as A increases.

From these preliminary results, it is inferred that the necessity of explicit inclusion of 3N potentials for heavier-mass nuclei above the upper p-shell region even in recent nonlocal *NN* interactions, such as the JISP16 and Daejeon16 interactions. It is, however, promising for the investigation of nuclear structure on p-shell nuclei, especially, the beryllium and carbon nuclei examined here. For these nuclei, the α-cluster structure appears, which is one of the main features in light nuclei. In addition, it seems to be advantageous for the investigation on such structure in the no-core MCSM that the basis-space truncation in this approach allows many-particle many-hole excitations compared to the truncations in the other NCSMs, facilitating the formation of α clusters in relatively smaller basis-space sizes. Hence, it is awaited to further proceed our investigations towards the understanding of the α-cluster structure from first principles, especially in the Be and C isotopes [4, 6, 7, 15].

References

[1] B. R. Barrett, P. Navrátil and J. P. Vary, Prog. Part. Nucl. Phys. **69**, 131 (2013).

[2] R. Roth and P. Navrátil, Phys. Rev. Lett. **99**, 092501 (2007).

[3] T. Dytrych, K. D. Sviratcheva, C. Bahri, J. P. Draayer and J. P. Vary, Phys. Rev. Lett. **98**, 162503 (2007).

[4] L. Liu, T. Otsuka, N. Shimizu, Y. Utsuno and R. Roth, Phys. Rev. C**86**, 014304 (2012).

[5] T. Abe, P. Maris, T. Otsuka, N. Shimizu, Y. Utsuno and J. P. Vary, Phys. Rev. C**86**, 054301 (2012).

[6] N. Shimizu, T. Abe, Y. Tsunoda, Y. Utsuno, T. Yoshida, T. Mizusaki, M. Honma and T. Otsuka, Prog. Theor. Exp. Phys. **01A205** (2012).

[7] N. Shimizu, T. Abe, M. Honma, T. Otsuka, T. Togashi, Y. Tsunoda, Y. Utsuno and T. Yoshida, Phys. Scr. **92**, 063001 (2017).

[8] T. Otsuka, M. Honma, T. Mizusaki, N. Shimizu and Y. Utsuno, Prog. Part. Nucl. Phys. **47**, 319 (2001).

[9] A. M. Shirokov, J. P. Vary, A. I. Mazur and T. A. Weber, Phys. Lett. B**644**, 33 (2007).

[10] A. M. Shirokov, I. J. Shin, Y. Kim, M. Sosonkina, P. Maris and J. P. Vary, Phys. Lett. B**761**, 87 (2016).

[11] I. J. Shin, Y. Kim, P. Maris, J. P. Vary, C. Forssén, J. Rotureau and N. Michel, J. Phys. G**44**, 075103 (2017).

[12] W. N. Polyzou and W. Glöckle, Few-Body Syst. **9**, 97 (1990).

[13] M. Wang, G. Audi, A. H. Wapstra, F. G. Kondev, M. MacCormick, X. Xu and B. Pfeiffer, Chinese Phys. C**36**, 1603 (2012).

[14] I. Angeli and K. P. Marinova, Atomic Data and Nuclear Data Tables **99**, 69 (2013).

[15] T. Yoshida, N. Shimizu, T. Abe and T. Otsuka, JPS Conf. Proc. **6**, 010021 (2015).

Shell model predictions for $\beta\beta$ decay

J. Menéndez

Center for Nuclear Study, Graduate School of Science, The University of Tokyo

Most unstable nuclei decay via β decay or electron capture (EC). However, for a few dozen even-even nuclei the dominant decay channel is the much slower second-order $\beta\beta$ decay or double EC (ECEC). This occurs when β decay and EC are either forbidden—the odd-odd isobars are less bound—or very suppressed—all energetically available states in odd-odd isobars have high spins only reachable via highly-forbidden Fermi or Gamow-Teller transitions.

$\beta\beta$ decay is intriguing because a mode where only two electrons are emitted—without antineutrinos—is predicted by extensions of the Standard Model of particle physics. A detection of such neutrinoless $\beta\beta$ decay would have profound implications: proof that neutrinos are its own antiparticle (Majorana particles); observation of lepton-number non-conservation; and information on the absolute neutrino mass. Worldwide, experiments pursue the first neutrinoless $\beta\beta$ signal.

The neutrinoless $\beta\beta$ decay rate depends on a nuclear matrix element that needs to be calculated by nuclear theory. Due to this, reliable matrix element values are needed to estimate the sensitivity of experiments, and to fully exploit the observation of a signal. However, neutrinoless $\beta\beta$ decay matrix elements are poorly known, with predictions from the nuclear shell model, energy-density functional theory and the quasiparticle random-phase approximation (QRPA) differing in more than a factor two [1]. Therefore, nuclear theory calculations need to be tested and calibrated to other nuclear observables related to neutrinoless $\beta\beta$ decay [2].

Two-neutrino $\beta\beta$ decay ($2\nu\beta\beta$), the second-order equivalent of the standard β decay, is closely connected to neutrinoless $\beta\beta$ decay. Two antineutrinos are emitted, but the initial and final states are the same, and the transition operation similar—dominated by the physics of spin and isospin—to neutrinoless $\beta\beta$ decay. Likewise, the two-neutrino ECEC (2νECEC) is also a good probe of neutrinoless $\beta\beta$ decay where nuclear structure calculations can be tested.

The more basic observable is the decay rate. In the case of $2\nu\beta\beta$ or 2νECEC, to leading order the rate is [3]

$$\left(T_{1/2}\right)^{-1} \simeq G_{2\nu,0}\, g_A^4 \left(M_{2\nu}\right)^2, \tag{1}$$

with $G_{2\nu,0}$ a known phase-space factor, $g_A = 1.27$ the axial coupling constant, and $M_{2\nu}$ the nuclear matrix element.

We calculated $M_{2\nu}$ for the 2νECEC of ^{124}Xe into ^{124}Te with the shell model [4]. We used a configuration space formed by the $0g_{7/2}$, $1d_{5/2}$, $1d_{3/2}$, $2s_{1/2}$, and $0h_{11/2}$ single-particle orbitals for neutrons and protons, with a ^{100}Sn core. We used the GCN5082 effective Hamiltonian [5]. Because the dimensions of the configuration space are too large for an exact diagonalization, we had to truncate the number of nucleons excited from the lower-energy $0g_{7/2}$, $1d_{5/2}$ orbitals to the higher-energy $1d_{3/2}$, $2s_{1/2}$, and $0h_{11/2}$ ones.

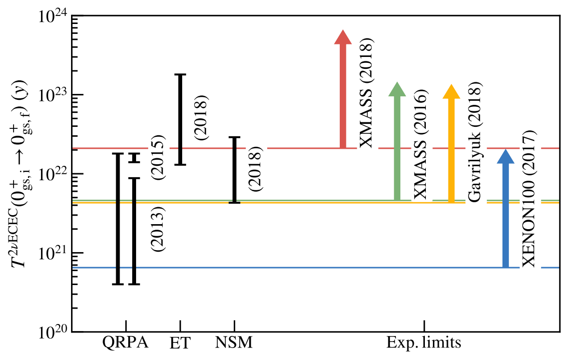

Figure 1. Half-life of ^{124}Xe. Predictions from the shell model (NSM), effective theory (ET) and QRPA are compared to experimental limits, shown by the colored arrows. From Ref. [4].

On the other hand, it is well-known that shell model calculations require an adjustment, or normalization, of the transition operator when describing β, EC and $\beta\beta$ decays [1]. This is usually known as "quenching", and translated into an effective value of the axial coupling constant $g_A^{\mathrm{eff}} = q\,g_A$. To take this deficiency of the shell model into account we corrected our results by three different values of q that guarantee a good description of: a) Gamow-Teller decays in the xenon mass region [6]; b) $2\nu\beta\beta$ beta decays in the xenon mass region; and c) the $2\nu\beta\beta$ decay of ^{136}Xe. Unfortunately, the values q_a, q_b, q_c are different, and all three classes of observables cannot be described with a single adjustment [6].

Figure 1 shows the shell model results (NSM) for the 2νECEC decay rate of ^{124}Xe. The uncertainty bar includes the results obtained with the three q values considered—about two thirds of the error bar—and the truncations in the configuration space—the remaining one third. The shell model result is consistent with other theoretical predictions from an effective theory (ET) [4] and the QRPA [7,8], and is also barely consistent with the half-life limits set by various experiments (colored arrows) [9–12]. After the theoretical prediction was submitted, the XENON collaboration measured the ^{124}Xe 2νECEC half-life $T_{1/2} = 1.8 \cdot 10^{22}$ y [13], in excellent agreement with the shell model prediction.

In addition to the decay rate, experiments can also measure the summed energy of the two electrons emitted. Although the shape of the energy spectrum depends mostly on the kinematics as suggested by Eq. (1), a more precise expression for the decay rate points out a sensitivity to the nuclear matrix elements [3]:

$$\left(T_{1/2}\right)^{-1} = g_A^4 \left[G_{2\nu,0}\left(M_{2\nu}\right)^2 + G_{2\nu,2}\, M_{2\nu}\, M_{GT3}\right] \tag{2}$$

where $G_{2\nu,2}$ is another known phase-space factor, and M_{GT3}

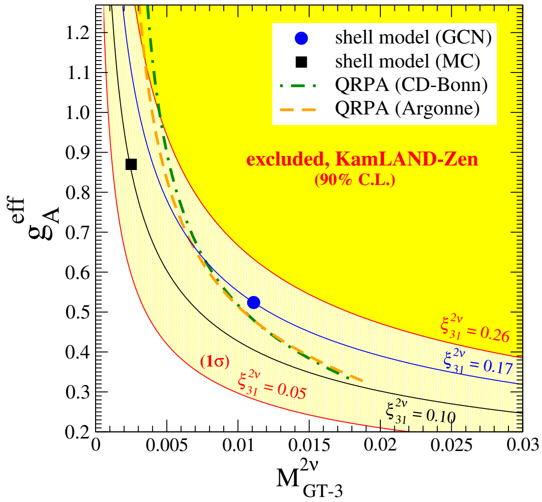

Figure 2. ^{136}Xe $2\nu\beta\beta$ decay, predictions from the GCN5082 (MC) shell model calculation, shown as blue circle (black square), and the QRPA (dashed lines). The dark (light) yellow region is excluded by the KamLAND-Zen analysis at 90% (1σ) confidence level. From Ref. [14].

a subleading nuclear matrix element. Since $M_{GT3} \ll M_{2\nu}$, the impact of Eq. (2) in the decay rate is very small. However, since the phase-space factors of the first and second terms in Eq. (2) are different, the summed electron spectrum has two distinct contributions. In fact, shape of the spectrum is sensitive to the ratio of nuclear matrix elements $M_{GT3}/M_{2\nu}$ [3].

Therefore, experiments can be confronted to calculations in a two-dimension plot including the measurement of the decay rate and the shape of the electron spectrum. This can be represented as the value of $g_A^{\rm eff}$ needed by the calculations to reproduce the measured decay rate—from the calculated $M_{2\nu}$—and the value of M_{GT3}.

We performed shell model calculations of the $2\nu\beta\beta$ of ^{136}Xe into ^{136}Ba [14], in the same configuration space as for ^{124}Xe. In this case, exact diagonalizations are feasible. We used the GCN5082, complemented with the MC effective Hamiltonian [15]. We obtained theoretical results for the leading and subleading nuclear matrix elements $M_{2\nu}$ and M_{GT3}.

Figure 2 compares the theoretical predictions with the result of the analysis of the data measured by the KamLAND-Zen collaboration [14]. The experimental results exclude the dark yellow region, and are consistent with the shell model predictions from both the GCN5082 and MC Hamiltonians. In contrast, part of the QRPA predictions [14] are excluded at 90% confidence level. The shell model predictions will be further tested by more stringent, future $2\nu\beta\beta$ measurements on ^{136}Xe, which will also determine whether the predictions from GCN5082 or MC are in better agreement with data.

In short, we have performed shell model calculations of the nuclear matrix elements for the 2νECEC of ^{124}Xe and the $2\nu\beta\beta$ of ^{136}Xe. The theoretical predictions have been challenged by recent measurements by the XENON (^{124}Xe) and KamLAND-Zen (^{136}Xe) collaborations. For ^{124}Xe the theoretical prediction is in excellent agreement with the measured decay rate, while for ^{136}Xe the calculated values are consistent with the experimental limits set by the measured electron spectrum.

References

[1] J. Engel, and J. Menéndez, Rep. Prog. Phys. **80**, 046301 (2017).
[2] N. Shimizu, J. Menéndez, and K. Yako, Phys. Rev. Lett. **120**, 142502 (2018).
[3] F. Šimkovic, R. Dvornický, D. Štefánik and A. Faessler, Phys. Rev. Lett. **122**, 192501 (2019).
[4] E. A. Coello Pérez, J. Menéndez, and A. Schwenk, Phys. Lett. B **797**, 134885 (2019).
[5] J. Menéndez, A. Poves, E. Caurier, and F. Nowacki, Nucl. Phys. A. **818**, 139 (2009).
[6] E. Caurier, F. Nowacki, and A. Poves, Phys. Lett. B **711**, 62 (2012).
[7] J. Suhonen, J. Phys. G: Nucl. Part. Phys. **40**, 075102 (2012).
[8] P. Pirinen, and J. Suhonen, Phys. Rev. C **91**, 054309 (2015).
[9] XMASS Collaboration, Phys. Lett. B **759**, 64 (2016).
[10] XENON Collaboration, Phys. Rev. C **95**, 024605 (2017).
[11] Gavrilyuk et al., Phys. Part. Nucl. **49**, 36 (2018).
[12] XMASS Collaboration, Prog. Theo. Exp. Phys. **2018**, 053D03 (2018).
[13] XENON Collaboration, Nature **568**, 532 (2019).
[14] KamLAND-Zen Collaboration, J. Menéndez, R. Dvornický, and F. Šimkovic, Phys. Rev. Lett. **122**, 192501 (2019).
[15] C. Qi, and Z. X. Xu, Phys. Rev. C **86**, 044323 (2012).

Shape transition in Sm isotopes studied by Monte Carlo shell model

Y. Tsunoda[a], T. Otsuka[b,a,c,d,e], and N. Shimizu[a]

[a] *Center for Nuclear Study, the University of Tokyo*
[b] *Department of Physics, the University of Tokyo*
[c] *RIKEN Nishina Center*
[d] *Instituut voor Kern- en Stralingsfysica, KU Leuven, Belgium*
[e] *National Superconducting Cyclotron Laboratory, Michigan State University, USA*

Nuclear shape is one of the most important properties for the study of the nuclear collectivity. Sm isotopes are considered to be spherical at $N = 82$, a magic number, and become deformed as N increases. We have investigated shapes of these Sm isotopes by using the Monte Carlo shell model (MCSM) calculations [1–3] and this work is partially contained in Ref. [4].

In order to describe nuclear deformation in the shell model, we have to use sufficiently large model space. The model space used in our calculations is the $0g_{9/2}$, $0g_{7/2}$, $1d_{5/2}$, $1d_{3/2}$, $2s_{1/2}$, $0h_{11/2}$, $1f_{7/2}$, and $2p_{3/2}$ orbits for protons, and the $0h_{11/2}$, $0h_{9/2}$, $1f_{7/2}$, $1f_{5/2}$, $2p_{3/2}$, $2p_{1/2}$, $0i_{13/2}$, $1g_{9/2}$, $2d_{5/2}$, and $3s_{1/2}$ orbits for neutrons. We use the effective interaction as is used in Ref. [4]. We performed MCSM calculations in order to use this large model space. In the MCSM, the wave function $|\Psi\rangle$ is represented as a superposition of the projected Slater determinants (MCSM basis vectors) as

$$|\Psi\rangle = \sum_{n,K} f_{n,K} P^{J\pi}_{MK} |\phi_n\rangle,$$

where $P^{J\pi}_{MK}$ is the angular-momentum and parity projector and $|\phi_n\rangle$ is a Slater determinant. Coefficients $f_{n,K}$ are determined by the diagonalization of the Hamiltonian matrix in the subspace spanned by the MCSM basis vectors $P^{J\pi}_{MK}|\phi_n\rangle$. $|\phi_n\rangle$ is determined to minimize the expectation value of the energy of the wave function. We can analyze the nuclear intrinsic shape by using the MCSM basis vector before projection, $|\phi_n\rangle$. In this method, we use the figure (referred to as T-plot) of the potential energy surface (PES) with circles indicating the shape of the MCSM basis vector. Examples of T-plot are shown in Figs. 3c-f. The PES is calculated by constrained Hartree-Fock (CHF) method using the shell-model effective interaction. We calculate the quadrupole moments, Q_0 and Q_2, of the MCSM basis vector before projection and locate a circle at the corresponding place in the PES. The area of the circle is proportional to the overlap probability between the MCSM basis vector $P^{J\pi}_{MK}|\phi_n\rangle$ and the wave function $|\Psi\rangle$. Thus, the distribution pattern of the circles indicates the nuclear intrinsic shape for the wave function. Although the $J = 0$ wave function is isotropic, we can analyze intrinsic shape of the 0^+ state because we use the MCSM basis vector before the angular-momentum projection. The quadrupole deformation parameter β_2 is calculated as

$$\beta_2 = f_{\rm scale}\sqrt{\frac{5}{16\pi}}\frac{4\pi}{3R^2A}\sqrt{(Q_0)^2+2(Q_2)^2},$$

where $R = 1.2A^{1/3}$ fm and $f_{\rm scale} = e_p/e + e_n/e$ with effective charges $e_p = 1.5e$ and $e_n = 0.5e$.

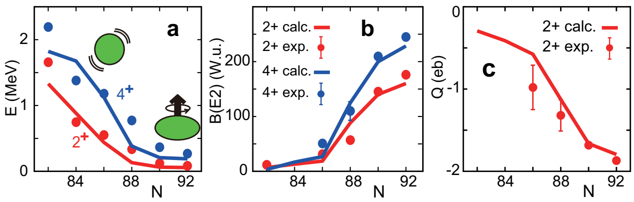

Figure 1. Systematic changes of the 2^+_1 and 4^+_1 states in Sm isotopes. **a**, excitation energies [5]. **b**, $B(E2;2^+_1 \to 0^+_1)$ and $B(E2;4^+_1 \to 2^+_1)$ values [5]. **c**, spectroscopic electric quadrupole moment of the 2^+_1 state [6]. Adapted from Fig. 1 of Ref. [4].

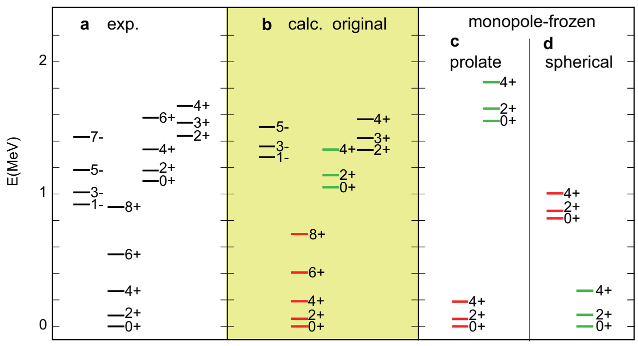

Figure 2. Level schemes of ^{154}Sm. **a**, experimental levels [5]. **b-d**, calculated levels of the original and monopole-frozen interactions. Adapted from Fig. 2 of Ref. [4].

We calculated the 0^+_1, 2^+_1, and 4^+_1 states of the even-even nuclei from ^{144}Sm to ^{154}Sm. Figure 1a shows excitation energies of the 2^+_1 and 4^+_1 states. These energies are high in lighter nuclei and $E(4^+)/E(2^+) \sim 2$ around $N = 86$ implies vibrational excitation. The energies are low in heavier nuclei and $E(4^+)/E(2^+) \sim 10/3$ implies rotation of deformed nuclei. Figures 1b and c show $B(E2)$ values and spectroscopic electric quadrupole moments, respectively, and suggest deformation in heavier nuclei. Our calculations of Sm isotopes agree with experiments.

We calculated several rotational bands of ^{154}Sm. Figures 2a and b show level schemes of ^{154}Sm of experiments and calculations, respectively. Experimental levels are reproduced by calculations. Prolate and triaxial bands built on

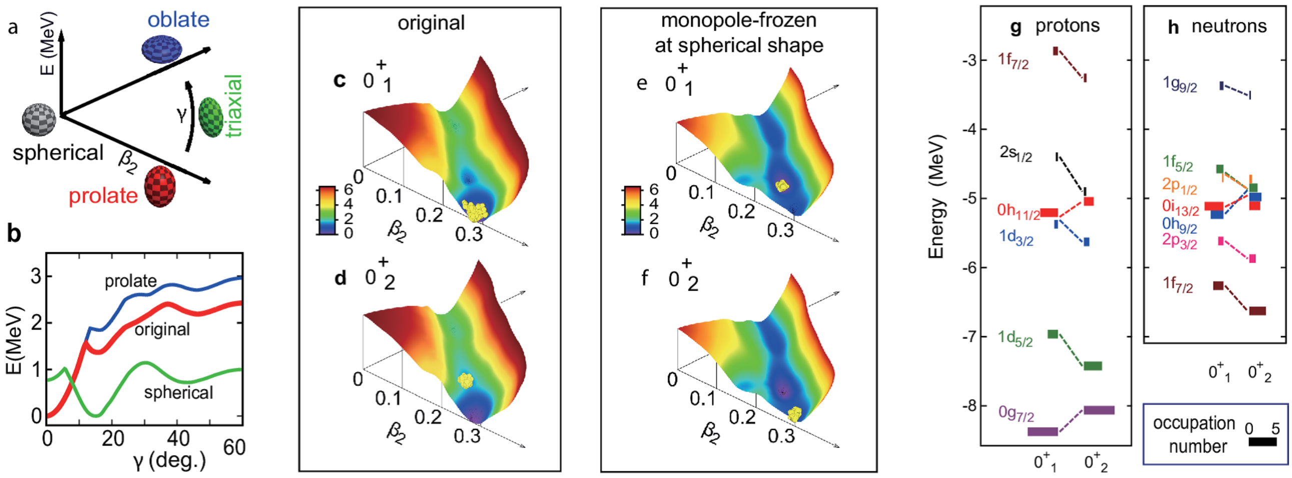

Figure 3. Properties of the 0^+_1 and 0^+_2 states of ^{154}Sm. **a**, deformation parameters β_2, γ and shapes corresponding to **c**-**f**. **b**, lowest value of PES for a given γ value for the original and the prolate and spherical monopole-frozen interactions. **c**-**f**, three-dimensional T-plot of the original and spherical monopole-frozen interactions. **g**, **h**, ESPE (vertical position) and occupation number (horizontal width). Adapted from Fig. 3 of Ref. [4].

0^+ states are shown in red and green, respectively. Figures 3c and d show T-plots of the prolate 0^+_1 and the triaxial 0^+_2 states, respectively. Figure 3a explains the axes of Figs. 3c-f and corresponding shapes. Distribution patterns of yellow circles in the T-plots indicate shapes of the corresponding state.

Figures 3g and h show effective single-particle energies (ESPEs) and occupation numbers of each single-particle orbit of the 0^+_1 and 0^+_2 states. The ESPEs are shifted from the bare single-particle energies (SPEs) by a part of two-body interaction with other nucleons, called the monopole interaction. The effect of the monopole interaction between any two orbits depends on the occupation numbers of the orbits. Thus, the occupation pattern determines the ESPEs. The 0^+_1 and 0^+_2 states show different occupation patterns and corresponding ESPEs.

In order to investigate the effect of the monopole interaction, we made a "monopole-frozen" analysis [4]. We performed MCSM calculations by using the effective interaction without the monopole interaction in the analysis. The ESPEs become constants and equal to the input SPEs. We take the ESPEs of the prolate 0^+_1 state of the original calculation as the input. The results of the prolate monopole-frozen calculation are shown in Fig. 2c. The excitation energies of the triaxial states (green) of the original case become lower than those of the prolate monopole-frozen case. This suggests that the ESPEs of the triaxial state are spontaneously optimized to gain binding energy in the original case. The results of another monopole-frozen calculation with ESPEs of the spherical CHF solution are shown in Fig. 2d and the ground state becomes triaxial. The particle-hole excitation from the spherical configuration changes the ESPEs differently in prolate and triaxial states, and the gain of the binding energy by the change of the ESPEs is also different in the original calculation. T-plots of the spherical monopole-frozen case are shown in Figs. 3e and f. Figure 3b shows three different PESs of the three cases and energies of the prolate ($\gamma \sim 0°$) and triaxial ($\gamma \sim 15°$) minima are consistent with the energies of the 0^+ states.

This work has been supported in part by MEXT as "Priority Issue on post-K computer" (Elucidation of the Fundamental Laws and Evolution of the Universe) and JICFuS. The MCSM calculations were performed on the K computer at the RIKEN AICS (Project ID: hp160211, hp170230, hp180179).

References

[1] T. Otsuka, M. Honma, T. Mizusaki, N. Shimizu, and Y. Utsuno, Prog. Part. Nucl. Phys. **47**, 319 (2001).
[2] N. Shimizu, T. Abe, Y. Tsunoda, Y. Utsuno, T. Yoshida, T. Mizusaki, M. Honma, and T. Otsuka, Prog. Theor. Exp. Phys. **2012**, 01A205 (2012).
[3] N. Shimizu, T. Abe, M. Honma, T. Otsuka, T. Togashi, Y. Tsunoda, Y. Utsuno, and T. Yoshida, Phys. Scr. **92**, 063001 (2017).
[4] T. Otsuka, Y. Tsunoda, T. Abe, N. Shimizu, and P. Van Duppen, Phys. Rev. Lett. **123**, 222502 (2019).
[5] National Nuclear Data Center, Evaluated Nuclear Structure Data File, http://www.nndc.bnl.gov/ensdf/.
[6] N. J. Stone, At. Data Nucl. Data Tables **111-112**, 1 (2016).

Other Activities

The 17th CNS International Summer School CNSSS18

M. Dozono, T. Gunji, S. Hayakawa, N. Imai, H. Liang[a,b], S. Michimasa, Y. Mizoi[c], H. Nagahama, S. Ota, T. Otsuka[a], H. Sakai[a], Y. Sakemi, H. Sakurai[a,b], N. Shimizu, S. Shimoura, H. Ueno[a], T. Uesaka[a], Y. Utsuno[d], K. Yako, H. Yamaguchi, K. Yoneda

Center for Nuclear Study, Graduate School of Science, University of Tokyo
[a]RIKEN Nishina Center
[b]Department of Physics, Univ. of Tokyo
[c]Faculty of Engineering, Osaka Electro-Communication University
[d]Advanced Science Research Center, Japan Atomic Energy Agency

The 17th CNS International Summer School (CNSSS18) was hosted by Center for Nuclear Study (CNS) from 22nd to 28th in August, 2018. The school was supported by RIKEN Nishina Center and Asian Nuclear Physics Association (ANPhA). The venue was the Nishina hall in the Wako campus of RIKEN.

The summer school was the seventeenth one in the series which aimed at fostering graduate students and postdocs by providing basic knowledge and perspectives of nuclear physics. It consisted of lectures by leading scientists in the fields of both experimental and theoretical nuclear physics. Each lecture started with an introductory talk from the fundamental point of view and ended with up-to-date topics in the relevant field.

The list of the lecturers and the title of lectures are following:

- Dr. Takashi Abe (CNS, Univ. of Tokyo, Japan), "Nuclear structure with *ab-initio* theory"
- Prof. Yasuyuki Akiba (BNL/RIKEN, Japan), "High energy heavy ion collision"
- Prof. Peter Butler (Univ. of Liverpool, UK), "Nuclear structure studies with RIB"
- Prof. Masaaki Kimura (Hokkaido Univ. Japan), "Nuclear Structure theory"
- Dr. Alberto Mengoni (Bologna/INFN, Italy), "Theoretical and experimental nuclear astrophysics"
- Prof. Toshimi Suda (Tohoku Univ., Japan), "Electron scattering from nucleon and nuclei"
- Dr. Juzo Zanihiro (RIKEN, Japan), "Overview of RIBF"

Seven lecturers and ninety-seven participants joined the school from six countries. Two lecturers and twenty participants came from foreign institutes. The time of each class was 50 minutes. There was 10 minutes break between the class to encourage the participants to communicate the lecturers. They talked each other in free discussion times such as breaks, lunch times, welcome and poster session in a relaxed atmosphere. Figure 1 presents a group photo of all the participants with the lecturers.

As traditional, there were four "Young Scientist Sessions", where given by graduate students and postdocs. We

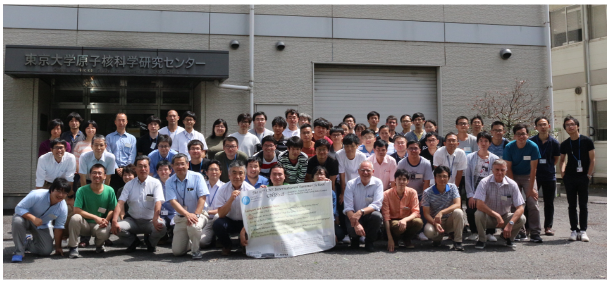

Figure 1. A group photos of the participants of CNSSS18 with the lecturers.

had nineteen oral presentations and twelve poster presentation. Since 2017, we have the CNSSS young scientist awards (CNSSSYS awards) for the good presentations. A few winners were selected from each young scientist sessions by the members of organizing committee and the lecturers. The winners of the second CNSSSYS award were;

- Mr. Noritaka Kitamura (CNS, Univ. of Tokyo) "Characterization of a titanium target for two-neutron transfer reaction at TRIUMF"
- Ms. Heamin Ko (Soongsil Univ.) "Neutrino self-interaction and MSW effect on the neutrino-process in core-collapse supernovae"
- Mr. Xuan Wang (RCNP, Osaka Univ.) "Measurement of Two-neutron transfer raction ^{11}Li(p, t)^{8}Li at 62.4 MeV"
- Mr. Yushin Yamada (Kyushu Univ.) "The study of the resonant states in ^{12}C+nucleon scattering"

The certificate of the awards were presented to them as demonstrated in Fig. 2.

The best presenter among them, Mr. Noritaka Kitamura, was also awarded the APPS-DNP/ANPhA prize for young physicist, which was sponsered by AAPPS-DNP/ANPhA. He received the certificate as well as the prize money as prestend in Fig. 3.

The organizers appreciate Nishina Center for providing the venue. We are grateful to supports from ANPhA. We thank administration staffs of the CNS for their helpful supports. We also thank graduate students and postdocs in the CNS for their dedicated efforts. Finally we acknowledge all the lecturers and participants for their contributions to the CNSSS18.

Figure 2. The winners of the first CNSSS young scientist awards. From right, Prof. Shimoura (school master), Mr. Yushin Yamada, Mr. Xuan Wang, Mr. Noritaka Kitamura, and Ms. Heamin Ko.

Figure 3. The ceremony of the AAPPS-DNP/ANPhA prize. Mr. Noritaka Kitamura received the certificate of the AAPPS-DNP/ANPhA prize for the young physicist from the chair of the ANPhA, Prof. Kazuhiro Tanaka. From the right, Prof. Tohru Motobayashi, Mr. Noritaka Kitamura, and Prof. Kazuhiro Tanaka.

Laboratory Exercise for Undergraduate Students

S. Ota, M. Niikura[a], N. Ozawa, T. Koiwai, K. Yako, H. Sakurai[a,b] and S. Shimoura

Center for Nuclear Study, Graduate School of Science, University of Tokyo
[a] *Department of Physics, University of Tokyo*
[b] *RIKEN Nishina Center*

Nuclear scattering experiments were performed as a laboratory exercise for undergraduate students of the University of Tokyo. This program was aiming at providing undergraduate students with an opportunity to learn how to study subatomic physics by using an ion beam from an accelerator. In 2017, 32 students attended this program.

The four beam times were scheduled in the second semester for third-year students, and 8 students participated in each beam time. The experiments were performed at the RIBF using a 26-MeV alpha beam accelerated by the AVF cyclotron. The alpha beam extracted from the AVF cyclotron was transported to the E7B beam line in the E7 experimental hall. The scattering chamber has two separate target ports which enable us to perform two independent experiments without opening the chamber during the beam time. In each beam time, the students were divided into two groups and took one of the following two subjects:

(1) Measurement of elastic scattering of incident alpha particle with ^{197}Au, to learn how to determine nuclear size.

(2) Measurement of gamma rays emitted from the cascade decay of highly excited ^{154}Gd and ^{184}Os, to learn the nuclear deformation.

Before the experiment, the students took a course on the basic handling of the semiconductor detectors and electronic circuits at the Hongo campus, and attended a radiation safety lecture at RIKEN. They also joined a tour to the RI beam factory at RIKEN.

In the α+^{197}Au measurement, α particles scattered with the Au target with a thickness of 1 μm were detected using a silicon PIN-diode located 15-cm away from the target. A collimator with a diameter of 6 mm was attached on the silicon detector. The energy spectrum of the scattered α particles was recorded by a multi-channel analyzer (MCA) system. The beam was stopped by a Faraday cup located downstream of the scattering chamber. The cross section for the alpha elastic scattering was measured in the angular range of $\theta_{\rm lab} = 20-150^\circ$.

The measured cross section was compared with the calculated cross section of the Rutherford scattering. The cross section was also analyzed by the potential model calculation, and the radius of the ^{197}Au nucleus was discussed. Some students obtained the radius of $\sim$10 fm by using a classical model where the trajectory of the α particle in the nuclear potential is obtained using the Runge-Kutta method. Others tried to understand the scattering process by calculating the angular distribution using the distorted wave Born approximation method with a Coulomb wave function and a realistic nuclear potential.

In the measurement of gamma rays, excited states in ^{154}Gd and ^{184}Os nuclei were populated by the ^{152}Sm(α,2n) and ^{182}W(α,2n) reactions, respectively. The gamma rays emitted from the cascade decay of the rotational bands were measured by a high-purity germanium detector located 30-cm away from the target. The energy of the gamma ray were recorded by the MCA system. The gain and the efficiency of the detector system had been calibrated using standard gamma-ray sources of ^{22}Na, ^{60}Co, ^{133}Ba, and ^{137}Cs. The gamma rays from the 10^+ and 8^+ states in ^{154}Gd and ^{184}Os, respectively, were successfully identified. Based on the energies of the gamma rays, the moment of inertia and the deformation parameters of the excited states were discussed by using a classical rigid rotor model and a irrotational fluid model. The students found that the reality lies between the two extreme models. The initial population among the levels in the rotational band was also discussed by taking the effect of the internal conversion into account.

It was the first time for most of the students to use large experimental equipments. They learned basic things about the experimental nuclear physics and how to extract physics from the data. We believe this program was very impressive for the students. The authors would like to thank Dr. K. Tanaka, the CNS accelerator group, and the RIBF cyclotron crew for their helpful effort in the present program.

Appendices

Symposium, Workshop, Seminar, PAC and External Review
CNS Reports
Publication List
Talks and Presentations
Personnel

Symposium, Workshop, Seminar, Colloquium, and PAC

A. Symposium and Workshop

(1) International OEDO Workshop
Jun. 11, 2018, CNS

B. CNS Seminar

(1) Fedor Simkovic (Comenius Univ, Bratislava / BLTP, JINR Dubna): "Massive neutrinos in nuclear processes", Mar. 5, 2019, Nishina Hall, RIKEN, Japan

(2) Ken'ichi Nakano (TIT): "Measurement of flavor asymmetry of light antiquarks in proton via Drell-Yan process at Fermilab SeaQuest", Jan. 29, 2019, Nishina Hall, RIKEN, Japan

(3) Afanasjev Anatoli (Mississipi State Univ.): "Covariant density functional theoretical studies across the nuclear landscape", Dec. 13, 2018, Nishina Hall, RIKEN, Japan

(4) Christian Smorra (CERN): "High-precision measurements of the antiproton's fundamental properties", Dec. 12, 2018, Nishina Hall, RIKEN, Japan

(5) Marco Mazzocco (Univ. of Padova / INFN): "Reaction Dynamics Studies with Light Weakly-Bound Radioactive Ion Beams at Near-Barrier Energies", Dec. 10, 2018, Nishina Hall, RIKEN, Japan

C. Program Advisory Committee for Nuclear-Physics Experiments at RI Beam Factory

(1) The 19th NP-PAC meeting
Date: November 29-December 1, 2018
Place: RIBF Conference Hall on the 2nd floor of the RIBF Building

CNS Reports

#97 "CNS Annual Report 2017"
Edited by T. Gunji, and Y. Kishi March, 2018

Publication List

A. Original Papers

(1) T. Nishi, K. Itahashi, G. P. A. Berg, H. Fujioka, N. Fukuda, N. Fukunishi, H. Geissel, R. S. Hayano, S. Hirenzaki, K. Ichikawa, N. Ikeno, N. Inabe, S. Itoh, M. Iwasaki, D. Kameda, S. Kawase, T. Kubo, K. Kusaka, H. Matsubara, S. Michimasa, K. Miki, G. Mishima, H. Miya, H. Nagahiro, M. Nakamura, S. Noji, K. Okochi, S. Ota, N. Sakamoto, K. Suzuki, H. Takeda, YK. Tanaka, K. Todoroki, K. Tsukada, T. Uesaka, Y. N. Watanabe, H. Weick, H. Yamakami, K. Yoshida, "Spectroscopy of Pionic Atoms in ^{122}Sn(d,^{3}He) Reaction and Angular Dependence of the Formation Cross Sections", Phys. Rev. Lett. **120**, 152505 (2018).

(2) M. L. Cortes, P. Doornenbal, M. Dupuis, S. M. Lenzi, F. Nowacki, A. Obertelli, S. Peru, N. Pietralla, V. Werner, K. Wimmer, G. Authelet, H. Baba, D. Calvet, F. Chateau, A. Corsi, A. Delbart, JM. Gheller, A. Gillibert, T. Isobe, V. Lapoux, C. Louchart, M. Matsushita, S. Momiyama, T. Motobayashi, M. Niikura, H. Otsu, C. Peron, A. Peyaud, E. C. Pollacco, J. Y. Rousse, H. Sakurai, C. Santamaria, M. Sasano, Y. Shiga, S. Takeuchi, R. Taniuchi, T. Uesaka, H. Wang, K. Yoneda, F. Browne, L. X. Chung, Z. Dombradi, S. Franchoo, F. Giacoppo, A. Gottardo, K. Hadynska-Klek, Z. Korkulu, S. Koyama, Y. Kubota, J. Lee, M. Lettmann, R. Lozeva, K. Matsui, T. Miyazaki, S. Nishimura, L. Olivier, S. Ota, Z. Patel, E. Sahin, C. M. Shand, P.-A. Soderstrom, I. Stefan, D. Steppenbeck, T. Sumikama, D. Suzuki, Z. Vajta, J. Wu, Z. Xu, "Inelastic scattering of neutron-rich Ni and Zn isotopes off a proton target", Phys. Rev. C **97**, 044315 (2018).

(3) A. Corsi, A. Obertelli, P. Doornenbal, F. Nowacki, H. Sagawa, Y. Tanimura, N. Aoi, H. Baba, P. Bednarczyk, S. Boissinot, M. Ciemala, A. Gillibert, T. Isobe, A. Jungclaus, V. Lapoux, J. Lee, K. Matsui, M. Matsushita, T. Motobayashi, D. Nishimura, S. Ota, E. Pollacco, H. Sakurai, C. Santamaria, Y. Shiga, D. Sohler, D. Steppenbeck, S. Takeuchi, R. Taniuchi, H. Wang, "Spectroscopy of nuclei around ^{100}Sn populated via two-neutron knockout reactions", Phys. Rev. C **97**, 044321 (2018).

(4) R. Yokoyama, E. Ideguchi, G. S. Simpson, Mn. Tanaka, S. Nishimura, P. Doornenbal, G. Lorusso, P.A. Soderstrom, T. Sumikama, J. Wu, Z. Y. Xu, N. Aoi, H. Baba, F. L. B. Garrote, G. Benzoni, F. Browne, R. Daido, Y. Fang, N. Fukuda, A. Gottardo, G. Gey, S. Go, N. Inabe, T. Isobe, D. Kameda, K. Kobayashi, M. Kobayashi, I. Kojouharov, T. Komatsubara, T. Kubo, N. Kurz, I. Kuti, Z. Li, M. Matsushita, S. Michimasa, C. B. Moon, H. Nishibata, I. Nishizuka, A. Odahara, Z. Patel, S. Rice, E. Sahin, H. Sakurai, H. Schaffner, L. Sinclair, H. Suzuki, H. Takeda, J. Taprogge, Z. Vajta, H.Watanabe, A. Yagi, T. Inakura, "Beta-gamma spectroscopy of the neutron-rich ^{150}Ba", Prog. Theor. Exp. Phys. **2018**, 041D02 (2018).

(5) S. Noji, H. Sakai, N. Aoi, H. Baba, G. P. A. Berg, P. Doornenbal, M. Dozono, N. Fukuda, N. Inabe, D. Kameda, T. Kawabata, S. Kawase, Y. Kikuchi, K. Kisamori, T. Kubo, Y. Maeda, H. Matsubara, S. Michimasa, K. Miki, H. Miya, H. Miyasako, S. Sakaguchi, Y. Sasamoto, S. Shimoura, M. Takaki, H. Takeda, S. Takeuchi, H. Tokieda, T. Ohnishi, S. Ota, T. Uesaka, H. Wang, K. Yako, Y. Yanagisawa, N. Yokota, K. Yoshida, R. G. T. Zegers, "Excitation of the Isovector Spin Monopole Resonance via the Exothermic ^{90}Zr(^{12}N,^{12}C) Reaction at 175 MeV/u", Phys. Rev. Lett. **120**, 172501 (2018).

(6) S. Chebotaryov, S. Sakaguchi, T. Uesaka, T. Akieda, Y. Ando, M. Assie, D. Beaumel, N. Chiga, M. Dozono, A. Galindo-Uribarri, B. Heffron, A. Hirayama, T. Isobe, K. Kaki, S. Kawase, W. Kim, T. Kobayashi, H. Kon, Y. Kondo, Y. Kubota, S. Leblond, H. Lee, T. Lokotko, Y. Maeda, Y. Matsuda, K. Miki, E. Milman, T. Motobayashi, T. Mukai, S. Nakai, T. Nakamura, A. Ni, T. Noro, S. Ota, H. Otsu, T. Ozaki, V. Panin, S. Park, A. Saito, H. Sakai, M. Sasano, H. Sato, K. Sekiguchi, Y. Shimizu, I. Stefan, L. Stuhl, M. Takaki, K. Taniue, K. Tateishi, S. Terashima, Y. Togano, T. Tomai, Y. Wada, T. Wakasa, T. Wakui, A. Watanabe, H. Yamada, Z. Yang, M. Yasuda, J. Yasuda, K. Yoneda, J. Zenihiro, "Proton elastic scattering at 200 AMeV and high momentum transfers of 1.7-2.7 fm^{-1} as a probe of the nuclear matter density of ^{6}He", Prog. Theor. Exp. Phys. **2018**, 053D01 (2018).

(7) A. M. Long, T. Adachi, M. Beard, G. P. A. Berg, M. Couder, R. J. de Boer, M. Dozono, J. Gorres, H. Fujita, Y. Fujita, K. Hatanaka, D. Ishikawa, T. Kubo, H. Matsubara, Y. Namiki, S. O'Brien, Y. Ohkuma, H. Okamura, H. J. Ong, D. Patel, Y. Sakemi, Y. Shimbara, S. Suzuki, R. Talwar, A. Tamii, A. Volya, T. Wakasa, R. Watanabe, M. Wiescher, R. Yamada, J. Zenihiro, "α-unbound levels in ^{34}Ar from ^{36}Ar$(p,t)^{34}$Ar reaction measurements and implications for the astrophysical ^{30}S$(\alpha,p)^{33}$Cl reaction rate", Phys. Rev. C **97**, 054613 (2018).

(8) S. Michimasa, M. Kobayashi, Y. Kiyokawa, S. Ota, D. S. Ahn, H. Baba, GPA. Berg, M. Dozono, N. Fukuda, T. Furuno, E. Ideguchi, N. Inabe, T. Kawabata, S. Kawase, K. Kisamori, K. Kobayashi, T. Kubo, Y. Kubota, C. S. Lee, M. Matsushita, H. Miya, A. Mizukami, H. Nagakura, D. Nishimura, H. Oikawa, H. Sakai, Y. Shimizu, A. Stolz, H. Suzuki, M. Takaki, H. Takeda, S. Takeuchi, H. Tokieda, T. Uesaka, K. Yako, Y. Yamaguchi, Y. Yanagisawa, R. Yokoyama, K. Yoshida, S. Shimoura, "Magic Nature of Neutrons in $^{54}Ca^{-54}$: First Mass Measurements of $^{55-57}Ca$", Phys. Rev. Lett. **121**, 022506 (2018).

(9) X. Y. Liu, Z. Liu, B. Ding, R. Doornenbal, A. Obertelli, S. M. Lenzi, P. M. Walker, L. X. Chung, B. D. Linh, G. Authelet, H. Baba, D. Calvet, F. Chateau, A. Corsi, A. Delbart, J. M. Gheller, A. Gillibert, T. Isobe, V. Lapoux, M. Matsushita, S. Momiyama, T. Motobayashi, M. Niikura, F. Nowacki, H. Otsu, C. Peron, A. Peyaud, EC. Pollacco, JY. Rousse, H. Sakurai, M. Sasano, Y. Shiga, S. Takeuchi, R. Taniuchi, T. Uesaka, H. Wang, K. Yoneda, Y. H. Lam, T. H. Huang, M. D. Sun, W. Q. Zhang, H. Y. Lu, D. S. Hou, E. Browne, Z. Dombradi, S. Franchoo, F. Giacoppo, A. Gottardo, K. Hadynska-Klek, Z. Korkulu, S. Koyama, Y. Kubota, J. Lee, M. Lettmann, R. Lozeva, K. Matsui, T. Miyazaki, S. Nishimura, C. Louchart, L. Olivier, S. Ota, Z. Patel, E. Sahin, C. Santamaria, C. Shand, P.A. Soderstrom, G. L. Stefan, D. Steppenbeck, T. Sumikama, D. Suzuki, Z. Vajta, V. Werner, J. Wu, Z. Xu, X. H. Zhou, Y. H. Zhang, H. S. Xu, F. S. Zhang, "Spectroscopy of $^{65,67}_{25}Mn$: Strong coupling in the N=40 island of inversion", Phys. Lett. B **784**, 392-396 (2018).

(10) J. Yasuda, M. Sasano, R. G. T. Zegers, H. Baba, D. Bazin, W. Chao, M. Dozono, N. Fukuda, N. Inabe, T. Isobe, G. Jhang, D. Kameda, M. Kaneko, K. Kisamori, M. Kobayashi, N. Kobayashi, T. Kobayashi, S. Koyama, Y. Kondo, A. J. Krasznahorkay, T. Kubo, Y. Kubota, M. Kurata-Nishimura, C. S. Lee, J. W. Lee, Y. Matsuda, E. Milman, S. Michimasa, T. Motobayashi, D. Muecher, T. Murakami, T. Nakamura, N. Nakatsuka, S. Ota, H. Otsu, V. Panin, W. Powell, S. Reichert, S. Sakaguchi, H. Sakai, M. Sako, H. Sato, Y. Shimizu, M. Shikata, S. Shimoura, L. Stuhl, T. Sumikama, H. Suzuki, S. Tangwancharoen, M. Takaki, H. Takeda, T. Tako, Y. Togano, H. Tokieda, J. Tsubota, T. Uesaka, T. Wakasa, K. Yako, K. Yoneda, J. Zenihiro, "Extraction of the Landau-Migdal Parameter from the Gamow-Teller Giant Resonance in ^{132}Sn", Phys. Rev. Lett. **121**, 132501 (2018).

(11) C. Santamaria, A. Obertelli, S. Ota, M. Sasano, E. Takada, L. Audirac, H. Baba, D. Calvet, F. Chateau, A. Corsi, A. Delbart, P. Doornenbal, A. Giganon, A. Gillibert, Y. Kondo, Y. Kubota, C. Lahonde-Hamdoun, V. Lapoux, D. Leboeuf, CS. Lee, H. N. Liu, M. Matsushita, T. Motobayashi, M. Niikura, M. Kurata-Nishimura, H. Otsu, A. Peyaud, EC. Pollacco, G. Prono, H. Tokieda, T. Uesaka, J. Zenihiro, "Tracking with the MINOS Time Projection Chamber", Nucl. Instrum. Methods Phys., Res. Sect. A **905**, 138-148 (2018).

(12) S. Shimoura, "Direct reactions as quantum probes for nuclei", Eur. Phys. J. Plus **133**, 463 (2018).

(13) O. Wieland, A. Bracco, F. Camera, R. Avigo, H. Baba, N. Nakatsuka, T. Aumann, SR. Banerjee, G. Benzoni, K. Boretzky, C. Caesar, S. Ceruti, S. Chen, FCL. Crespi, V. Derya, P. Doornenbal, N. Fukuda, A. Giaz, K. Ieki, N. Kobayashi, Y. Kondo, S. Koyama, T. Kubo, M. Matsushita, B. Million, T. Motobayashi, T. Nakamura, M. Nishimura, H. Otsu, T. Ozaki, A. T. Saito, H. Sakurai, H. Scheit, F. Schindler, P. Schrock, Y. Shiga, M. Shikata, S. Shimoura, D. Steppenbeck, T. Sumikama, S. Takeuchi, R. Taniuchi, Y. Togano, J. Tscheuschner, J. Tsubota, H. Wang, K. Wimmer, K. Yoneda, "Low-lying dipole response in the unstable ^{70}Ni nucleus", Phys. Rev. C **98**, 064313 (2018).

(14) Y. Kubota, M. Sasano, T. Uesaka, M. Dozono, M. Itoh, S. Kawase, M. Kobayashi, C. S. Lee, H. Matsubara, K. Miki, H. Miya, Y. Ono, S. Ota, K. Sekiguchi, T. Shima, T. Taguchi, T. L. Tang, H. Tokieda, T. Wakasa, T. Wakui, J. Yasuda, J. Zenihiro, "Development of a neutron detector with a high position resolution at intermediate energies", Nucl. Instrum. Methods Phys. Res., Sect. A **914**, 32-41 (2019).

(15) S. Takeuchi, T. Nakamura, M. Shikata, Y. Togano, Y. Kondo, J. Tsubota, T. Ozaki, A. Saito, H. Otsu, H. Wang, H. Sakurai, Y. Watanabe, S. Kawase, D. Ahn, M. Aikawa, T. Ando, S. Araki, S. Chen, N. Chiga, P. Doornenbal, S. Ebata, N. Fukuda, T. Isobe, S. Kawakami, T. Kin, S. Koyama, S. Kubono, Y. Maeda, A. Makinaga, M. Matsushita, T. Matsuzaki, S. Michimasa, S. Momiyama, S. Nagamine, K. Nakano, M. Niikura, K. Ogata, T. Saito, Y. Shiga, Y. Shimizu, S. Shimoura, T. Sumikama, P. A. Soderstrom, H. Suzuki, H. Takeda, R. Taniuchi, M. Uesaka, Y. Watanabe, K. Wimmer, T. Yamamoto, K. Yoshida, "Coulomb breakup reactions of $^{93-94}Zr$ in inverse kinematics", Prog. Theor. Exp. Phys. **2019**, 013D02 (2019).

(16) Z. Elekes, A. Kripko, D. Sohler, K. Sieja, K. Ogata, K. Yoshida, P. Doornenbal, A. Obertelli, G. Authelet, H. Baba, D. Calvet, F. Chateau, A. Corsi, A. Delbart, JM. Gheller, A. Gillibert, T. Isobe, V. Lapoux, M. Matsushita, S. Momiyama, T. Motobayashi, H. Otsu, C. Peron, A. Peyaud, EC. Pollacco, JY. Rousse, H. Sakurai, C. Santamaria,

Y. Shiga, S. Takeuchi, R. Taniuchi, T. Uesaka, H. Wang, K. Yoneda, F. Browne, LX. Chung, Z. Dombradi, F. Flavigny, S. Franchoo, F. Giacoppo, A. Gottardo, K. Hadynska-Klek, Z. Korkulu, S. Koyama, Y. Kubota, J. Lee, M. Lettmann, C. Louchart, R. Lozeva, K. Matsui, T. Miyazaki, M. Niikura, S. Nishimura, L. Olivier, S. Ota, Z. Patel, E. Sahin, C. Shand, PA. Soderstrom, I. Stefan, D. Steppenbeck, T. Sumikama, D. Suzuki, Z. Vajta, V. Werner, J. Wu, Z. Xu, "Nuclear structure of ^{76}Ni from the $(p,2p)$ reaction", Phys. Rev. C **99**, 014312 (2019).

(17) L. Stuhl et al., "Study of the Gamow-Teller transitions in 6He with PANDORA system (17H391)", 2017 Annual Report of the Research Project with Heavy Ions at NIRS-HIMAC, (2018).

(18) S. Acharya et al. [ALICE Collaboration], "Longitudinal asymmetry and its effect on pseudorapidity distributions in Pb - Pb collisions at $\sqrt{sNN} = 2.76$ TeV", Phys. Lett. B **781**, 20 (2018).

(19) S. Acharya et al. [ALICE Collaboration], "First measurement of Ξ_c^0 production in pp collisions at $\sqrt{s} = 7$ TeV", Phys. Lett. B **781**, 8 (2018).

(20) S. Acharya et al. [ALICE Collaboration], "Λ_c^+ production in pp collisions at $\sqrt{s} = 7$ TeV and in p-Pb collisions at $\sqrt{sNN} = 5.02$ TeV", JHEP **04**, 108 (2018).

(21) S. Acharya et al. [ALICE Collaboration], "Prompt and non-prompt J/ψ production and nuclear modification at mid-rapidity in p - Pb collisions at $\sqrt{sNN = 5.02}$ TeV", Eur. Phys. J. C **78**, 466 (2018).

(22) S. Acharya et al. [ALICE Collaboration], "Constraints on jet quenching in p-Pb collisions at $\sqrt{sNN}$ =5.02 TeV measured by the event-activity dependence of semi-inclusive hadron-jet distributions", Phys. Lett. B **783**, 95 (2018).

(23) S. Acharya et al. [ALICE Collaboration], "Measurement of the inclusive J/ψ polarization at forward rapidity in pp collisions at $\sqrt{s} = 8$ TeV", Eur. Phys. J. C **78**, 562 (2018).

(24) S. Acharya et al. [ALICE Collaboration], "ϕ meson production at forward rapidity in Pb-Pb collisions at $\sqrt{sNN} =$ 2.76 TeV", Eur. Phys. J. C **78**, 559 (2018).

(25) S. Acharya et al. [ALICE Collaboration], "Energy dependence and fluctuations of anisotropic flow in Pb-Pb collisions at $\sqrt{sNN}$ =5.02 and 2.76 TeV", JHEP **07**, 103 (2018).

(26) S. Acharya et al. [ALICE Collaboration], "Inclusive J/ψ production at forward and backward rapidity in p-Pb collisions at $\sqrt{sNN} = 8.16$ TeV", JHEP **07**, 160 (2018).

(27) S. Acharya et al. [ALICE Collaboration], "Anisotropic flow in Xe-Xe collisions at $\sqrt{sNN} = 5.44$ TeV", Phys. Lett. B **784**, 82 (2018).

(28) S. Acharya et al. [ALICE Collaboration], "Neutral pion and η meson production in p-Pb collisions at $\sqrt{sNN} = 5.02$ TeV", Eur. Phys. J. C **78**, 624 (2018).

(29) S. Acharya et al. [ALICE Collaboration], "Inclusive J/ψ production in Xe-Xe collisions at $\sqrt{sNN} = 5.44$ TeV", Phys. Lett. B **785**, 419 (2018).

(30) S. Acharya et al. [ALICE Collaboration], "Anisotropic flow of identified particles in Pb-Pb collisions at $\sqrt{sNN} =$ 5.02 TeV", JHEP **09**, 006 (2018).

(31) S. Acharya et al. [ALICE Collaboration], "Azimuthally-differential pion femtoscopy relative to the third harmonic event plane in Pb-Pb collisions at $\sqrt{sNN} = 2.76$ TeV", Phys. Lett. B **785**, 320 (2018).

(32) S. Acharya et al. [ALICE Collaboration], "Dielectron production in proton-proton collisions at $\sqrt{s} = 7$ TeV", JHEP **1809**, 064 (2018).

(33) S. Acharya et al. [ALICE Collaboration], "Neutral pion and η meson production at midrapidity in Pb-Pb collisions at $\sqrt{sNN} = 2.76$ TeV", Phys. Rev. C **98**, 044901 (2018).

(34) S. Acharya et al. [ALICE Collaboration], " Medium modification of the shape of small-radius jets in central collisions at $\sqrt{sNN} = 2.76$ TeV", JHEP **1810**, 139 (2018).

(35) S. Acharya et al. [ALICE Collaboration], "Transverse momentum spectra and nuclear modification factors of charged particle in pp, p-Pb and Pb-Pb collisions at the LHC", JHEP **1811**, 013 (2018).

(36) S. Acharya et al. [ALICE Collaboration], ”Transverse momentum spectra and nuclear modification factors of charged particles in Xe-Xe collisions at $\sqrt{sNN} = 5.44$ TeV”, Phys. Lett. B **788** 166 (2019).

(37) S. Acharya et al. [ALICE Collaboration], ”Measuring $K_s0K\pm$ interaction using pp collisions $\sqrt{s} = 7$ TeV”, Phys. Lett. B **790** 22 (2019).

(38) S. Acharya et al. [ALICE Collaboration], ”Y suppression at forward rapidity in Pb-Pb collisions at $\sqrt{sNN} = 5.02$ TeV”, Phys. Lett. B **790** 89 (2019).

(39) S. Acharya et al. [ALICE Collaboration], ”Direct photon elliptic flow in Pb-Pb collisions at $\sqrt{sNN} = 2.76$ TeV”, Phys. Lett. B **789**, 308 (2019).

(40) S. Acharya et al. [ALICE Collaboration], ”Charged jet cross section and fragmentation in proton-proton collisions at $\sqrt{s} = 2.76$ and 8 TeV”, Phys. Rev. D **99**, 012016 (2019).

(41) S. Acharya et al. [ALICE Collaboration], ”Dielectron and heavy-quark production in inelastic and high-multiplicity proton-proton collisions at $\sqrt{s} = 13$ TeV”, Phys. Lett. B **788**, 505 (2019).

(42) S. Acharya et al. [ALICE Collaboration], ”Suppression of $\Lambda(1520)$ resonance production in central Pb-Pb collisions at $\sqrt{sNN} = 2.76$ TeV”, Phys. Rev. C **99**, 024905 (2019).

(43) S. Acharya et al. [ALICE Collaboration], ”$p-p$, $p-\Lambda$ and $\Lambda-\Lambda$ correlation studied via femtoscopy in pp reactions at $\sqrt{s} = 7$ TeV”, Phys. Rev. C **99**, 024001 (2019).

(44) S. Acharya et al. [ALICE Collaboration], ”Measurement of dielectron production in central Pb-Pb collisions at $\sqrt{sNN} = 2.76$ TeV”, Phys. Rev. C **99**, 024002 (2019).

(45) S. Acharya et al. [ALICE Collaboration], ”Event-shape engineering for the D-meson elliptic flow in mid-central Pb-Pb collisions at $\sqrt{sNN} = 5.02$ TeV”, JHEP **02**, 150 (2019).

(46) S. Acharya et al. [ALICE Collaboration], ”Azimuthal anisotropy of heavy-flavor decay electrons in p-Pb collisions at $\sqrt{sNN} = 5.02$ TeV”, Phys. Rev. Lett. **122**, 072301 (2019).

(47) S. Acharya et al. [ALICE Collaboration], ”Centrality and pseudorapidity dependence of charged-particle multiplicity density in Xe-Xe collisions at $\sqrt{sNN} = 5.02$ TeV”, Phys. Lett. B **790**, 35 (2019).

(48) N.N. Duy, K.Y. Chae, S.M. Cha, H. Yamaguchi, K. Abe, S.H. Bae, D.N. Binh, S.H. Choi, K.I. Hahn, S. Hayakawa, B. Hong, N. Iwasa, D. Kahl, L.H. Khiem, A. Kim, D.H. Kim, E.J. Kim, G.W. Kim, M.J. Kim, K. Kwak, M.S. Kwak, E.J. Lee, S.I. Lim, B. Moon, J.Y. Moon, S.Y. Park, V.H. Phong, H. Shimizu, L. Yang, Z. Ge, T.V.N. Hao, ”Beam production of ^{18}Ne with in-flight method for alpha scattering at CRIB”, Nuclear Inst. and Methods in Physics Research, A **897**, 8-13 (2018).

(49) D. Kim, G.W. Kim, S.Y. Park, A. Kim, K.I. Hahn, K. Abe, O. Beliuskina, S. Hayakawa, N. Imai, N. Kitamura, Y. Sakaguchi, H. Yamaguchi, S.M. Cha, K.Y. Chae, M.S. Kwag, S.W. Hong, E.J. Lee, J.H. Lee, E.K. Lee, J.Y. Moon, S.H. Bae, S.H. Choi, S. Kubono, V. Panin, Y. Wakabayashi, N. Iwasa, D. Kahl, A. A. Chen, ”Study of ^{19}F Levels with $E_x = 6.7-7.7$ MeV by the ^{15}N+αScattering Experiment”, Journal of the Korean Physical Society, **73**, 265-270 (2018).

(50) S.M. Cha, K.Y. Chae, M.J. Kim, M.S. Kwag, E.J. Lee, K. Abe, S. Hayakawa, H. Shimizu, H. Yamaguchi, L. Yang, S.H. Bae, S.H. Choi, D.N. Binh, N.N. Duy, Z. Ge, V.H. Phong, K.I. Hahn, B. Hong, B. Moon, N. Iwasa, D. Kahl, L.H. Khiem, A. Kim, D.H. Kim, G.W. Kim, S.I. Lim, S.Y. Park, E.J. Kim, K. Kwak, J.Y. Moon, ”Study of α-cluster Structure in ^{22}Mg Using a Radioactive Ion Beam”, Journal of the Korean Physical Society, **73**, 1055-1060 (2018).

(51) A. Uchiyama, K. Harada, K. Sakamoto, U. Dammalapati, T. Inoue, M. Itoh, S. Ito, H. Kawamura, K.S. Tanaka, R. Yoshioka, Y. Sakemi, ”Effective multiple sideband generation using an electro-optic modulator for a multiple isotope magneto-optical trap”, Rev. Sci. Instrum., **89**, 123111 (2018).

(52) A. Uchiyama, K. Harada, T. Inoue, H. Kawamura, K.S. Tanaka, M. Itoh, T. Aoki, A. Hatakeyama, Y. Takahashi, Y. Sakemi, ”Development of a Dual Isotope Co-Magnetometer Using Laser Cooled Rubidium Toward Electron Electric Dipole Moment Measurement Using Francium”, Journal of Physics: Conference Series, **1206**, 012008 (2019).

(53) 酒見泰寛, "冷却原子を用いた電子の電気双極子能率の探索", 光学（一般社団法人・日本光学会）, **47**, 301 (2018).

(54) 長濱弘季, "反陽子の基礎物理量の高精度測定", しょうとつ（原子衝突学会誌）, 第 15 巻 5 号, 91 (2018).

(55) S. Yoshida, N. Shimizu, T. Togashi, and T. Otsuka, "Uncertainty quantification in the nuclear shell model", Phys. Rev. C **98**, 061301(R) (2018).

(56) S. Yoshida, Y. Utsuno, N. Shimizu, and T. Otsuka, "Systematic shell-model study of beta-decay properties and Gamow-Teller strength distributions in $A \sim 40$ neutron-rich nuclei", Phys. Rev. C **97**, 054321 (2018).

(57) Md. S. R. Laskar, N. Shimizu, Y. Utsuno, "g-factor measurement of 2738 keV isomer in ^{135}La", Phys. Rev. C **99**, 014308 (2019).

(58) N. Shimizu, and T. Mizusaki, "Variational Monte Carlo method for shell-model calculations in odd-mass nuclei and restoration of symmetry", Phys. Rev. C **98**, 054309 (2018).

(59) T. Mizusaki, M. Oi, and N. Shimizu, "Why does the sign problem occur in evaluating the overlap of HFB wave functions?", Phys. Lett. B **779**, 237 (2018).

(60) J. Menendez, N. Shimizu and K. Yako, "Is it possible to study neutrinoless decay by measuring double Gamow-Teller transitions?", Conf. Ser. **1056**, 012307 (2018).

(61) X. F. Yang, Y. Tsunoda, T. Otsuka, "Investigating the large deformation of the 5/2+ isomeric state in ^{73}Zn: An indicator for triaxiality", Phys. Rev. C **97**, 044324 (2018).

(62) A. I. Morales, T. Otsuka, Y. Tsunoda, "Is seniority a partial dynamic symmetry in the first vg9/2 shell?", Phys. Lett. B **781**, 706 (2018).

(63) T. Togashi, Y. Tsunoda, T. Otsuka, N. Shimizu, and M. Honma, "Novel Shape Evolution in Sn Isotopes from Magic Numbers 50 to 82", Phys. Rev. Lett. **121**, 062501 (2018).

(64) B. A. Marsh, Y. Tsunoda, T. Otsuka, "Characterization of the shape-staggering effect in mercury nuclei", Nature Physics **14**, 1163 (2018).

(65) P. Singh, T. Otsuka, T. Togashi, Y. Tsunoda, "Evidence for Coexisting Shapes through Lifetime Measurements in ^{98}Zr", Phys. Rev. Lett. **121**, 192501 (2018).

(66) D. Rosiak, Y. Tsunoda, T. Togashi, T. Otsuka, "Enhanced Quadrupole and Octupole Strength in Doubly Magic ^{132}Sn", Phys. Rev. Lett. **121**, 252501 (2018).

(67) M. Stryjczyk, Y. Tsunoda, T. Otsuka, "β- decay study of the ^{66}Mn-^{66}Fe-^{66}Co-^{66}Ni decay chain", Phys. Rev. C **98**, 064326 (2018).

(68) Ł. W. Iskra, T. Otsuka, T. Togashi, Y. Tsunoda, et al. "Revised B(E3) transition rate and structure of the 3- level in ^{96}Zr", Phys. Lett. B **788**, 396 (2018).

(69) Y. Ichikawa, Y. Tsunoda, T. Otsuka, "Interplay between nuclear shell evolution and shape deformation revealed by magnetic moment of ^{75}Cu", Nature Physics **15**, 321 (2018).

(70) C. Loelius, T. Otsuka, N. Tsunoda, "Enhanced Electric Dipole Strength for the Weakly Bound States in ^{27}Ne", Phys. Rev. Lett. **121**, 262501 (2018).

(71) H. Nishibata, N. Tsunoda, and T. Otsuka, "Structure of ^{31}Mg: Shape coexistence revealed by $\beta - \gamma$ spectroscopy with spin-polarized ^{31}Na", Phys. Rev. C **99**, 024322 (2018).

B. Proceedings

(1) N. Imai, "Nuclear reaction data of low-energy LLFP produced by OEDO", Proceedings of the 2017 Symposium on Nuclear Data, JAEA-Conf2018-001, 39-44 (2018).

(2) M. La Commara, M. Mazzocco, A. Boiano, C. Boiano, C. Manea, C. Parascandolo, D. Pierroutsakou, C. Signorini, E. Strano, D. Torresi, H. Yamaguchi, D. Kahl, P. DiMeo, J. Grebosz, N. Imai, Y. Hirayama, H. Ishiyama, N. Iwasa, S.C. Jeong, H.M. Jia, Y.H. Kim, S. Kimura, S. Kubono, C.J. Lin, H. Miyatake, M. Mukai, T. Nakao, M. Nicoletto, Y. Sakaguchi, A.M. Sanchez-Benitez, F. Soramel, T. Teranishi, Y. Wakabayashi, Y.X. Watanabe, L. Yang, Y.Y. Yang, "$^{8}B+^{208}$Pb Elastic Scattering at Coulomb Barrier Energies", IOP Conf. Series: Journal of Physics: Conf. Series 966, 012010 (2018).

(3) D. Kahl, H. Shimizu, H. Yamaguchi, K. Abe, O. Beliuskina, S. M. Cha, K. Y. Chae, A. A. Chen, Z. Ge, S. Hayakawa, N. Imai, N. Iwasa, A. Kim, D. H. Kim, M. J. Kim, S. Kubono, M. S. Kwag, J. Liang, J. Y. Moon, S. Nishimura, S. Oka, S. Y. Park, A. Psaltis, T. Teranishi, Y. Ueno, L. Yang, "Impact of the ^{26m}Al(p,γ) reaction to galactic ^{26}Al yield", AIP Conference Proceedings 1947(1), 020003 (2018).

(4) S. Hayakawa, K. Abe, O. Beliuskina, S. M. Cha, K. Y. Chae, S. Cherubini, P. Figuera, Z. Ge, M. Gulino, J. Hu, A. Inoue, N. Iwasa, D. Kahl, A. Kim, D. H. Kim, G. Kiss, S. Kubono, M. L. Cognata, M. L. Commara, L. Lamia, M. Lattuada, E. J. Lee, J. Y. Moon, S. Palmerini, C. Parascandolo, S. Y. Park, D. Pierroutsakou, R. G. Pizzone, G. G. Rapisarda, S. Romano, H. Shimizu, C. Spitaleri, X. D. Tang, O. Trippella, A. Tumino, P. Vi, H. Yamaguchi, L. Yang, N. T. Zhang, "Measurements of the neutron-induced reactions on ^{7}Be with CRIB by the trojan horse method", AIP Conference Proceedings 1947(1), 020011 (2018).

(5) H. Yamaguchi, D. Kahl, S. Hayakawa, L. Yang, H. Shimizu, Y. Sakaguchi, K. Abe, Y. Wakabayashi, T. Hashimoto, T. Nakao, S. Kubono, T. Suhara, N. Iwasa, A. Kim, D. H. Kim, S. M. Cha, M. S. Kwag, J. H. Lee, E. J. Lee, K. Y. Chae, N. Imai, N. Kitamura, P. Lee, J. Y. Moon, K. B. Lee, C. Akers, H. S. Jung, N. N. Duy, L. H. Khiem, C. S. Lee, S. Cherubini, M. Gulino, C. Spitaleri, G. G. Rapisarda, M. L. Cognata, L. Lamia, S. Romano, A. Coc, N. de Sereville, F. Hammache, G. Kiss, S. Bishop, T. Teranishi, T. Kawabata, Y. K. Kwon, D. N. Binh, "Indirect studies on astrophysical reactions at the low-energy RI beam separator CRIB", AIP Conference Proceedings 1947(1), 020022 (2018).

(6) H. Yamaguchi, S. Hayakawa, L. Yang, H. Shimizu and D. Kahl, "Direct measurements and detection techniques with low-energy RIBs", EPJ Web Conf., 184, 01017 (2018).

(7) A. Inoue, A. Tamii, K. Abe, S. Adachi, N. Aoi, M. Asai, M. Fukuda, G. Gey, T. Hashimoto, E. Ideguchi, J. Isaak, N. Kobayashi, Y. Maeda, H. Makii, K. Matsuta, M. Mihara, M. Miura, T. Shima, H. Shimizu, R. Tang, T. Dinh Trong, H. Yamaguchi and L. Yang, "Study of the contribution of the ^{7}Be(d,p) reaction to the ^{7}Li problem in the Big-Bang Nucleosynthesis", EPJ Web Conf., 184, 02007 (2018).

(8) H. Shimizu, D. Kahl, H. Yamaguchi, K. Abe, O. Beliuskina, S. M. Cha, K. Y. Chae, A. A. Chen, Z. Ge, S. Hayakawa, N. Imai, N. Iwasa, A. Kim, D. H. Kim, M. J. Kim, S. Kubono, M. S. Kawag, J. Liang, J. Y. Moon, S. Nishimura, S. Oka, S. Y. Park, A. Psaltis, T. Teranishi, Y. Ueno and L. Yang, "Isomeric ^{26}Al beam production with CRIB", EPJ Web Conf., 184, 02013 (2018).

(9) M. Gulino, S. Cherubini, G.G. Rapisarda, S. Kubono, L. Lamia, M.L. Cognata, R.G. Pizzone, H. Yamaguchi, S. Hayakawa, Y. Wakabayashi, N. Iwasa, S. Kato, T. Komatsubara, T. Teranishi, A. Coc, N. Sereville, F. Hammache, G. Kiss, S. Bishop, D.N. Binh, B. Roeder, L. Trache, R. Tribble, R. Sparta, I. Indelicato and C. Spitaleri, "Trojan Horse Method experiments with radioactive ion beams", EPJ Web Conf., 184, 01008 (2018).

(10) E. Strano, M. Mazzocco, A. Boiano, C. Boiano, M. La Commara, C. Manea, C. Parascandolo, D. Pierroutsakou, C. Signorini, D. Torresi, H. Yamaguchi, D. Kahl, L. Acosta, P. Di Meo, J.P. Fernandez-Garcia, T. Glodariu, J. Grebosz, A. Guglielmetti, N. Imai, Y. Hirayama, H. Ishiyama, N. Iwasa, S.C. Jeong, H.M. Jia, N. Keeley, Y.H. Kim, S. Kimura, S. Kubono, J.A. Lay, C.J. Lin, G. Marquinez-Duran, I. Marte, H. Miyatake, M. Mukai, T. Nakao, M. Nicoletto, A. Pakou, K. Rusek, Y. Sakaguchi, A.M. Sanchez-Benitez, T. Sava, O. Sgouros, C. Stefanini, F. Soramel, V. Soukeras, E. Stiliaris, L. Stroe, T. Teranishi, N. Toniolo, Y. Wakabayashi, Y.X. Watanabe, L. Yang and Y.Y. Yang, "^{7}Be and ^{8}B reaction dynamics at Coulomb barrier energies", EPJ Web Conf., 184, 02015 (2018).

(11) M. Mazzocco, A. Boiano, C. Boiano, M. La Commara, C. Manea, C. Parascandolo, D. Pierroutsakou, C. Signorini, E. Strano, D. Torresi, H. Yamaguchi, D. Kahl, L. Acosta, P. Di Meo, J.P. Fernandez-Garcia, T. Glodariu, J. Grebosz, A. Guglielmetti, N. Imai, Y. Hirayama, H. Ishiyama, N. Iwasa, S.C. Jeong, H.M. Jia, N. Keeley, Y.H. Kim, S. Kimura, S. Kubono, J.A. Lay, C.J. Lin, G. Marquinez-Duran, I. Marte, H. Miyatake, M. Mukai, T. Nakao, M. Nicoletto, A. Pakou, K. Rusek, Y. Sakaguchi, A.M. Sanchez-Benitez, T. Sava, O. Sgouros, F. Soramel, V. Soukeras, E. Stiliaris, L. Stroe, T. Teranishi, N. Toniolo, Y. Wakabayashi, Y.X. Watanabe, L. Yang and Y.Y. Yang, Reaction Dynamics for the Systems "^{7}Be, ^{8}B + ^{208}Pb at Coulomb Barrier Energies", IOP Conf. Series: Journal of Physics: Conf. Series 1078, 012013 (2018).

(12) N. Tsunoda, T. Otsuka, N. Shimizu, "Structure of exotic nuclei based on nuclear force", Proceedings of the Ito International Research Center Symposium "Perspectives of the Physics of Nuclear Structure", 23, 012014. (2018).

(13) T. Abe, "Advances in the Monte Carlo Shell Model for Understanding Nuclear Structure", JPS Conf. Proc. 23, 012009 (2018).

(14) J. Menéndez, "Towards Reliable Nuclear Matrix Elements for Neutrinoless $\beta\beta$ Decay", Proceedings of the "Symposium on Perspectives of the Physics of Nuclear Structure", JPS Conf. Proc. 23, 012036 (2018).

(15) T. Miyagi, T. Abe, M. Kohno, P. Navrátil, R. Okamoto, T. Otsuka, N. Shimizu, S.R. Stroberg, "Nuclear Ab Initio Calculations with the Unitary-Model-Operator Approach", JPS Conf. Proc. 23, 013007 (2018).

C. Theses

(1) R. Tsunoda: "Search for decays from IARs of ^{119}Sn to the excited states in the shape-coexistence nucleus ^{118}Sn": Master Thesis, the University of Tokyo. March 2019.

Talks and Presentations

A. Conferences

(1) S. Shimoura (Invited): "Tetra-neutron and few-body correlations studied by RI-beam experiments", New Frontiers in Nuclear Physics and Astrophysics (NNPA), May 28-June 1, 2018, Antalya, Turkey.

(2) S. Shimoura (Invited): "Tetraneutron system populated by double-charge exchange reactions using RI beam", The 13th International Conference on Hypernuclear and Strange Particle Physics (HYP2018), June 24-29, Portsmouth, Virginia, USA.

(3) S. Shimoura (Invited): "Tetra-neutron system populated by RI-beam induced reactions", The 22nd International Conference on Few-Body Problems in Physics (FB22), 9-13 July, 2018, Caen, France.

(4) S. Shimoura (Invited): "Nuclear Reaction Data for Long-Lived Fission Products", ImPACT International Symposium on "New Horizons of Partitioning and Transmutation Technologies with Accelerator System", 2-3 December 2018, The University of Tokyo.

(5) S. Shimoura (Invited): "Tetra-neutron system populated by exothermic double-charge exchange reaction", 13th International Conference on Nucleus-Nucleus Collisions (NN2018), Dec. 4-8, 2018, Omiya, Saitama.

(6) N. Imai (Invited): "Experimental studies with the energy-degraded RI beams", 20th Northeastern Asia symposium, Sept. 19, 2018, Nagoya, Japan.

(7) S. Michimasa (Invited): "Overview of OEDO", International OEDO Workshop 2018, June 11, 2018, Wako, Japan.

(8) M. Dozono (Invited): "Status report of ImPACT17-02-01/02", International OEDO Workshop 2018, June 11, 2018, Wako, Japan.

(9) N. Imai (Oral): "Measurement of $^{77,79}\mathrm{Se}(d,p)$ reactions in inverse kinematics at OEDO", The 10th international conference on Direct Reaction with Exotic Beams (DREB2018), June 4-8, 2018, Matsue, Japan.

(10) S. Michimasa (Oral): "New energy-degrading beam line for in-flight RI beams, OEDO", The International Conference on Electromagnetic Isotope Separators and Related Topics (EMIS), Sept. 16-21, 2018, CERN Geneva, Switzerland.

(11) S. Michimasa (Oral): "Construction of Low-energy RI Beam Line at RIBF and Nuclear Reaction Data on Low-energy LLFPs", Fifteenth NEA Information Exchange Meeting on Actinide and Fission Product Partitioning and Transmutation, Sept. 30-Oct. 3, 2018, Manchester Hall, Manchester, UK.

(12) S. Michimasa (Invited): "Recent Achievements using OEDO-SHARAQ at RIBF", The 10th China-Japan Joint Nuclear Physics Symposium (CJNP2018), Nov. 18-23, 2018, Sheraton Bailuhu Resort Hotel, Houzhou, China.

(13) S. Ota (Invited): "Active target technique with medium-energy high-intensity heavy-ion beams", The 10th China-Japan Joint Nuclear Physics Symposium (CJNP2018), Nov. 18-23, 2018, Sheraton Bailuhu Resort Hotel, Huizhou, China.

(14) L. Stuhl (Oral): "Study of spin-isospin responses of radioactive nuclei with background free neutron spectrometer, PANDORA International Conference on Electromagnetic Isotope Separators and Related Topics (EMIS2018)", Sep. 16–21, 2018, CERN, Geneva, Switzerland.

(15) L. Stuhl (Invited): "Detector development for (p,n) measurements at RIKEN RIBF", Nuclear Physics In Stellar Explosions Workshop, Sep. 12–14, 2018, Debrecen, Hungary.

(16) L. Stuhl (Oral): "Overview of campaign type experiments at SAMURAI — The ^{18}O campaign", SAMURAI International Workshop 2018, RIKEN Nishina Center, Sep. 3–4, 2018, Wako, Japan.

(17) L. Stuhl (Oral): "Status of (p,n) measurements at SAMURAI", SAMURAI International Workshop 2018, RIKEN Nishina Center, Sep. 3–4, 2018, Wako, Japan.

(18) L. Stuhl (Oral): "Study of spin-isospin responses of light nuclei along the drip line with PANDORA", The 10th international conference on Direct Reactions with Exotic Beams (DREB2018), Jun. 4–8, 2018, Matsue, Japan.

(19) S. Ota (Oral): "Giant resonances in Tin-region nuclei", 6th International Conference on Collective Motion in Nuclei under Extreme Conditions, Oct. 29-Nov. 2, 2018, Cape town, South Africa.

(20) Y. Sekiguchi (Oral): "Long-range two-particle correlations", Second internal workshop on Collectivity in Small Collision Systems (CSCS2018), Jun. 13-15, 2018, Wuhan, China.

(21) S. Hayashi for the ALICE Collaboration (Oral): "J/ψ production in p-Pb collisions with the ALICE detector", The 7th Asian Triangle Heavy Ion Conference (ATHIC2018), Nov. 3-6, 2018, Hefei, China.

(22) Y. Sekiguchi for the ALICE Collaboration (Oral): "Two-particle correlations with ALICE", The 7th Asian Triangle Heavy Ion Conference (ATHIC2018), Nov. 3-6, 2018, Hefei, China.

(23) S. Hayashi for the ALICE Collaboration (Oral): "Quarkonium production in pp, pA, and AA collisions", Quark and Nuclear Physics 2018 (QNP2018), Nov. 13-17, 2018, Tsukuba, Japan.

(24) T. Gunji (Oral): "Extension of Forward Physics beyond 2030", International workshop on Forward Physics and Forward Calorimeter upgrade in ALICE, Mar. 7-9, 2019, Tsukuba, Japan.

(25) L. Yang (Oral): "Reaction mechanisms of ^{17}F+^{58}Ni at energies around the Coulomb barrier", DREB2018, Jun. 4 8, 2018, Kunibiki Messe, Matsue, Shimane, Japan.

(26) H. Yamaguchi (Oral): "Study on explosive nuclear synthesis with low-energy RI beams at CRIB", 15th International Symposium on Nuclei in the Cosmos, Jun. 24-29, 2018, LNGS, Assergi, Italy.

(27) S. Hayakawa (Oral): "Cross section measurements of the $^{7}\mathrm{Be}(n,p)^{7}\mathrm{Li}$ and the $^{7}\mathrm{Be}(n,\alpha)^{4}\mathrm{He}$ reactions covering the Big-Bang nucleosynthesis energy range by the Trojan Horse method at CRIB", 15th International Symposium on Nuclei in the Cosmos, Jun. 24-29, 2018, LNGS, Assergi, Italy.

(28) H. Yamaguchi (Oral): "Activities at the low-energy RI beam separator CRIB", RIBF Users Meeting 2018, Sep. 5-6, 2018, RIKEN, Wako, Saitama, Japan.

(29) H. Yamaguchi (Invited): "Indirect method application for RI-beam experiments", ECT Workshop "Indirect Methods in Nuclear Astrophysics", Nov. 5-9, 2018, ECT, Trento, Italy.

(30) H. Yamaguchi (Invited): "Studies on nuclear astrophysics and nuclear clustering with low-energy RI beams at CRIB", 13th International Conference on Nucleus-Nucleus Collisions (NN2018), Dec. 4-8, 2018, Omiya, Saitama, Japan.

(31) H. Yamaguchi (seminar): "Study on cluster states in unstable nuclei with alpha-resonant scattering", RIBF Nuclear Physics Seminar, Jan. 8, 2019, RIKEN, Wako, Saitama, Japan.

(32) K. Harada (Oral): "Magneto-optical trapping of radioactive francium atoms: toward search for electron electric dipole moment", 11th Fundamental Physics using Atoms, Mar. 1-4, 2019, OIST, Okinawa, Japan.

(33) H. Nagahama (Invited) : "High-precision measurements for testing CP and CPT symmetry", 3rd ETH Zurich-The University of Tokyo Strategic Partnership Symposium on the UN Sustainable Development Goals and Innovation, Jan. 21-22, 2019, The University of Tokyo, Japan.

(34) T. Abe (Oral): "Recent advances of the no-core Monte Carlo shell model", GANIL Workshop on Nuclear Structure and Reactions for the 2020s, July,2018, GANIL, Caen, France.

(35) T. Abe (Oral): "No-core Monte Carlo shell model calculations with Daejeon16 NN interaction", International Conference "Nuclear Theory in the Supercomputing Era - 2018" (NTSE-2018), Nov. 2018, IBS, Daejeon, Korea.

(36) T. Abe (Oral): "Recent advances in the no-core Monte Carlo shell model for the alpha clustering nature in light nuclei", International workshop on "Recent advances in nuclear structure physics 2018" (RANSP2018), Nov. 2018, YITP, Kyoto, Japan.

(37) T. Abe (Oral): "Alpha-cluster structure from no-core Monte Carlo shell model (oral)", The 50th Reimei workshop on Universal Physics in Many-Body Quantum Systems – From Atoms to Quarks –, Dec. 2018, JAEA, Ibaraki, Japan.

(38) T. Abe (Oral): "Alpha-cluster structure from no-core Monte Carlo shell model", TRIUMF Theory Workshop on "Progress in Ab Initio Techniques in Nuclear Physics", Mar. 2019, TRIUMF, Vancouver, Canada.

(39) N. Shimizu (Oral): ”Large-scale shell model calculations and chiral doublet of 128Cs”, International Conference, Nuclear Theory in the Supercomputing Era 2018 (NTSE-2018), Nov. 2018.

(40) N. Shimizu (Oral): ”Shell-model study in A∼130 nuclei and chiral doublet of ^{128}Cs”, The 9th international workshop ”Quantum Phase Transitions in Nuclei and Many-body Systems”, May. 2018, Padova, Italy.

(41) 角田佑介 (Invited): ”Shapes of Medium-mass Nuclei Studied by Monte Carlo Shell Model Calculations”, Nuclear Structure 2018 (NS2018), Aug. 2018, Michigan State University, Michigan, USA.

(42) N. Tsunoda (Oral): ”Physics in the island of inversion starting from the first principle”, Shapes and Symmetries in Nuclei: from Experiment to Theory (SSNET’18 conference), Oct. 2018, Gif-Sur Yvette, France.

(43) J. Menéndez (Invited): ”Double Gamow-Teller transitions in connection to neutrinoless double-beta decay”, ECT Workshop ”Exploring the role of electro-weak currents, in Atomic Nuclei”, April. 2018, Trento, Italy.

(44) J. Menéndez (Invited): ”Current status of neutrinoless double beta decay matrix elements”, ”13th Conference on the Intersections of Particle and Nuclear Physics (CIPANP 2018)”, May. 2018, Indian Wells, USA.

(45) J. Menéndez (Invited): ”Neutrinoless double-beta decay and direct dark matter detection”, INT Workshop ”From nucleons to nuclei: enabling discovery for neutrinos, dark matter and more”, Jun. 2018, Seattle, USA.

(46) J. Menéndez (Invited): ”Double charge exchanges for double beta decays”, Symposium ”Neutrinos and Dark Matter in Nuclear Physics (NDM18)”, Jul. 2018, Daejeon, South Korea.

(47) J. Menéndez (Invited): ”Recent progress on neutrinoless double-beta decay nuclear matrix elements”, ”Double-Beta Decay and Underground Science” International Workshop, Oct. 2018, Hawaii, USA.

(48) J. Menéndez (Invited): ”Nuclear matrix elements to unveil the nature of neutrinos and dark matter”, Conference ”Shapes and Symmetries in Nuclei: from Experiment to Theory (SSNET’18)”, Nov. 2018, Gif-sur-Yvette, France.

(49) T. Miyagi (Oral): ”Recent progress in the unitary-model-operator approach”, TRIUMF workshop on Progress in Ab Initio Techniques in Nuclear Physics, Feb-Mar. 2018, Vancouver, Canada

(50) 下浦享 (Oral): ”核変換: 新たな核変換の方法を探る” ImPACT プログラム「核変換による高レベル放射性廃棄物の大幅な低減・資源化」公開成果報告会—新たな選択肢の提案、未来に向けて—2019 年 3 月 9 日、品川インターシティホール.

(51) D. Dozono (Invited): ”r-process study with OEDO”, 研究会「重力波観測時代の r プロセスと不安定核」, June 20, 2018, Wako, Japan.

(52) M. Dozono (Oral): ”低速 RI ビームを用いた LLFP 核の核反応データ測定”, 日本原子力学会 2018 年秋の大会, 2018 年 9 月 5 日∼7 日, 岡山大学, 津島キャンパス.

(53) N. Imai (Oral): ”核変換による高レベル放射性廃棄物の大幅な低減･資源化 (4-2) 代理反応を用いた ^{79}Se$(n,\gamma)^{8}$0Se 反応断面積評価”, 日本原子力学会 2019 年春の年会, 2019 年 3 月 20 日∼22 日, 茨城大学, 水戸キャンパス.

(54) M. Dozono (Oral): ”核変換による高レベル放射性廃棄物の大幅な低減・資源化 (4-3) 低速 RI ビームを用いた LLFP 核の陽子・重陽子誘起反応測定”, 日本原子力学会 2019 年春の年会, 2019 年 3 月 20 日∼22 日, 茨城大学, 水戸キャンパス.

(55) Y. Sekiguchi (Oral) : ”p+p や p/d/He^{+}A 衝突 (小さい系) における集団運動”, 35th Heavy Ion Café and 27th Heavy Ion Pub, Jun. 30, 2018, Nagoya, Japan.

(56) T. Gunji (Oral) : ”EM プローブ”, 35th Heavy Ion Café and 27th Heavy Ion Pub, Jun. 30, 2018, Nagoya, Japan.

(57) Y. Sekiguchi for the ALICE Collaboration (Oral) : ”Pseudorapidity dependence of anisotropic flow in p-Pb collisions with the ALICE detector”, The Physical Society of Japan 2019 annual meeting, Mar. 14-17, 2019, Fukuoka, Japan.

(58) T. Gunji for the ALICE Collaboration (Oral): ”Low mass dielectron measurements in pp and Pb-Pb collisions at LHC-ALICE”, The Physical Society of Japan 2019 annual meeting, Mar. 14-17, 2019, Fukuoka, Japan.

(59) 酒見泰寛 (Invited): ”人工 RI 結晶による基本対称性の研究”, 超重元素研究の新展開（研究会）, 2018 年 7 月 30-31 日, 九州大学.

(60) 酒見泰寛 (Invited): ”光格子重元素干渉計による基本対称性の研究”, 物質階層原理＆ヘテロ界面（研究報告会）, 2019 年 2 月 5-6 日, 理化学研究所, 和光キャンパス.

(61) 酒見泰寛 (Invited): ”Fundamental physics with laser cooled heavy elements” 2019 重元素化学ワークショップ, 2019 年 3 月 27-28 日, 理化学研究所, 和光キャンパス.

(62) 長濱弘季 (Invited): ”基本対称性の高精度検証”, RIBF 若手放談会：エキゾチック核物理の将来, Feb. 2019, 理研神戸, 日本.

(63) 角田佑介 (Oral), ”「モンテカルロ殻模型による中重核の構造の研究」”, 素粒子・原子核・宇宙「京からポスト京に向けて」シンポジウム, Jan. 2019, 筑波大学東京キャンパス文京校舎.

(64) 角田直文, ”原子核殻模型の統計力学的理解”, 若手放談会:エキゾチック核物理の将来, Feb. 2019, 理研神戸, 日本.

(65) 角田直文, ”中性子過剰原子核の存在限界とその新しい原理 核力に基づく大規模計算による解析”, 素粒子・原子核・宇宙「京からポスト京に向けて」シンポジウム, Jan. 2019, 筑波大学東京キャンパス文京校舎.

(66) 阿部喬 (Invited): ”大規模数値計算の現在と未来”, RIBF 若手放談会：エキゾチック核物理の将来, Feb. 2019, 理研神戸, 日本.

(67) 清水則孝 (Oral): ”殻模型計算による中重核高スピン状態の記述とカイラル二重項バンド”, 素粒子・原子核・宇宙「京からポスト京に向けて」シンポジウム, Jan. 2019, 東京, 日本.

(68) 大城幸光 (Oral): ”CNS イオン源の現状”, 第 16 回 AVF 合同打ち合わせ, 2018 年 10 月 30-31 日, 高崎量子応用研究所.

(69) 小高康照 (Oral): ”AVF 入射軌道解析の現状”, 第 16 回 AVF 合同打ち合わせ, 2018 年 10 月 30-31 日, 高崎量子応用研究所

(70) M. Dozono (Poster): ”Proton- and deuteron-induced reactions on ^{107}Pd and ^{93}Zr at 20-30 MeV/u”, The 10th international conference on Direct Reaction with Exotic Beams (DREB2018), June 4-8, 2018, Matsue, Japan.

(71) J.W. Hwang (Poster): ”Study on performance of the OEDO beamline”, The 10th international conference on Direct Reaction with Exotic Beams (DREB2018), June 4-8, 2018, Matsue, Japan.

(72) S. Shimoura (Poster): ”Reduction and resource recycling of high-level liquid radioactive wastes through nuclear transmutation-Nuclear Reaction Data of long-lived fission products”, Fifteenth NEA Information Exchange Meeting on Actinide and Fission Product Partitioning and Transmutation, Sept. 30-Oct. 3, 2018, Manchester Hall, Manchester, UK.

(73) K. Kawata (Poster): ”Production of isomer beam around ^{52}Fe nucleus via projectile fragmentation”, Jun. 4-8, 2018, DREB 2018, Matsue, Japan.

(74) S. Hayashi for the ALICE Collaboration (Poster): ”Inclusive J/ψ measurement at mid-rapidity in p-Pb collisions with the ALICE detector”, Quark Matter 2018 (QM2018), May. 13-19, 2018, Venice, Italy.

(75) H. Shimizu (Poster): ”Isomeric RIB Production of Aluminum-26”, 15th International Symposium on Nuclei in the Cosmos, Jun. 24-29, 2018, LNGS, Assergi, Italy.

(76) N. Ozawa (Poster) : ”Development of a New Surface Ionizer for the FrEDM Experiment”, The 11th International Workshop on Fundamental Physics Using Atoms, Mar. 1-4, 2019, OIST, Okinawa, Japan.

(77) 下浦享、他 (Poster): ”PJ2-1 低速 RI ビーム開発”, ImPACT プログラム「核変換による高レベル放射性廃棄物の大幅な低減・資源化」公開成果報告会ー新たな選択肢の提案、未来に向けてー2019 年 3 月 9 日、品川インターシティホール.

(78) Takashi Abe, ”Alpha-cluster structure from no-core Monte Carlo shell model (poster)”, The 1st R-CCS International Symposium on K and Post-K: Simulation, Big Data and AI supporting Society 5.0, Feb. 2019, Kobe, Japan.

(79) 阿部　喬, ”Alpha-cluster structure from no-core Monte Carlo shell model（ポスター発表）”, 新学術領域「量子クラスターで読み解く物質の階層構造」キックオフシンポジウム, 東工大, Nov. 2018, 日本.

B. JPS Meetings

(1) N. Imai (Invited): “Surrogate reaction of ^{79}Se(n,γ)”, The 5th Joint Meeting of the APS Division of Nuclear Physics and the Physical Society of Japan, Oct. 23-27, 2018, Waikoloa, Hawaii, USA.

(2) S. Michimasa (Oral): ”Direct mass measurements of very neutron-rich calcium isotopes beyond N=34”, The 5th Joint Meeting of the APS Division of Nuclear Physics and the Physical Society of Japan, Oct. 23-27, 2018, Waikoloa, Hawaii, USA.

(3) M. Dozono (Oral): ”Nuclear reaction study for long-lived fission products in nuclear waste: Proton-and deuteron-induced reactions on ^{107}Pd and ^{93}Zr at 20-30 MeV/u”, The 5th Joint Meeting of the APS Division of Nuclear Physics and the Physical Society of Japan, Oct. 23-27, 2018, Waikoloa, Hawaii, USA.

(4) S. Ota (Invited): ”Experimental study of the isospin dependence of nuclear incompressibility”, The 5th Joint Meeting of the APS Division of Nuclear Physics and the Physical Society of Japan, Oct. 23-27, 2018, Waikoloa, Hawaii, USA.

(5) S. Masuoka (Oral): “Re-measurement of ^{4}He(^{8}He,^{8}Be) reaction”, The 5th Joint Meeting of the APS Division of Nuclear Physics and the Physical Society of Japan, Oct. 23-27, 2018, Waikoloa, Hawaii, USA.

(6) R. Tsunoda (Oral): ”Proton resonance scattering of a shape-coexistence nucleus ^{118}Sn”, The 5th Joint Meeting of the APS Division of Nuclear Physics and the Physical Society of Japan, Oct. 23-27, 2018, Waikoloa, Hawaii, USA.

(7) K. Kawata (Oral): ”Production of isomers around ^{52}Fe nucleus via projectile fragmentation”, The 5th Joint Meeting of the APS Division of Nuclear Physics and the Physical Society of Japan, Oct. 23-27, 2018, Waikoloa, Hawaii, USA.

(8) H. Tokieda (Oral): ”CNS Active Target (CAT) for high-intensity heavy-ion beam experiment”, The 5th Joint Meeting of the APS Division of Nuclear Physics and the Physical Society of Japan, Oct. 23-27, 2018, Waikoloa, Hawaii, USA.

(9) C. Iwamoto (Oral): ”Performance evaluation of Dual Gain Multi-layer Thick GEM for CAT with high-intensity heavy-ion beams”, The 5th Joint Meeting of the APS Division of Nuclear Physics and the Physical Society of Japan, Oct. 23-27, 2018, Waikoloa, Hawaii, USA.

(10) Y. Sekiguchi for the ALICE Collaboration (Oral): ”Long range angular correlations in p-Pb collisions with ALICE”, Fourth Joint Meeting of the Nuclear Physics Divisions of the American Physical Society and The Physical Society of Japan, Oct. 23-27, 2018, Hawaii, USA.

(11) S. Hayashi for the ALICE Collaboration (Oral): ”J/ψ production in p-Pb collisions with the ALICE detector”, Fourth Joint Meeting of the Nuclear Physics Divisions of the American Physical Society and The Physical Society of Japan, Oct. 23-27, 2018, Hawaii, USA.

(12) H. Nagahama (Oral) : ”A new approach to high-precision measurements of the electron EDM using francium atoms”, Fourth Joint Meeting of the Nuclear Physics Divisions of the American Physical Society and The Physical Society of Japan, Oct. 23-27, 2018, Hawaii, USA.

(13) T. Abe (Oral): ”Large-scale computation of the no-core Monte Carlo shell model for nuclear many-body problems”, 5th joint meeting of the APS Division of Nuclear Physics and the Physical Society of Japan, Oct. 2018, Hawaii, USA.

(14) T. Abe (Oral): ”Recent results and implications of no-core MCSM calculations for nuclear structure”, 5th joint meeting of the APS Division of Nuclear Physics and the Physical Society of Japan, Oct. 2018, Hawaii, USA.

(15) N. Shimizu (Oral): ”Double Gamow Teller transition and its relation to neutrinoless double beta decay matrix element”, American Physical Society, 5th Joint Meeting of the APS Division of Nuclear Physics and the Physical Society of Japan, Oct. 2018, Hawaii, USA.

(16) 角田佑介 (Invited): ”Large-scale shell model calculations for structure of Ni and Cu isotopes”, Fifth Joint Meeting of the Nuclear Physics Divisions of the APS and the JPS (HAWAII 2018), Oct. 2018, Hilton Waikoloa Village, Hawaii, USA.

(17) N. Tsunoda (Oral): ”Study of neutron-rich nuclei via nuclear force and microscopic theory”, Fifth Joint Meeting of the Nuclear Physics Divisions of the APS and JPS, Oct 2018, Waikoloa village, Hawaii, USA.

(18) J. Menéndez (Invited): ”Nuclear observables to constrain neutrinoless double-beta decay”, ”Fifth Joint Meeting of the Nuclear Physics Divisions of the American Physical Society and Japanese Physical Society”, Oct. 2018, Hawaii, USA.

(19) S. Michimasa (Invited): ”Closed-shell property at N = 34 seen in the masses of neutron-rich Ca isotopes”, 日本物理学会第 74 回年次会, 2019 年 3 月 14 日〜17 日, 九州大学, 伊都キャンパス.

(20) M. Dozono (Oral): ”低速 RI ビームを用いた ^{107}Pd の陽子・重陽子誘起反応測定”, 日本物理学会第 7 回年次会, 2019 年 3 月 14 日〜17 日, 九州大学, 伊都キャンパス.

(21) S. Masuoka (Oral): ”二重荷電交換反応 ^{4}He(^{8}He,^{8}Be) 反応の再測定 (II)”, 日本物理学会第 74 回年次会, 2019 年 3 月 14 日〜17 日, 九州大学, 伊都キャンパス.

(22) J.W. Hwang (Oral): ”Angle-tunable Degrader for a low-energy beamline”, 日本物理学会第 74 回年次会, 2019 年 3 月 14 日〜17 日, 九州大学, 伊都キャンパス.

(23) 早水友洋 (Oral): ”電子の永久電気双極子モーメント探索へ向けたフランシウム原子の生成とトラップ”, 2019 年 3 月 14 日〜17 日, 日本物理学会第 74 回年次会, 九州大学, 伊都キャンパス.

(24) N. Tsunoda (Oral): ”Physics in neutron-rich nuclei with the effective interaction for the shell model based on nuclear force”, 日本物理学会第 73 回年次大会, Mar. 2019, 福岡大学, 日本.

(25) 清水則孝 (Oral): ”制限ボルツマンマシンによる殻模型波動関数の記述”, 日本物理学会第 73 回年次大会, Mar. 2019, 福岡, 日本.

C. Lectures

(1) Y. Sakemi, H. Yamaguchi: ”Nuclear Physics III”, Summer, 2018.

(2) T. Gunji (with K. Fukushima, K. Ozawa, H. Liang): ”Hadron Physics”, Summer, 2018.

(3) K. Yako (with M. Yokoyama): ”Experimental Techniques in Particle and Nuclear Physics”, Winter, 2018.

(4) N. Imai: ”Physics Seminar”, Winter, 2018.

(5) N. Imai: ”Classical Mechanics A for undergraduate students”, Summer, 2018.

(6) S. Ota: ”Physics Experiment II”, Winter, 2018.

(7) H. Yamaguchi, T. Gunji, S. Michimasa: ”Experience seminar for Freshmen and Sophomore”, Winter, 2018.

Personnel

Director

SHIMOURA, Susumu	*Professor, Graduate School of Science* *Center for Nuclear Study*

Scientific Staff

SAKEMI, Yasuhiro	*Professor*
YAKO, Kentaro	*Associate Professor*
IMAI, Nobuaki	*Associate Professor*
GUNJI, Taku	*Associate Professor*
SHIMIZU, Noritaka	*Project Associate Professor*
YAMAGUCHI, Hidetoshi	*Lecturer*
WIMMER, Kathrin	*Lecturer*
MICHIMASA, Shin'ichiro	*Assistant Professor*
OTA, Shinsuke	*Assistant Professor*
NAGAHAMA, Hiroki	*Assistant Professor*

Guest Professors

UTSUNO, Yutaka	*JAEA*
MIZOI, Yutaka	*Osaka Electro-Communication University*

Technical Staff

KOTAKA, Yasuteru

Technical Assistants

OHSHIRO, Yukimitsu
KOJIMA, Reiko
YAGYU, Masayoshi

Project Research Associates

TOGASHI, Tomoaki
BELIUSKINA, Olga
DOZONO, Masanori
HAYAKAWA, Seiya
ABE, Takashi, Javier
TSUNODA, Naofumi

Post Doctoral Associates

HAYASHI, ShinIchi
IWAMOTO, Chihiro
SCHROCK, Philipp
YANG, Lei
STUHL, Laszlo
TSUNODA, Yusuke
MENÉNDEZ SANCHEZ, Javier
HWANG, Jongwon
MIYAGI, Takayuki
TAKEUCHI, Satoshi
HAYAMIZU, Tomohiro
ZHANG, Ningtao

Assistant Teaching Staff

TOKIEDA, Hiroshi
TAKAKI, Motonobu
SEKIGUCHI, Yuko

Graduate Students

MASUOKA, Soichiro
KITAMURA, Noritaka
KAWATA, Keita
SHIMIZU, Hideki
TSUNODA, Reiko
OZAWA, Naoya

Administration Staff

OSUGI, Toshio
YAMAMOTO, Ikuko
KISHI, Yukino
ENDO, Takako

Committees

Steering Committee

TAKEDA, Hiroyuki	*Department of Physics, Graduate School of Science, UT*
HOSHINO, Masahiro	*Department of Earth and Planetary Physics, Graduate School of Science, UT*
YAMAMOTO, Satoshi	*Department of Physics, Graduate School of Science, UT*
SAKURAI, Hiroyoshi	*Department of Physics, Graduate School of Science, UT*
MORI, Toshinori	*International Center for Elementary Particle Physics, UT*
TAKAHASHI, Hiroyuki	*Department of Nuclear Engineering and Management, Graduate School of Engineering, UT*
SHIMOURA, Susumu	*Center for Nuclear Study, Graduate School of Science, UT*
SAKEMI, Yasuhiro	*Center for Nuclear Study, Graduate School of Science, UT*
YAKO, Kentaro	*Center for Nuclear Study, Graduate School of Science, UT*
TAMURA, Hirokazu	*Department of Physics, Graduate School of Science, Tohoku University*